4D PRINTING OF POLYMER-BASED SMART STRUCTURES BY THERMAL ACTIVATION

JOANNE TEOH EE MEI

School of Mechanical and Aerospace Engineering

A thesis submitted to the Nanyang Technological University
in fulfilment of the requirement for the degree of
Doctor of Philosophy

2018

Acknowledgement

The author would like to express utmost gratitude to the following individuals for their help thus far. First and foremost, the author would like to thank Professor Chua Chee Kai and Associate Professor Prof Liu Yong for supervising this research. Especially thankful for their patience in guiding through technical writing. I am grateful to Singapore Centre for 3D Printing's staff providing support to this work, especially to Dr An Jia.

The author would also like to express sincere appreciation to Assistant Professor Yeong Wai Yee and Dr Liu Dan for their time in assessing the qualifying exam.

This report would not have been possible without the assistance of the laboratory specialists from School of Mechanical and Aerospace Engineering and School of Materials Science and Engineering, Nanyang Technological University. Lastly, to Nanyang Technological University for the scholarship opportunity.

Abstract

4D printing is an emerging technology and presents a significant advancement over 3D printing. By leveraging on additive manufacturing of shape memory materials, this technology can enable controlled shape recovery of complex structures leading to a broad range of disruptive commercial applications including product design, industrial manufacturing and biomedical implementation.

4D printing has attracted significant attention from both the research community and industry. Commercial computer aided design software tools are available to design and simulate shape recovery. However, there is limited research on systematic design for shape recovery of complex structures fabricated using shape memory materials. This research is aimed to establish a systematic design methodology for 4D printing using polymer based shape memory materials by thermal stimulation. Polymer shape memory material provides key advantages in terms of low temperature deposition and fabrication. In addition, different polymer based composite shape memory materials can be synthesised, formulated and customised to achieve different thermomechanical properties, leading to the practical choice of using thermal stimulus where glass transition temperature can be used as the controllable parameter for shape recovery.

In this research, three design guidelines have been developed. Firstly, (1) quantifying the relationship between smart structure design and mechanical fracture characteristics during shape setting; and (2) allocating multimaterials at different levels of design to obtain complex response behaviours. Secondly, a thorough understanding of heat transfer in 4D smart structures in relation to their self-response behaviours. Lastly, to explore the feasibility of printing and programming crossfolded smart structures as well as to characterize crossfolded structures. The systematic design methodology was established using computer aided design, finite element simulation and empirical analysis. ANSYS software was used to perform

computer aided design and finite element simulation of single-material structures to analyse shape recovery characteristics of complex structures. It was also used to establish critical design guidelines and material parameters that significantly impact the shape recovery performance including response rate and recovery path. Different shape recovery structures including cross-folding were investigated. Stress relief feature were also designed and analysed to establish guidelines for reducing fracture during both programming and shape recovery stages. Experiments using fabricated test samples were used to perform correlation and validation of results obtained from computer aided design and finite element simulation.

We have established design guidelines and material parameters that impact the controlled multistage response of 4D printed structures. These parameters included printed thickness, stress relief features and material properties. By optimising these parameters, we have demonstrated repeatable shape recovery performance of complex single-material and multi-material structures, an example was the self-morphing artificial orchid flower which was thermally activated to blossom.

Table of contents

List of figures

List of tables

List of abbreviations

3DP	Three-Dimensional Printing
4DP	Four-Dimensional Printing
CAD	Computer Aided Design
DLP	Digital Light Processing
DMA	Dynamic Mechanical Analysis
DSC	Differential Scanning Calorimetry
FEA	Finite Element Analysis
SLA	Stereolithography
SLM	Selective Laser Melting
SMA	Shape Memory Alloy
SME	Shape Memory Effect
SMM	Shape Memory Material
SMP	Shape Memory Polymer
STL	Standard Triangle Language
TB	TangoBlack
T_g	Glass Transition Temperature
UV	Ultraviolet
VW	VeroWhite
VM	VeroMagenta

CHAPTER ONE - INTRODUCTION

1.1 Background

Since three-dimensional printing (3DP) or additive manufacturing was developed in the 1980s, it has been widely adopted in a wide range of manufacturing applications [1]. In a generic 3D printing process flow, the desired product structure is designed by 3D modelling with Computer Aided Design (CAD) software such as SolidWorks and then sent to a specific 3D printer for rapid prototyping or small batch production of functional parts. One most recent development in 3D printing for advanced manufacturing is four-dimensional printing (4DP). 4D printing refers to the fabrication of a dynamic 3D structure using shape memory materials and is capable of changing its shape over time [2-4]. The pre-determined design structure, defined as the permanent shape, is first fabricated using a 3D printer and then the structure is programmed to a temporary shape using an external stimulus. The structure will recover to its permanent shape when the same external stimulus is applied. The concept of 4D printing originated from Dr Skylar Tibbits at Massachusetts Institute of Technology (MIT). MIT’s shape memory based structure is activated using water absorption stimulus, such that the movement of the structure is activated by the swelling of the materials [5].

4D printing is currently developed by industry leaders as well as at various research institutions. One prominent development in 4D printing in the industry is the collaboration among MIT’s Self-Assembly Lab, 3D printing manufacturer Stratasys and 3D software company Autodesk. Relying on PolyJet technology, they have jointly developed water activated complex self-evolving structures [6]. In general, 4D printing can be classified as multi-material 4D printing and single material 4D printing. For example, heat activated active composite materials have been 4D printed at Xi’an Jiaotong University and Zhejiang University [7]. Similarly, heat activated multi-material structures such as active origami and controlled sequential self-folding boxes have been reported by Georgia Institute of Technology and Singapore University of

Technology and Design [8, 9]. The advantages of using multiple materials are complex structural design and the control over multistage sequential responses, but the use of multiple materials is subject to either a wet environment or the range of the glass transition temperatures of the materials. Biomimetic 4D printing using hydrogels conducted at Harvard University is an example of single material 4D printing [10]. The advantage of using single material in 4D printing is the simplicity in design and more choices on materials and 3D printing systems (e.g. stereolithography, fused deposition modelling, selective laser melting, etc.). However, single material 4D printing is unable to achieve multistage sequential responses, which limits the complexity of 4D printed products.

The key advantage of 4D printing over 3D printing is the ability for structures to transform or change physical form without the use of additional external mechanical mechanism, which not only saves space and time but also eliminates manpower and human errors, especially in a harsh environment, e.g. compactable structures for deployable space devices application. In addition, different shape memory materials can also be combined to create hierarchical multiple responses on a single structure [11] . Printable material properties can be improved to create more durable materials [12]. Moreover, the structural designs of the 3D printed products can be simplified as well, e.g. a 3D box can be designed and printed as a simple 2D structure which then self-assembles into a 3D box. Therefore, the application of 4D printing holds many promises in the future of science and engineering in areas such as manufacturing [13] , military [4] and biomedical [14] applications.

However, 4D printing is relatively a new concept that is still very much in the research and development stage. Currently, shape memory materials for 4D printing are limited, some have to be printable and curable by ultraviolet (UV) light using the PolyJet technology and others such as metal powder have to be printable with selective laser melting (SLM) process. Nevertheless, 4D printing is gaining momentum in the research field with significant application potential and is considered to be a significant advancement over 3D printing. In order to create 4D printed products, the four essential elements are: Computer-aided programmable design, 3D printer, smart materials and stimulation. For example, a PolyJet-based 4D printing is shown in Figure 1. In 4D printing, smart refers to the ability to remember the as- printed form before transformation. Essentially it is a responsive structure upon an external stimulus, e.g. thermal stimulation in this case.

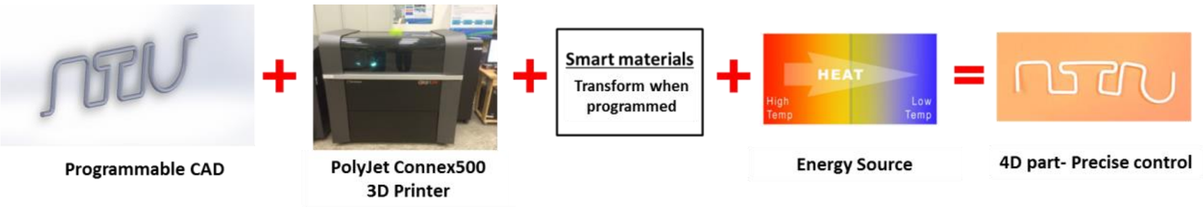

Figure 1. Essential elements in a PolyJet based 4D printing

At first, the structures should be designed to enable physical shape transformation upon application of external stimulus. Although there are commercially available computer-aided software tools such as Autodesk Cyborg and Nervous System Kinematics for 4D printing, a general guideline for a working programmable design is still lacking in the field. Therefore this research intends to develop a set of guidelines for a working programmable design.

The second element is printer. The 3D printer must be able to print shape memory materials. 4D printing has been investigated using different additive manufacturing process technologies such as Fused Deposition Modelling (FDM) [15], stereolithography apparatus (SLA) [16], selective laser melting (SLM) [17] and PolyJet [11]. FDM, SLA and SLM use single shape memory material to create single-stage response and thermal stimulus is used for shape morphing activation. However, PolyJet is different as it enables the use of multiple materials for multistage responses by both hydration and thermal activation. This also enables design and fabrication of complex 4D printing structures. Therefore PolyJet is selected in this research.

Shape memory materials are pre-requisites for 4D printing. The materials must satisfy two fundamental requirements: 3D printability and reconfigurability upon stimulus application. Thus, Shape Memory Materials (SMMs) are potential candidate materials for 4D printing. They have an inherent property, called Shape Memory Effect (SME), which is the ability of a material to recover to its original shape from significant deformation when external stimulus, such as heat, is applied. The two common categories of Shape Memory Materials are Shape Memory Alloys (SMAs) and Shape Memory Polymers (SMPs). Currently on the market there are both 3D printers printing either polymers or alloys. Each has its own advantages; however, polymers are usually preferred due to its low melting temperature, low cost production and compatibility with printing. Currently the 4D printing research works are polymer dominated, mainly because 3D printing of shape memory alloy is challenging and has achieved limited success. Therefore, polymers are selected in this research. The selection of PolyJet printer is mainly because multiple materials are required for sequential activation, which is critical for advancement of 4D printing, and PolyJet is almost the only polymer printer which can print multiple materials within a single layer. Most of the materials used in PolyJet are shape memory polymers, whose glass transition temperatures can be varied through mixing two different base materials such as VeroWhitePlus and TangoBlackPlus. The sequential activation can be predefined by controlling the different glass transition temperature of each material.

The last element is stimulation. 4D printing uses external stimuli types such as electricity, light, magnetism, moisture, pH value and thermal [18-20]. Multiple external stimuli types can also be combined to achieve a more complex shape morphing design. In this research, we have selected thermal stimulus to achieve design and control of shape memory polymer materials since the self-response characteristics are partly determined by the T_g (glass transition temperature) of single or multiple shape memory polymer materials. Shape memory materials with different T_g can be selected to achieve different self-response characteristics. Similarly, multiple materials can be implemented to achieve multistage shape morphing. Self- response refers to the ability to transform into a predetermined shape and function after fabrication upon an appropriate external stimulus. If the stimulus is heat, then it is called heat responsive.

1.2 Motivation

This research focuses on the first element of 4D printing – the programmable design. The key motivation is to realize the vision of designing, predicting and implementing programmable complex structures in multi-material 4D printing. In particular, there is limited research literature on the design methodology of thermally activated smart structures such as programmability of smart structures, method for allocation of multiple materials in hierarchical complex smart structures and the effect of geometric design (e.g. thickness) on the thermal responses of smart structures. Therefore, this research is focused on development and validation of a design methodology implementation of thermally responsive SMPs using 4D printing.

The three main stages of work in this research are: 1) characterization of SMPs; 2) 3D printing of SMPs; 3) design and programming of 3D hierarchical structures of single-stage and multistage in combination with single materials and multi-materials. In developing the design methodology for 4D printing structures, the design requirements of a 4D printed structure may differ depending on the type of SMPs used and different structural designs. Therefore, before fabricating the arbitrary shapes of the structure, simulating the behaviour and predicting the response time will be useful to prevent wastage of materials on multiple fabrication. In addition, the requirement for programmable designs must also consider controlling multistage response through different factors such as T_g temperatures of multi- materials, heat transfer control with different thicknesses and the hierarchy of multi-folding structures. It would be ideal if the behaviour of the fabricated structural design is similar to the simulated design.

1.3 Objectives

Based on the motivation of this project, the objectives of current research are given as follows:

1. To investigate and establish the design methodology of self-response three-dimensional printed structure (or known as 4D printing) through the use of thermally activated shape memory polymers (SMPs)

2. To design, fabricate and model the mechanical and thermal characteristics of basic 3D printed smart structures (e.g. hinge, artificial flower petal and flower)

3. To design and fabricate a physical prototype (e.g. flower) based on the basic shape-transformation structures for programmed, single stage with multi-level 4D printing and multistage with multi-level 4D printing. Multi-level 4d printing refers to the combination of local (petal) and global (layer) stage change. Here the word “level” refers the hierarchical level within one structure. Hence the local level and global level are different in hierarchy but designed in a single structure.4D printing is achieved concurrently or sequentially at both levels. For example, in the demonstration of an opening orchid flower, the sequential opening of three layers of petals is a global level transformation, while the opening of each individual petal is at the local level which occurs concurrently with the global transformation.

1.4 Scope of research work

This research is aimed at establishing design methodology for 4D printing of thermally activated smart structures. It includes theoretical and experimental research on the optimal process parameters of currently available materials through design, modelling, fabrication and evaluation of multi-component structures. The scope is listed as follows:

- Design, programming and 3D printing of basic primitive forms using various shape memory polymeric materials
- Characterisation of thermal and mechanical properties (e.g. Tg and ultimate tensile strength) of various shape memory polymeric materials
- Modelling the folding/unfolding behaviours of basic primitive forms using Finite Element Analysis method
- Investigation of the thermal requirements for activating the folding/unfolding behaviours of basic primitive forms
- Design, programming and fabrication of a 4D printed single material structure with thickness consideration (e.g. flower) by integrating the basic primitive forms
- Evaluation of the physical behaviour of the 4D printed L-hinge and spiral square structure as compared to simulated results
- Design, programming and fabrication of a 4D printed multi-material system-level structure (e.g. flower) by integrating the basic primitive forms
- Evaluation of the physical behaviour of the 4D printed system-level structure as compared to simulated results

1.5 Organization of report

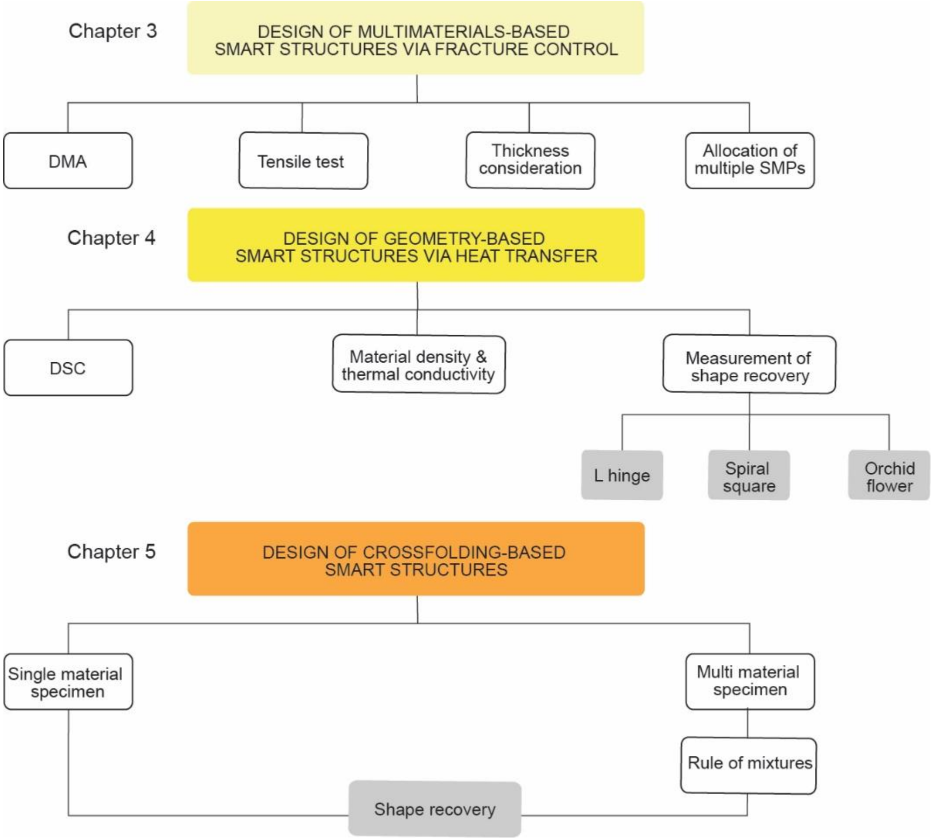

Figure 2. Flow of experiments conducted designed for different types of test

Chapter 1 provides an introduction to the project, highlighting the motivations, objectives and scope of the research.

Chapter 2 reviews the current research development in 4D printing, especially on the properties of SMPs as either single or multiple materials.

Chapter 3 details on the capability and feasibility of 4D printing to print multi-materials, multistage flower. It also covers the methodology for the PolyJet technology with thermal activation, as well as the procedures of the mechanical tests. The incorporation of basic design to system design with the material Tg relationships will be also described. (Figure 2)

Chapter 4 describes on the novel multistage single material structures predicting the structure behaviour in simulation before printing for experiment. (Figure 2)

Chapter 5 provides smart multistage complex cross-folding by characterising shape recovery properties and design guidelines to reduce stress on the surface and minimum thickness for cross-folding structures. (Figure 2)

Chapter 6 states the summary of the current progress of the project, future work to be conducted and final system design to be developed.

CHAPTER TWO - LITERATURE REVIEW

The literature review describes an overview of 3D printing technologies, processes and systems as well as dual-shape and triple-shape memory polymer materials. Specific application examples on 4D printing of shape memory polymer materials and shape morphing characteristics using different external stimulus are also analysed. It is found that in heat activated 4D printing, both shape setting and controlled response behaviours are dependent on smart structure design. However, virtually there are no design guidelines in previous research works to ensure the success of setting complex smart structures and controlling complex response behaviours.

2.1 3D printing

2.1.1 Classification of 3D printing

3D printing, also known as additive manufacturing (AM) or rapid prototyping, refers to the fabrication of objects through the process of joining multiple deposited layers to form 3D structures [21]. Gaining popularity since the late 1980s, the number of additive manufacturing processes have grown and they can be classified into liquid based, solid based and powder based types (Figure 3) [22]. Several examples of the techniques are stereolithograpy, sheet lamination, laser sintering, droplet deposition, etc. The main differences of the processes can be described in terms of four key process parameters which are state of raw material, energy source, layer deposition or forming method and state of completed part [23]. Advantages of 3D printing include the capability to create objects with complex internal features that cannot be manufactured with other means, produce parts of different geometry within the same batch and produce customised parts and prototypes at a faster speed and lower cost [24-26].

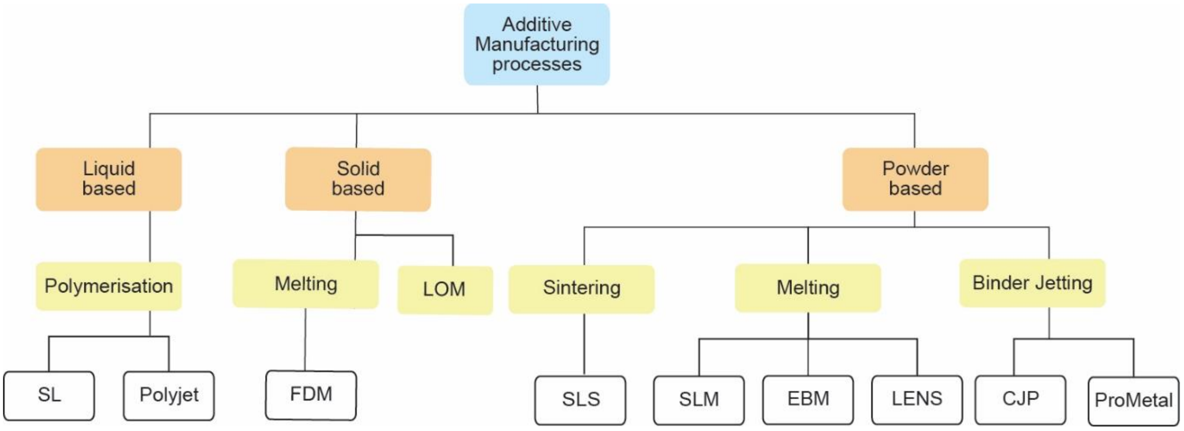

Figure 3. Classification of 3-D printing processes

2.1.2 3D printing process chain

All 3D printing processes have a common process chain which involves mainly three steps (see Figure 4) [27-29]. Firstly, a computer aided design (CAD) software e.g. Solidworks, Rhino, AutoCAD is used to draw a 3D CAD model with actual dimensions. The CAD file is then converted into the .STL (Standard Triangle Language) format, repaired and verified to be error-free before transferring into the computer of the 3D printing machines to be sliced into cross-sections [30, 31]. Secondly, the user has to prepare the building parameters such as building orientation, creating support structures, physical and technological parameters before printing. Thirdly, the printed part is removed from the system and user will have to remove support material if any from the completed part. Secondary processing such as polishing and sanding can also be used to improve surface finish of the part [32].

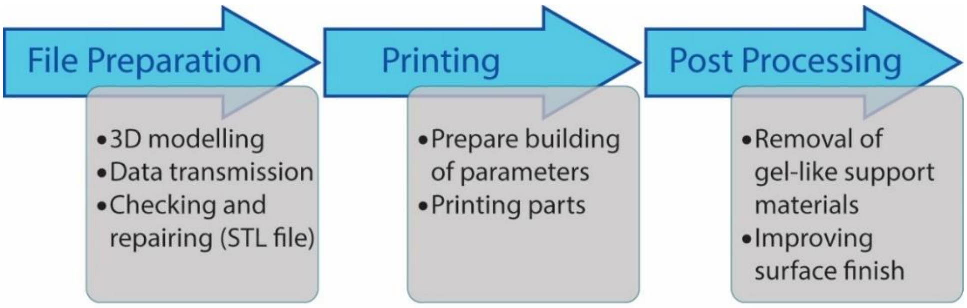

Figure 4. 3D printing process chain

2.1.3 Examples of 3D printing systems

Stereolithography and fused deposition modelling are the earliest 3D printing systems, hence commonly used in the industry now [33] [34]. Stereolithography is a manufacturing technology used to create prototypes in a layer by layer technique using photopolymerisation (Figure 5a). In this technique, full layers of resin are applied at once and then cured using a UV light pattern generator. The UV light triggers photopolymerisation process which causes the monomers to join together forming polymers [35]. SLA is a technology which produced parts by curing a photo-reactive resin with an ultraviolet laser layer-by-layer. Exposure to the ultraviolet laser light cures and solidifies the resin which provides an interface to the layer below. There is an elevator platform which will descend as the layers are being printed. Support structure are required to prevent deflection and to hold the cross sectional area in place. The supports are removed from the finish products manually. One main advantage of stereolithography is resolution. However, it is an expensive process due to the cost of photo-curable resin and the basic cost of the stereolithography machine.

Fused deposition modelling (Figure 5b) is another technique where the model is created by extruding small flattened strings of molten materials to form layers [36]. In this technique, a plastic filament is fed through that extrusion head where the material is melted and deposited by drawing plastic lines on top of previous layers. These molten strings harden instantaneously after being extruded from the nozzle. FDM system is the most commonly used 3D printer, often found at homes and offices as it is relatively cheap in terms of 3D printing machine and materials. In FDM, a nozzle deposits molten plastic in successive layers. The molten plastic solidifies upon touching the printed surface.

PolyJet is developed later than SLA and FDM. Similar to SLA, PolyJet printing (Figure 5c) uses liquid photopolymer materials which are jetted out in droplets onto a build tray and immediately cured by ultraviolet (UV) light. This process repeats for each layer until a solid part is completed [37, 38]. The support material is water soluble and can be washed away with a water jet. Care needs to be taken for delicate features to prevent damage of parts [27]. Table 1 shows the specifications of PolyJet Connex 500. Multi-material printing is possible and the layer thickness can be as low as 16 µm. A major advantage of the using the PolyJet machine is the ability to print multiple materials (maximum 3 for Model Connex3 and 6 for Model J750) in one single model, which can be useful for the design of complex structures with multiple materials [5, 39].

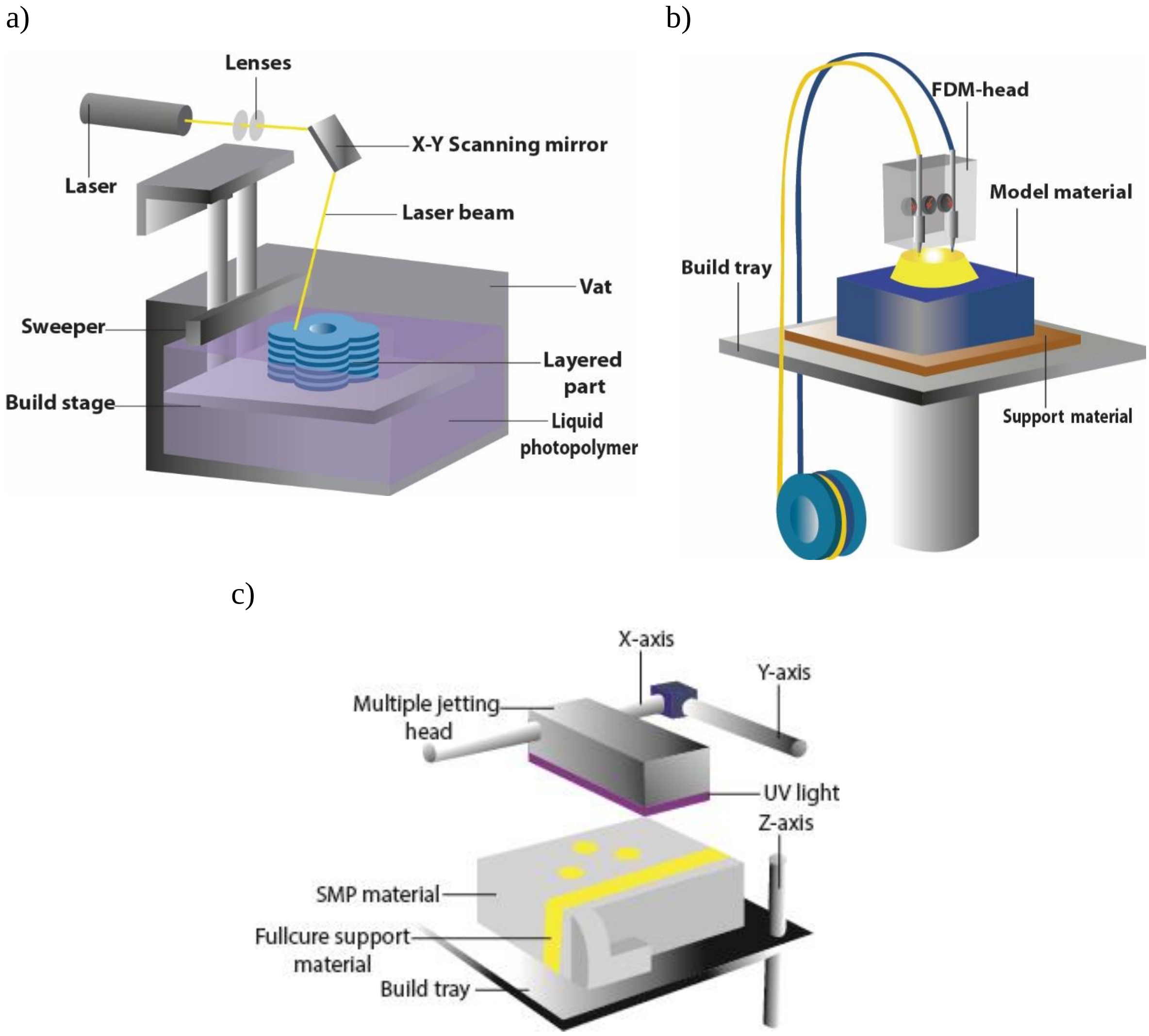

Figure 5. Schematic diagram of a) SLA, b) FDM and c) PolyJet printing

Table 1. PolyJet materials and equipment specifications

Object 500 Connex3	
Machine	Objet 500 Connex3
Build volume	$490 \times 390 \times 200$ mm^3
Method	Material jetting and ultraviolet curing
Material type	Liquid
Material	TangoBlackPlus and Verowhiteplus
Tensile Modulus (MPa)	0.21-18
Layer thickness (mm)	0.016 (minimum)

The choice of printing methods that works best with each application depends primarily on the end goal as there are limitations in different methods of printing [40]. Generally, manufacturing time, building cost, dimensional accuracy and surface finish [23] are weighed in choice of 3D printing process in a prototype development. Currently, there are constant improvements made in the process of each production for better quality of finished parts, and research on the effects of smart material as a choice of input in the production of additive manufacturing [41].

2.2 Shape memory polymers

There are many different types of SMP such as polyurethane from the polyester polyol series [42], Polybornene, trans-Polyisoprene and Styrene-butadiene copolymer [43]. SMPs can transform their shapes from a deformed state or temporary shape to their original state or permanent shapes under appropriate stimulus which can be classified by two types physical type such as temperature, light, electric field, magnetic field and chemical type such as pH, specific ions or enzyme [44]. Thermal sensitive SMP is a typical one, which has been widely studied and used in industry. Thermal sensitive SMPs have a physical cross-linking structure, crystalline/amorphous hard phase, or chemical cross-linking structure and a low temperature transition of crystalline, amorphous or liquid–crystal phase as a switch. They are processed or thermally set to have an original shape. Generally, in the permanent shape, internal stress is zero or very low.

When the SMP is subject to deformation during its programming stage, large internal stress can be stored in the cross-linking structure by cooling the polymer below its T_g. By heating the polymer above its T_g, the SMP recovers its permanent shape thus releasing internal stress stored in the crosslinking structure.

Some of the research on SMP includes the modelling of polyurethane thermomechanical properties [45], photo-thermal engineering of SMP as micro-actuators for the treatment of stroke [46], and usage of SMP as deployable hinges in solar panels [47]. Usage-wise, SMPs have vast applications in smart apparels and textiles [48, 49], intelligent medical devices [50-52], heat shrinkable packages for electronics [53], self-deployable structures in spacecraft and foam [54-57] or bulk [58]

2.2.1 Dual-shape memory polymer

In dual-shape memory polymer materials, the shape morphing capability is determined by a switching phase and a cross-linking phase within a polymer network [59]. The switching phase is used to programme a metastable shape. The shape deformation is maintained by reversible crystallization, vitrification or supramolecular interactions until external stimulus is applied for recovery to the original pre-determined shape. Figure 6 shows the shape morphing flow for a typical structure using dual-shape memory polymer material.

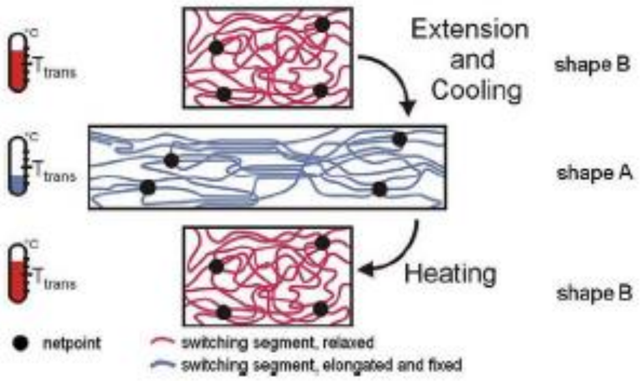

Figure 6. Molecular mechanism of the thermally induced shape-memory effect (See [59] for details)

Thermally induced shape memory polymer materials leverage on linear block copolymers to achieve the switching phase. A typical example is polyurethane which uses glass transition temperature as the switching phase activation. Covalent cross-linking is used to achieve dual-shape capability. Figure 7 shows the shape morphing flow for a typical thermally induced shape memory polymer.

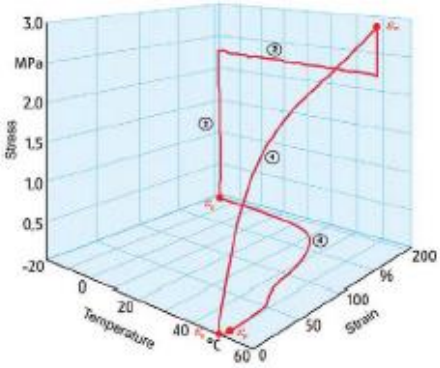

Figure 7. Typical stress-strain-temperature diagram (first cycle) for a thermoplastic shape-memory polymer with a thermally induced shape memory effect. Step 1 of the experiment is strain controlled, while steps 2 through 4, to the beginning of the next cycle are stress-controlled (See [59] for details)

Light induced shape memory polymer materials leverage on photo-reactive molecular switching to achieve switching phase. A typical example is light sensitive polymer which uses UV radiation as the switching phase activation. Figure 8 shows the shape morphing flow (a – f) for a typical light induced shape memory polymer.

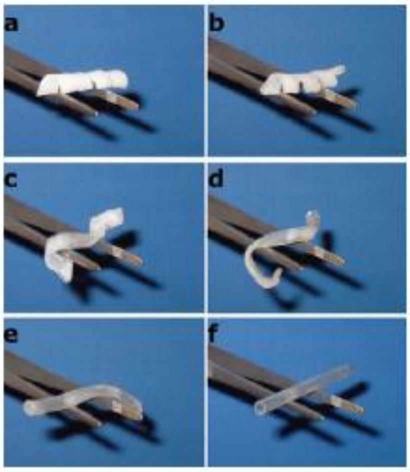

Figure 8. Time series photographs that show the recovery of a shape-memory tube (see [59] for details)

2.2.2 Triple-shape memory polymer

An intrinsic limitation of dual-shape memory material is that the original pre-determined shape must be fixed at the time of fabrication or cross-linking. This restricts shape morphing capability for complex geometries.

Triple-shape memory polymer materials overcome the intrinsic limitation of dual-shape memory polymer materials by providing two metastable shapes in addition to a globally stable shape. These materials comprise of two independent switching phases related to two different transitions [60]. Figure 9 shows the shape morphing flow for a typical structure using triple-shape memory polymer material.

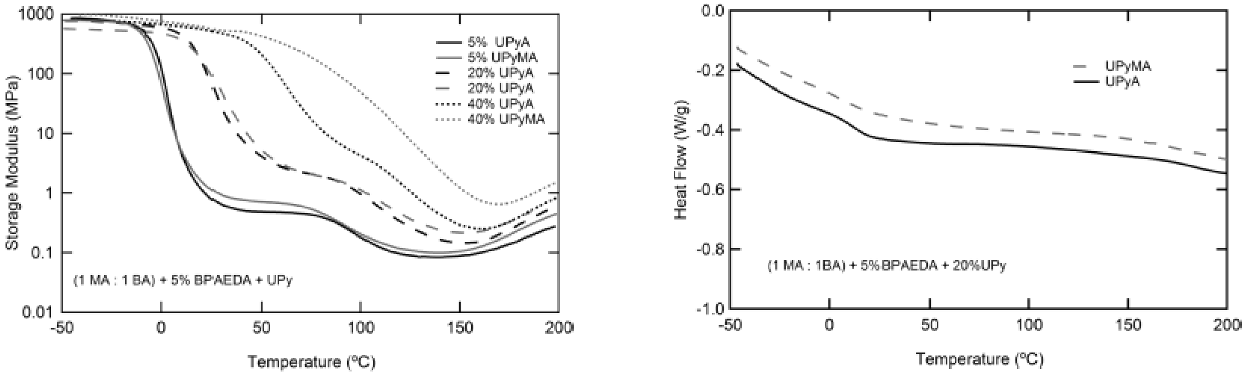

Figure 9. Typical structure using triple-shape memory polymer material (see [60] for details)

Shape memory polymers (SMPs) are stimuli-responsive materials that have the designed properties to enable return from a deformed temporary shape to an original permanent shape via application of external stimulus such as temperature, magnetic fields, light and moisture [61, 62]. SMPs have some advantages and drawbacks as compared to the SMAs and ceramics [61]. These advantages include high strain recovery, lower density, lower cost, simple procedure for programming of shapes and good controllability over the recovery temperature. Moreover, SMPs can be modified chemically to achieve biocompatibility and biodegradability. As a result, they have gained many research interests in various applications. However, their major drawbacks are their low strength, low modulus and low operating temperatures.

In AM, the permanent shape of SMP components can be set by 3D printing while its temporary shape can be set by deformation at above the T_g temperature followed by cooling. The temporary shape of SMPs is generally maintained until being activated by external stimulus. One example of a 3D printed SMP structure using the PolyJet printer is presented in Figure 10. This SMP structure consists of three connected letters "NTU" in the as printed form. It was then heated to above its T_g temperature and straightened at high temperature and cooled to room temperature while maintaining the pulling force. Once the sample has reached room temperature, the pulling force was removed and it took the shape in Figure 10(a). When being heated to above the T_g temperature, the sample returned to the as printed form shown in Figure 10(b), demonstrating a full shape recovery.

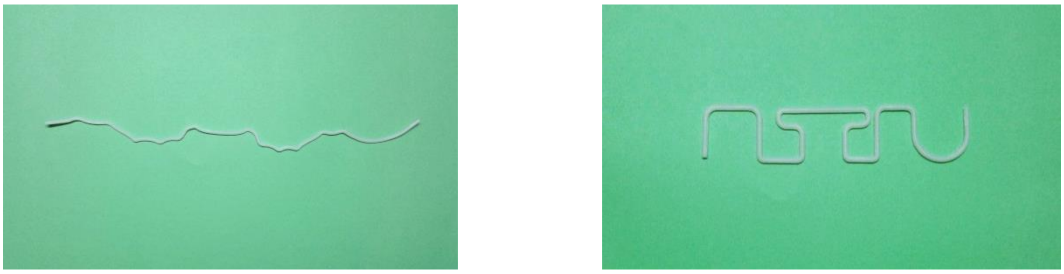
(a) *(b)*

Figure 10. Printed sample of "NTU" before heating (a) and after heating (b)

Video: Single material "NTU"

2.3 4D printing of polymer

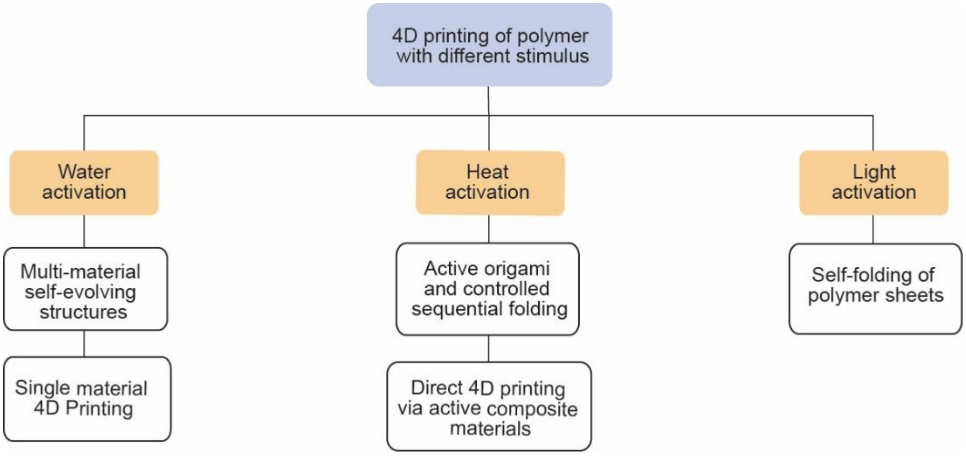

Figure 11. 4D printing of polymer with different stimulus

One important factor to consider when designing a component with multiple materials is the availability of the 3D printing technology. At the current status, PolyJet technology is the most established technology in performing multi-material printing. Thus, most of the developments in 4D printing utilise PolyJet printers in their research to fabricate multi-material components that consist of smart materials and conventional materials. There are different stimulus used for 4D printing of polymer shown in Figure 11.

Moreover, in the developments of 4D printing of multiple materials, the design of the components plays a critical role as the conventional materials do not react to the external stimulus. Hence, the degree of the change in the printed components upon activation is usually determined by the design of the components. In order to illustrate this point, some examples of the developments in 4D printing of multiple materials are discussed. These examples include printed actuators for soft robotics [63], self-evolving structures [64], anti-counterfeiting system [65], *active origami* and controlled sequential folding [61, 66, 67] together with some of the results from our ongoing research.

According to Pei [2], 4D printing is “the process of building a physical object using appropriate additive manufacturing technology, laying down successive layers of stimuli-responsive composite or multi-material with varying properties. After being built, the object reacts to stimuli from the natural environment or through human intervention, resulting in a physical or chemical change of state through time.” Tibbits *et al.* [5] stated 4D printing as a new process that “entails multi-material prints with the capability to transform over time, or a customised material system that can change from one shape to another, directly off the print bed with the fourth dimension described here as the transformation over time, emphasising that printed structures are no longer static, dead objects; rather, they are programmably active and can transform independently.” Thus, according to these definitions, there are three important characteristics of 4D printing that differentiate itself from 3D printing [3]. The first characteristic is that the components printed have incorporated smart materials, be it a smart composite material or a single smart material with self-changing features. The second characteristic is the stimulus that acts on and activates the printed components such as temperature, electricity, ultraviolet (UV) light, moisture and etc. [20, 68]. These stimuli can either come from the natural environment or through human intervention. The third characteristic is the time required for the components to change properties, resulting in a change of state of the components. However, one of the main differences between these two definitions is that Pei considered 4D printing to incorporate either a physical change or chemical change of state while Tibbits *et al.* only considered shape changes. The stand on this is that 4D printing including external activation stimulus will enable the proliferation of additive manufacturing to create complex shape morphing structures.

2.3.1 Water activation

2.3.1.1 Multi-material self-evolving structures

In one of the developments in 4D printing, Raviv *et al.* printed various multi-material components that would transform into their designed shapes when exposed to water [64]. The authors called this concept self-evolving structure. The self-evolving components were basically made up of an extremely hydrophilic polymer material and a rigid plastic material. When this hydrophilic material is exposed to water, it will absorb the water and results in an increase in its volume up to two times.

During the initial stage of this research, three different components that displayed different types of deformations when exposed to water were fabricated. The three types of deformations are illustrated in Figure 12, where the top and middle components exhibit the stretching deformations while the bottom component exhibits the folding deformation.

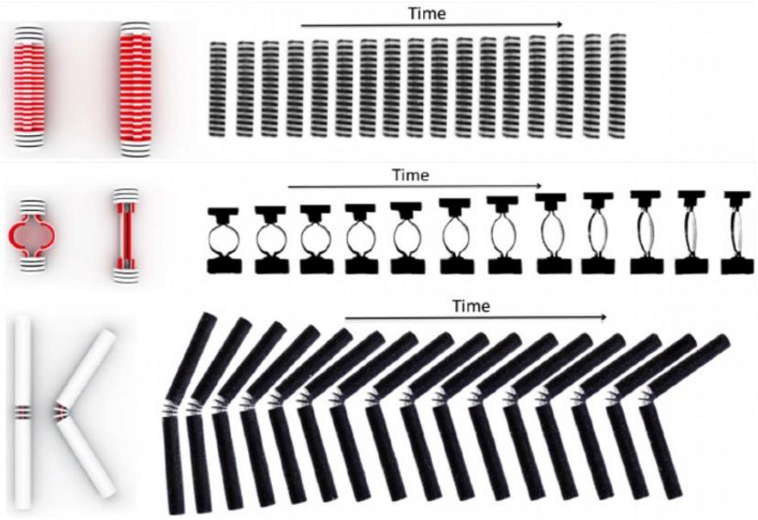

Figure 12. Self-evolving components that exhibited (top) linear stretching, (middle) ring stretching and (bottom) folding over time from left to right (see [64] for details)

The top component in Figure 12 exhibits linear stretching. When this component was exposed to water, its length changes with respect to time and by varying the ratio of hydrophilic material to the rigid material, different percentage of linear expansion can be achieved.

As for the middle component shown in Figure 12, it demonstrates ring stretching. The component was formed by many ring-like shapes and each ring was printed with two different layers of materials. When this component was exposed to water, the inner layer expands and causes deformation of the ring. The overall linear expansion of this component can be controlled by varying the radius or diameter of the rings.

The bottom component in Figure 12 exhibits folding phenomenon. This is done by printing a layer of hydrophilic material over a layer of rigid material. To achieve the desired angle of folding, rigid plates of different spacing and diameters were inserted between the bars so as to stop the folding process when the plates interfered physically with each other.

A variety of more complex multi-material components were fabricated based on the results obtained from the stretching and folding deformations. These complex components have demonstrated 1D folding, 2D folding and 2D folding with stretching. The multi-material component that displayed 2D folding with stretching is shown in Figure 13. This component deforms into convex and concave surfaces via the folding deformation and ring stretching deformation.

Figure 13: Complex 2D multi-material component exhibiting stretching and folding from left to right, and top to bottom (see [64] for details)

Nevertheless, according to the results obtained, mechanical degradation was encountered when the components undergo the transformation cycle of folding and unfolding (wetting/ drying) repeatedly [64]. Moreover, degradation of the hydrophilic material can be observed as well when the material was repeatedly wetted and dried. Furthermore, the transformation between the different shapes is not permanent. Thus, depending on the applications, this reversible transformation can either be an advantage or disadvantage. Another problem encountered is that the top component in Figure 13 is fragile and the expansion is limited to only 30% [64]. Nonetheless, this problem might be solvable by exploring new materials in the future research [64].

Overall, there are a lot of possible future improvements to be done [64]. In [64], only hydrophilic materials that react to water have been explored. Other activating mechanisms such as temperature change and exposure to UV light can also be explored. In addition, the physical properties of the hydrophilic material and their behaviour can be predicted by simulating on a molecular level instead of using the spring-mass model in this research.

Lastly, this novel design of self-evolving structure could be applicable in many fields. For instance, a structure could be readily assembled under the deep water which would be difficult for humans to do otherwise.

2.3.1.2 Single material 4D Printing

Gladman *et al.* discloses biomimetic shape morphing of complex structures using aqueous stimulus [69]. The hydrogel matrix comprises of stiff cellulose fibrils embedded in a soft acrylamide matrix. Anisotropic swelling of directly printed hydrogel matrix structures with pre-defined geometric orientation is used to activate three-dimensional shape morphing in figure 14. Controlled shape morphing was successfully demonstrated in complex flower shapes [69]. Although aqueous stimulus was demonstrated, the authors did not disclose successful demonstration of reverse stimulus, i.e. removal of water content in the hydrogel matrix. Our research is focused on thermal stimulus activation which intrinsically allows application of reverse stimulus which is critical in practical applications.

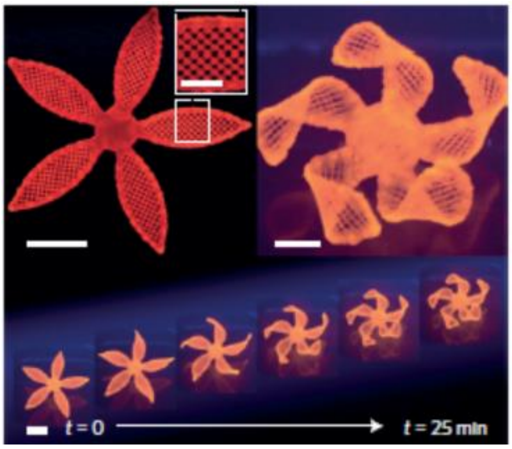

Figure 14. Simple flowers composed of bilayers with respect to the long axis of each petal, with time-lapse sequences of the flowers during the swelling process (see [69] for details)

2.3.2 Heat activation

2.3.2.1 Active origami and controlled sequential folding

Although origami is a type of traditional art where a piece of flat paper is being folded into a 3D object, the notion of origami has been widely explored nowadays to provide innovative solutions to the problems of compacting large objects into a small volume of space. For instance, the applications of origami can be found on the airbags for automobiles, cartons, shopping bags and photovoltaic solar cells with shape changing ability. However, the packing process is often challenging and may lead to an increase in the infrastructure cost since new equipment may be required should there be any changes in the folding design. Therefore, the idea of *active origami* is intriguing as it can help to reduce the investment needed for the folding equipment.

Active origami is defined as a design to create an origami object that has the ability to self-fold or self-unfold [67]. In order to do that, smart materials are required. For example, there are researches being performed on the design of origami by using SMPs, light activated polymers, and SMAs recently.

Therefore, one of the developments in 4D printing of *active origami* is to make use of multi-material printing technology to print and investigate the performance of printed active composites (PACs) [66]. Examples of PACs are soft composites made up of glassy SMP fibres that reinforce the elastomeric matrix. By adjusting the volume fraction and orientation of the SMP fibres and the stacking order of the laminas, different laminates can be fabricated. These laminates will then undergo thermomechanical programming so as to adopt complex 3D configurations such as bending, coiling, twisting and folding as shown in Figure 15. The original flat plate shape of the laminates can be recovered by heating the deformed laminates. In addition, a self-folding box was designed and printed with PACs as the hinges that connect to the inactive plates made from the stiff plastics [66].

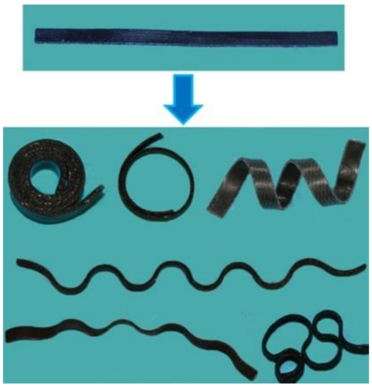

Figure 15: Laminates adopting complex 3D configurations including bending, coiling, twisting and folding (see [66] for details)

Following the first part of the research, the second part of the research was conducted by applying the concept of 4D printing to the design and fabrication of *active origami* [67]. The research focuses mainly on the understanding of the thermomechanics of the structures of the PACs hinges [67]. Experiments were performed to determine the relationship between the hinge folding angle and the microstructural parameters. Moreover, theory that describes the observed phenomena was developed as well. The design and fabrication of the *active origami* consists of printing flat polymer sheets that consist of the PACs hinges [67]. These PACs hinges were fabricated in the same manner as the first part of the research conducted. However, the PACs hinges fabricated here have only two layers of PACs laminates. One layer contains only elastomeric matrix material while the other layer contains a pre-determined fibre size and spacing.

Using a theoretical model developed to provide direction in choosing the design parameters, several *active origami* components were designed and fabricated to demonstrate the prescribed folding angles. These components self-folded from flat polymer sheets and they include a box consisting of six sides and a five-sided pyramid as presented in Figure 16, and two origami airplanes. Additionally, directly printing a 3D object was proved to be feasible as well. However, doing so would require more materials due to the need for support structures and longer fabrication time as the removal of these supports would increase the post-processing time.

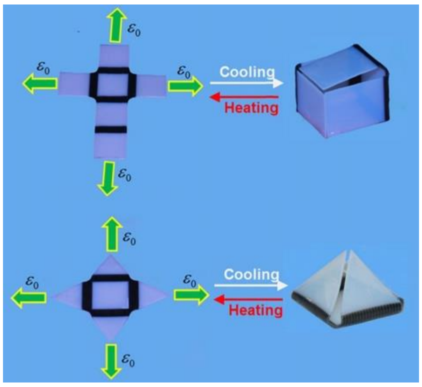

Figure 16: Before self-folding and after self-folding of active origami box and pyramid (see [67] for details)

In summary, the concept of PACs was demonstrated and they were shown to be able to integrate with other printed parts to form a 3D component that can transform over time. Moreover, the concept of 4D printing was applied and *active origami* was created. As for the potential and challenges of this research, the most extreme case will be to fabricate a component with continuous and spatially varying material properties [66]. Furthermore, this idea of 4D printing can be further developed by making use of other smart materials and computational design tools such as shape and topology optimisation to come out with the layout of the materials within the composites [66]. In this case, it will be possible to achieve larger changes in the configuration of the components.

Another research area to concentrate on will be to understand and achieve controlled sequential folding or shape recovery of the *active origami*. As the design of the origami gets more complex, folding of the *active origami* parts at the same instant might just cause the different folding parts to interfere with each other before the folding process is complete. Moreover, very few researches have been done on the study of controlled sequential shape recovery of SMPs or *active origami*.

Recently, Yu *et al.* have performed research on the fabrication of SMPs with spontaneous and controlled sequential shape recovery properties [61]. In their research, the material used is an epoxy based UV curable SMP with SME that is activated by temperature. Since the SMP is sensitive to thermal changes, controlled sequential shape recovery can be achieved by implementing a customised distribution of the SMP thermomechanical properties to the specified sections. This would allow the different sections to activate their shape recovery at different T_g temperatures and thus achieve sequential folding of the printed components.

In [61], experiments on helical components and interlocking components were demonstrated. These components have rectangular plates and their hinges were made up of SMPs with either different T_g temperatures or same T_g temperatures. The spontaneous and sequential folding process of a helical component with designed order of T_g temperatures is reproduced in Figure 17. The complete shape recovery of the component can be observed at different time through a series of photographs. Additionally, another helical component with the same T_g temperatures at the different hinges was also fabricated. However, this printed component with the same material properties exhibits a slower shape recovery speed and an incomplete shape recovery. Clearly, different materials having different T_g temperatures are required at different hinge sections in order to have a controlled sequential shape recovery or folding process of the printed component.

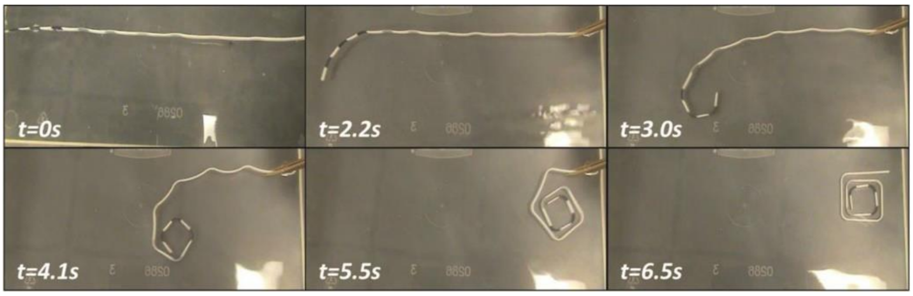

Figure 17. Spontaneous and sequential folding process of helical component with different material properties at various hinge sections (see [61] for details)

This result was again illustrated by the interlocking components. Controlled sequential shape recovery was demonstrated by an interlocking component with a designed order of T_g temperatures. However, when another interlocking component with a reversed order of T_g temperatures and one with the same T_g temperatures at the different hinge sections were tested, none of the two components successfully exhibit complete shape recovery. This observation further confirmed the above conclusion that the order and distribution of material properties at different hinge sections is important in achieving controlled and sequential shape recovery or folding process.

Overall, Yu *et al.* have demonstrated controllability over the shape recovery sequence through the fabrication of helical components and interlocking components [61]. The control over the sequence of the shape recovery is achieved by selecting and assigning different material properties with different T_g temperatures to the various sections. In terms of the potential of this research, the results obtained can have great contributions to the different applications such as permutations of complex deformation and the development of SMP solids that have the ability to self-adjust and self-reinforce to suit the changing environmental conditions [61]. Furthermore, through the use of 3D printing, SMP structures with controlled sequential folding process could enjoy a larger design freedom and a higher resolution in the distribution of material properties [61].

Since 2014, we have been investigating the 4D printing with SMP materials and the design methodologies. Our research activities include both single materials and multiple materials for 4D printing and applications. Different from the researches carried out by Qi *et al.* [66, 67] who have adopted SMP fibres within an elastomeric matrix as the material for the hinges to achieve the *active origami* structures, in our research, we have adopted SMP as the sole material for the hinges of the *active origami* structures. The advantage of this approach is that SMPs comprising of multi-material with different percentage of each component enable better freedom in design and shape response. Instead of only using fibres to control the direction of response, our developed structures can response to any direction when the structure is being programmed. Thus, this allows for a better freedom in shape changing geometry, which results in a relationship between the material and dimensional difference reacting to thermal stimulus. Moreover, we have developed reconfigurable origami structures by exploiting the combination of multi-material fabrication and geometric design Figure 18 and Figure 19 illustrate the multistage folding structure and conceptual reconfigurable glider respectively.

In the case of the sample shown in Figure 18, we have achieved controlled sequential folding process of a printed part with different materials printed at different hinge structures. Only the hinges were composed of SMP and the T_g temperatures for the various hinges were different. Hence, the hinges fold at different temperatures during continuous heating and have different stages of recovery, resulting in multistage folding as illustrated in Figure 18.

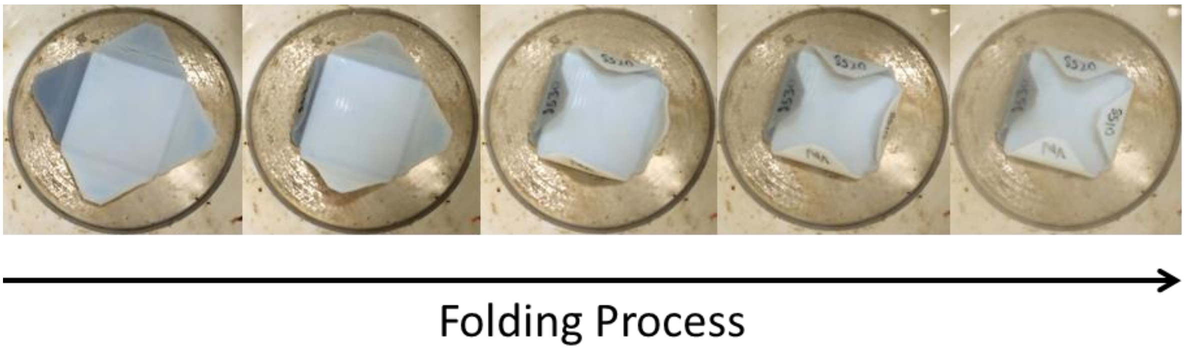

Figure 18.Multistage folding of 4D printed part with different SMP materials at different hinges

In another example, the application of multi-folding in a 3D object represented by a reconfigurable glider is presented in Figure 19. The multi-material part is printed with the hinges consisting of SMPs. The SMPs are located specifically at the hinges such that the planar structure will not collide with the other areas during activation by thermal stimulus. As shown in Figure 19, the glider unfolds from Figure 19a to Figure 19b when it is heated.

Figure 19. Multi-folding glider (a) before heating and (b) after heating

2.3.2.2 Direct 4D printing via active composite materials

An alternative approach used by Ding *et al.*, using direct 4D printing approach with SMPs, integrating the programming steps into the 3D printing process [7]. The sample in this method is ready for shape changing just after printing without any composition change required by gel-based 4D printing or the thermomechanical training required by SMP-based 4D printing. As a result, the 3D-printed component can directly change its shape rapidly upon heating.

In this research, effectively control the photopolymerization process during printing to enable 3Dcomponents with complex geometric form at high spatial resolution in a way that, when removed from the build tray, they exhibit high-fidelity features but with controlled built-in strains.

The deployment step then simply involves heating the component upon which the shape transformation occurs at a time scale controlled by the heat transfer. The target shape morphing, to be activated by thermal stimulus, is pre-determined by the combination of composite material property selection and elastomeric compressive strain which is controlled by printing interval duration shown in figure 20.

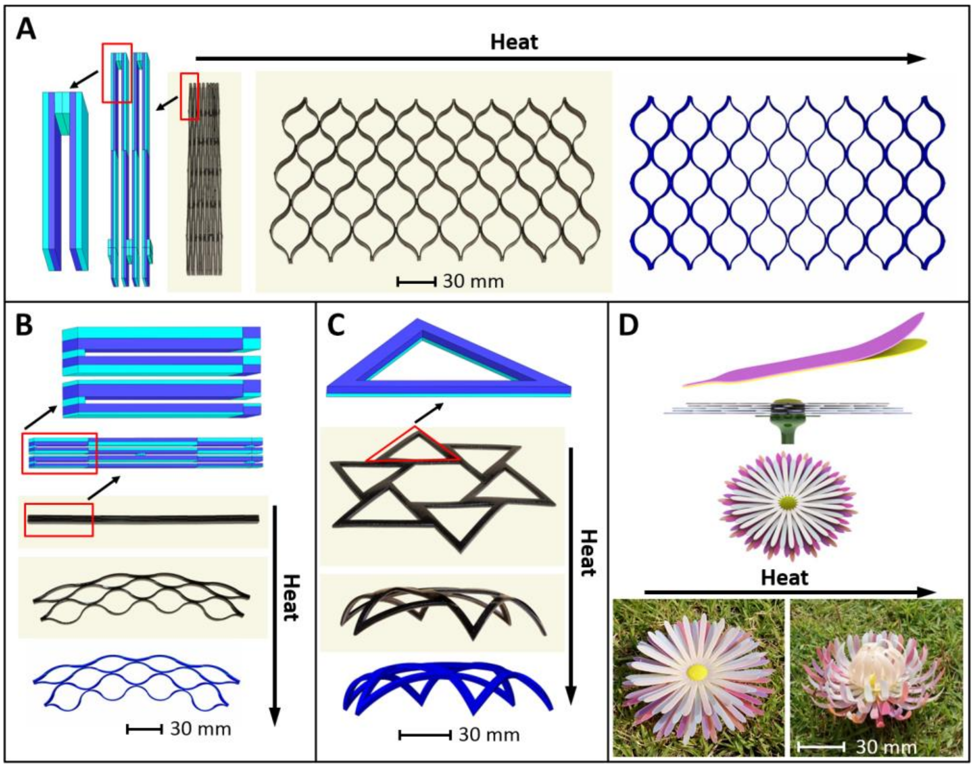

Figure 20. Direct 4D printing of structures consisting of multiple elements

2.3.3 Light activation

Recently, some effort has been made to use light to activate the printed structure. In one research, a polystyrene film in the cut-out shape of a box with inkjet printed black hinges that absorb heat faster than the remaining material and capable of folding into a cube for encapsulation with a grain of rice is placed in the centre of the polystyrene flat box. The rice can be encapsulated upon heating the polystyrene film with a light source and folding the hinges mechanically. The polystyrene box unfolds when reheated above T_g using a light source [70]. Although there are many other projects on light activated SMPs, the 3D printability of these polymers has yet to be seen [70-77]. A truly 4D printed light activated structure has not yet been reported. The use of light-activated SMPs may be the next step in 4D printing research.

2.3.4 Summary

Table 2 summarises current major 4D printing works in terms of printer, number of materials, type of stimulus, and more importantly, requirement of shape setting and design of smart structures.

Table 2. Summary on 4DP on SMP of water, heat and light activation

4D printed smart structure	**Printer**	**Material**	**Stimulation**	**Requirement of shape setting**	**Shape**	**Information on 4DP design**	**Ref**
Bar & disks structure & Grid	PolyJet	Multiple Stratasys Digital materials	Water	No		**Dimensions** Bar and disks: expands by 0.432 mm (from 0.813 mm to 1.245 mm) per disk Grid: 24cm X24cm X1.25cm	[45]
Flower	Bio-4DP	Single Hydrogel	Water	No	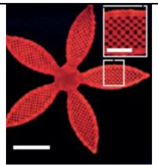	**Angles** bilayer lattice with a 90◦/0◦ & and −45◦/45◦ configuration	[53]
Origami Box & Pyramid & interlocking components	PolyJet	Multiple Stratasys Digital materials	Heat	Yes	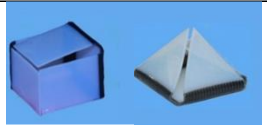	**Dimensions** Origami and pyramid box: **NIL** Interlocking: Thickness of SMP component is 0.6mm (0.8mm for the plate with holes) and the depth is 6mm. Five hinge sections (with a radius of 5mm in uniform)	[42], [47], [48]
Flower , Lattice structure& Flat star-shaped structure	PolyJet	Multiple Digital materials Grey60, Tangoblack, hydrogel	Heat	Yes	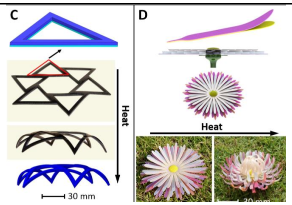	**Dimensions** Flower: SMP/elastomer thicknesses of all petals are 0.3/0.3 mm. Three different radii (42, 48, and 51 mm) are designed for petals in different layers Lattice: (180 mm × 25.2 mm × 7 mm) SMP/elastomer thicknesses are 0.35/0.35 mm Flat star-shaped: outer/inner side length of 60/44.4 mm. The SMP/elastomer thicknesses are 0.88/1.77 mm	[54]

Flower-themed rings and heel attachment	DLP 3D printing	Single Methacrylated PCL	Light	Yes		NIL	[55-62]

The difference between 4D printing of single material and multiple materials lies on their limiting factor of changes. In 4D printing of single material, the limiting factor is the smartness of the smart materials. Here the “smartness” refers to a combination of several intrinsic properties of a smart material, such as shape recovery quality, shape recovery rate and sensitivity to stimulus. It is this factor that determines how readily the printed single material components react upon activation. For the 4D printing of multiple materials, the extent of the changes in the multi-material components, especially changes in the overall shape, is usually determined by the design of the basic 4DP components (stretching, compression, bending, twisting, etc) and the complexity of the integral design of these basic components.3D printing of a single smart material is the basic form of 4D printing, where 3D printability of the material and the relationships among process, microstructure and material "smartness" need to be researched. 3D printing of multiple smart materials or a combination of smart materials and conventional materials requires both design knowledge, material knowledge and process knowledge, which currently represents the state of the art of 4D printing.

In real life applications such as sensors and actuators are implemented in a dry environment. Hence heat activation is more practical in applications that do not permit the use of water, such as electronic components which can cause short circuit. Secondly, heat also has a better controllability on sequential activation at different controlled glass transition temperatures, which is difficult to achieve by moisture absorption alone. Therefore, heat activated 4D printing is likely more often and hence heat activation is preferred over water activation. In heat activation, shape setting is a necessary and critical step. Although it is relatively easy to design and set shapes for simple smart structures such as of origami, fractures do occur during shape setting if the design of the smart structure is not appropriate. In addition, there is a strong link between smart structure design and complex response behaviour as discussed above. However, these are less explored in previous research works, as shown in Table 2 that limited design information is given and virtually there is no guideline provided. Thus developing design guidelines for heat activated 4D printing becomes necessary and important. More specially, the following works are needed in order to develop guidelines for designing 4D printed structures by heat activation: (1) to understand the relationship between smart structure design and fracture during shape setting; (2) to understand the relationship between smart structure design and response behaviour via heat transfer ; and (3) to increase design complexity for multistage folding.

In addition to guidelines for smart structure design, there are other challenges in 4D printing. For instance, in the area of technological limitation, one challenge faced is the inadequate availability of 3D printing technologies. As mentioned earlier, the developments in 4D printing mainly made use of PolyJet technology to fabricate multi-material components. PolyJet printers utilise UV light to cure liquid photopolymers to create the 3D structures. The starting form of the materials has to fulfil either of the criteria. The smart materials or smart composites have to be in liquid form and they must be curable by UV light for it to be printable by PolyJet. This would greatly limit the types of smart materials to be explored in the development of 4D printing as smart materials or smart composites that do not fulfil either criterion cannot be used. Moreover, the sensitivity of the smart materials is another limitation, and more research is required to overcome the issue of the sensitivity of the smart materials. Furthermore, the current mechanism of 4D printing relies on specialized materials and unique operating conditions. Therefore, new mechanisms which can operate at the room temperature in an ambient environment should be given more attention in the future.

2.4 Conclusion

In this chapter, 3D printing, shape memory polymers, and the developments in 3D printing of smart materials, also known as 4D printing, were reviewed together with some of the results from our ongoing research. These developments in 4D printing were classified according to the type of stimulus. Currently 4D printing is still a relatively new research area, although there are a few developments in this area. Therefore, 4D printing has a lot of challenges ahead. These challenges can be classified into three areas: mainly lack of design guidelines, technological limitation and material limitation.

CHAPTER THREE - DESIGN OF MULTIMATERIALS-BASED SMART STRUCTURES VIA FRACTURE AVOIDANCE

3.1 Introduction

In order to implement solutions to overcome the three key challenges in Chapter 2, it’s important to establish the design methodology for designing 4D printed shape morphing structures by heat activation. This chapter proposes two design methods: (1) quantifying the relationship between smart structure design and mechanical fracture characteristics during shape setting; and (2) allocating multimaterials at different levels of design to obtain complex response behaviours (e.g. biomimetic blooming effect or hierarchical morphing). A self-blooming flower is designed and fabricated according to the proposed methods. The biomimetic flower can be programmed without fracture and hierarchically morphed in an ambient environment. To avoid fracture during deformation of the printed flower, a mathematical model was developed to provide design guidelines on recommended thickness design parameters. To increase the complexity of 4D smart structure, four SMPs of different glass transition temperatures were used in three layers of flower petals for global sequential opening as well as within each single petal for local sequential morphing. Finally, the multistage and multi-level biomimetic blooming effect were demonstrated in a dry environment by using a hair dryer. This work has the potential to enable identification and optimisation of key design parameters to achieve multistage shape morphing in complex design structures.

3.2 Materials and method

3.2.1 Characterization of shape memory polymer

3.2.1.1 Dynamic mechanical analysis (DMA)

The materials used in the present research are based on two basic materials provided by Stratasys (USA) namely VeroWhitePlus and TangoBlackPlus (product codes from Stratasys). VeroWhitePlus is a hard and rigid material at room temperature while TangoBlackPlus is soft and rubbery at room temperature. TangoblackPlus liquid resin comprises urethaneacrylate oligomer, Exo-1,7,7-trimethylbicyclo hept-2-yl acrylate, methacrylate oligomer, polyurethane resin and photoinitiator; VerowhitePlus liquid resin consists of isobornyl acrylate, acrylic monomer, urethane acrylate, epoxy acrylate, acrylic monomer, acrylic oligomer and photoinitiator. The same materials were also used in a recent research [78].

Through mixing these two materials with different ratios, one is able to obtain materials of different glass transition temperatures (T_g). In the present research, we have used the following materials in our design: VeroWhitePlus, DM8510, DM8520 and DM8530. For each material, three specimens (17.5 x 12 x 2 mm^3) were printed using Objet500 Connex3 PolyJet printer (Stratasys, USA). TA Instruments Q800 DMA machine was used to determine the T_g temperature at a ramp of 3°C /minute to 100°C and a frequency of 1Hz under the testing of the single cantilever mode [79].

3.2.1.2 Tensile test

Three specimens of each material were printed along longitudinal direction and tested using Shimadzu Tensile Testing machine at 25°C, 50°C and 75°C at a strain rate of 0.0011 s^{-1}. For tests at 50°C and 75°C, each specimen was heated to the setting temperature and maintained for 15 min before starting the test. The dog-bone shaped specimen (180 x 20 x 3 mm) for tensile test was designed according to ASTM-D-638 and is schematically shown in Figure 21 [80, 81], which consists of two clamping ends and one gauge section (70 x 13 x 3 mm).

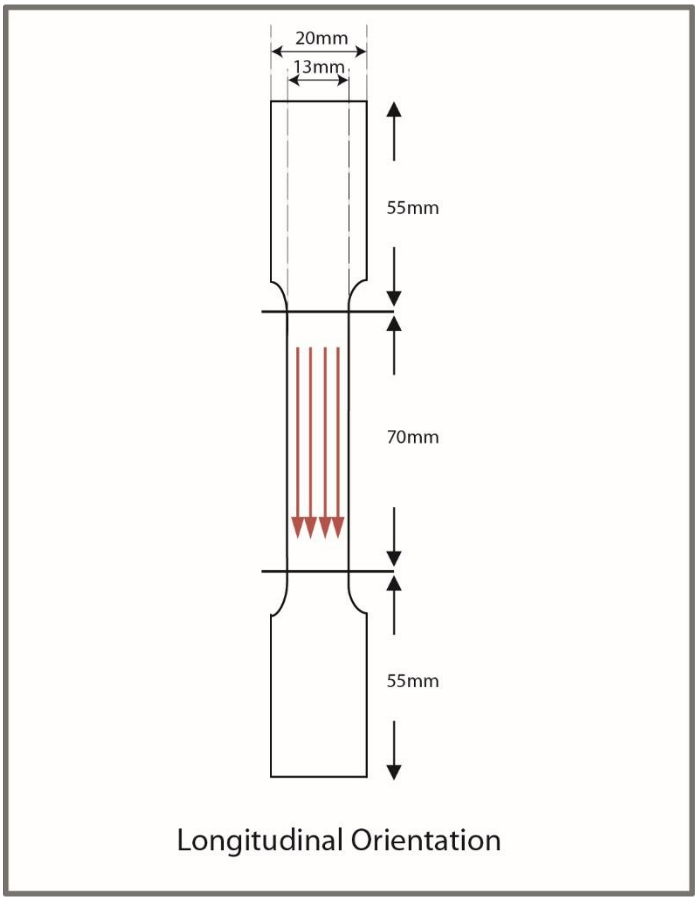

Figure 21. Specimen for tensile test (red arrows indicate the printing direction).Specimen thickness is 3 mm

3.2.2 Design and fabrication

The natural orchid flower Vanda Miss Joaquim was chosen as the sample flower for this research. Before designing, both the structure of the flower and its blossom characteristics were examined. The flower consists of three layers of six petals which bloom in difference sequences during rotation and unfolding from a closed bud to a fully bloomed flower. The design was drawn using Solidworks based on the actual flower and saved as STL file (*.stl) to be loaded into PolyJet Studio software. Materials of different T_g temperatures were assigned to different layers of the flower as well as to different locations of each petal to ensure proper shape-morphing sequence for flower blooming.

3.2.3 Programming and demonstration

After printing, flower petals were painted with colours for enhanced visual effect, however, colours could be printed instead if needed. Then the flower was immersed in 75°C water for one minute where all petals were slowly folded manually in all directions into a bud. After that, the programmed bud was taken out and cooled down at the room temperature. To demonstrate self-blooming, the flower bud was placed on an artificial grass pad and blown with hot air from a hand-held hair dryer to increase the temperature of the flower to above T_g temperatures of its components.

3.3 Results and discussion

3.3.1 Characterization of shape memory polymers

Each material used in the flower is a mixture of two basic components: VeroWhitePlus and TangoBlackPlus (product codes from Stratasys, USA). At different mixing ratios, the property of the material such as T_g can be tailored. Table 3 shows the T_g temperatures of four materials used in this research (See Appendix for original DMA graphs). Material DM8530 has the lowest T_g, suggesting that material DM8530 has the highest content of TangoBlackPlus compared to materials VeroWhitePlus, DM8510 and DM8520. With a higher T_g, a material will respond to heat stimulation more slowly. Therefore, the graded T_g in these four materials allow designing of sequential responses, which essentially form the basis of sequential self-morphing of the multi-material flower petals.

Table 3. Glass transition temperatures of four materials used in the present research

Material	**Tg (^{0}C)**
VeroWhitePlus	55.6
DM8510	53.5
DM8520	51.6
DM8530	47.4

Figure 22 shows the typical stress-strain curves of DM8510 at 25°C, 50°C and 75°C. The other three photopolymers showed similar curves with slight differences in ultimate tensile strength (UTS) due to different rubbery contents, hence they are not shown in the figure. From Figure 22, it can be seen that at 25°C, the material experienced elastic and plastic deformation. Meanwhile the specimen is rigid and has high yield stress and the fracture strain is small. At 50°C and 75°C, the temperatures are either close to the T_g or above the T_g of DM8510, making specimens soft and rubbery, therefore there was a tremendous decrease in UTS and a notable increase in maximum fracture strain. The graphs also show that the specimens had a smaller fracture strain at 75°C than they did at 50°C, which could be due to that the materials became very soft at 75°C and failed at the clamping area.

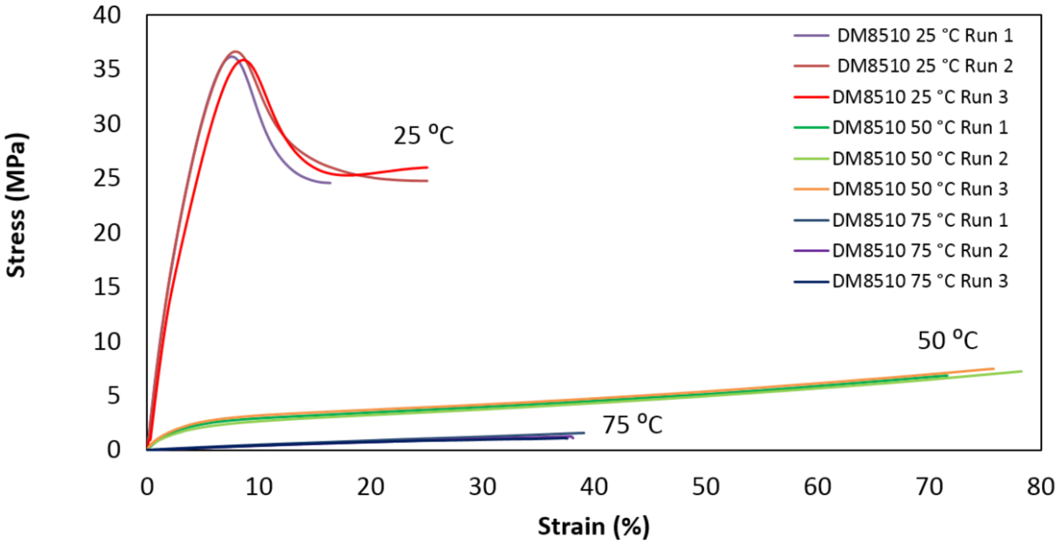

Figure 22. Stress-strain curve of material DM8510 at 25°C, 50°C and 75°C

3.3.2 Design of the flower

3.3.2.1 Thickness consideration

Shape-setting for 3D printed structures is a necessary step in 4D printing of SMPs and it involves bending of flower petals to form a bud. During shape-setting procedure, fracture of the 3D-printed SMPs was not uncommon. To avoid fracture during bending flower petals, the radius of curvature of the bending location must be carefully designed. The fracture of the material during shape-setting process is determined by the maximum strain allowable on the outer surface of the material which is further related to the radius of curvature and thickness of the material at the bending point.

Figure 23 shows a strip of sheet material with a thickness t and an original length L_0 being bent at an angle of θ. R is the outer radius, r is the inner radius, and r_n is radius to neutral axis, where

$$r_n = r + \frac{t}{2} \tag{1}$$

Assuming that after bending, the bending length L_n at the neutral axis does not change and equals to L_0, hence we have

$$L_0 = L_n = r_n \cdot \theta \tag{2}$$

The strain at the outer surface can be calculated as follows:

$$\varepsilon_R = \frac{(L_R - L_0)}{L_0}\text{, where } L_R = R \cdot \theta \tag{3}$$

Substituting (1) and (2) into (3), we have

$$r = \frac{\left(\frac{1}{\varepsilon_R} - 1\right)t}{2} \tag{4}$$

From equation (4), it can be seen that bending angle θ is cancelled and not a determining factor. The bend radius r is a function of strain at the surface and the thickness, and the allowable minimum bend radius before fracture depends on failure strain and thickness. Since the failure strain of a material at a defined temperature can be determined experimentally and is a constant, the parameter that can be altered to avoid fracture is thickness. However, it should be noted that geometrically, r is within (0, ∞), which limits ε to be less than 100%. Equation (4) is not applicable to material that can be bent at a strain greater than 100%.

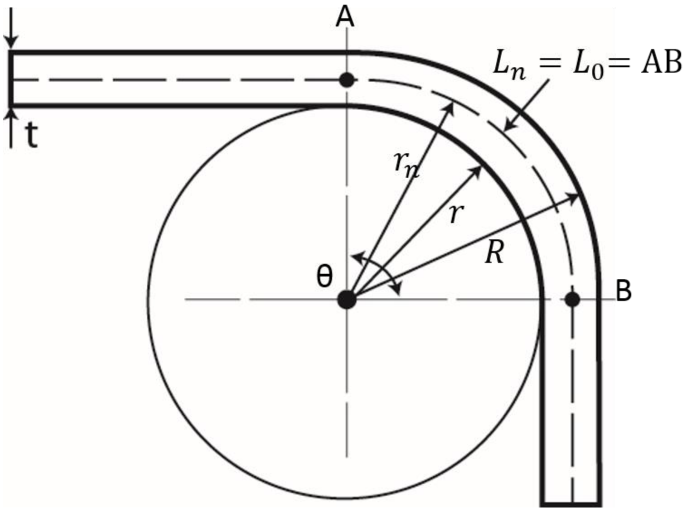

Figure 23. Bending schematic of a sheet material

Based on the failure strain data obtained from mechanical tests at 50°C, graphs of minimum bend radius versus thickness can be plotted (Figure 23). From a pragmatic point of view, the smaller the minimum allowable bending radius is, the safer will be the component during bending operation. This means that it is safer to design the thickness at the bending location as thin as allowable. Figure 24 also shows that materials VeroWhitePlus and DM8530 would be prone to fracture in comparison with DM8510 and DM8520, since they have larger critical radius values. On the other hand, the lower boundary of thickness design is limited by the printability of the PolyJet printer, which is about 0.1 mm. If a material is too thin, it may not survive the manual handling after printing.

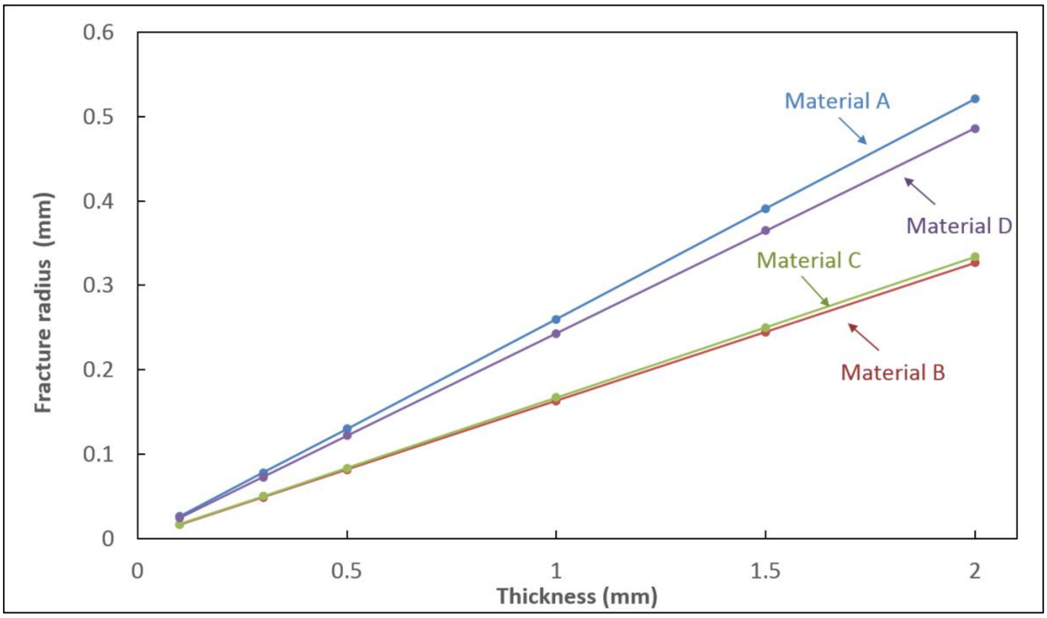

Figure 24. Allowable minimum radius of curvature at fracture versus thickness for four materials at 50°C

The flower was designed in free-form with specific allocation of materials for the petals. The design input was listed as bending radius to avoid breakage during shape-setting. The complex shape recovery consists of shape changing within each petal as well as relative movement between petals. The former is defined as the local response and the latter is defined as the global response. There are two basic considerations when allocating these materials. One is thickness. The thickness of a flower petal decreases from the proximal area to the distal area. Different thickness causes different heat transfer behaviours and hence different respond times (or sequential unfolding). In chapter 3, the flower petal was designed with a constant thickness, optimized from the principle of fracture avoidance. In chapter 4, the flower petal will be designed with a thickness variation to demonstrate the principle of geometric control on 4D printing. The other is T_g. When the flower was placed in hot water (above the T_g of all the allocated materials), all the materials start to respond. However, materials with the lower T_g are allocated for structures that were intended to respond earlier when heat was applied. While materials with the higher T_g are allocated to structures which were intended to respond later.

3.3.2.2 Allocation of multiple SMPs for hierarchically self-morphing

A natural orchid flower Vanda Miss Joaquim generally consists of three layers (Figure 25a) [82]. At the bottom layer, there are three sepals. Two are lateral sepals which similar to each other while the third one is a dorsal sepal. There are also three petals, two in the middle layer and one at the top layer. The top layer petal is also known as labellum which not only rotates but also unfolds locally during blossom. These three sepals, two petals and a labellum are three major parts of the flower and have significant shape changes during blooming of the entire flower. Figure 25b and Figure 25c present the computer-aided design based on the three-layer structure of the orchid flower. The sepals and petals are labelled with P1-P6.

Figure 26 (a-c) shows the designs of bottom layer (P1, P2 and P3), middle layer (P4 and P5) and top layer (P6) of the flower, respectively. The locations of different SMPs were determined based on the opening sequence of each layer and each petal to prevent collision of the petals when blooming. For example, DM8520 and DM8530 have relatively lower T_g, therefore they are selected for bottom layer which opens the fastest during heating (Figure 26a). DM8530 is placed closer to the stem while DM8520 at the tip of each petal, meaning that petals P1-P3 will open faster at the stem than the tip. Similarly, the other petals are designed with multiple SMPs using the same strategy. Figure 26(d)-(f) shows the side view of the three layers. The thickness of each petal is designed as a constant of 1.5 mm.

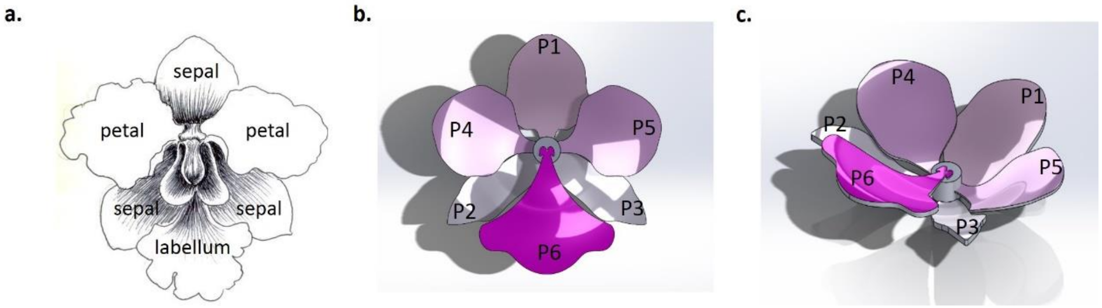

Figure 25. Overall flower design. (a) An actual orchid flower. (b) Top view of the flower design and (c) isometric view

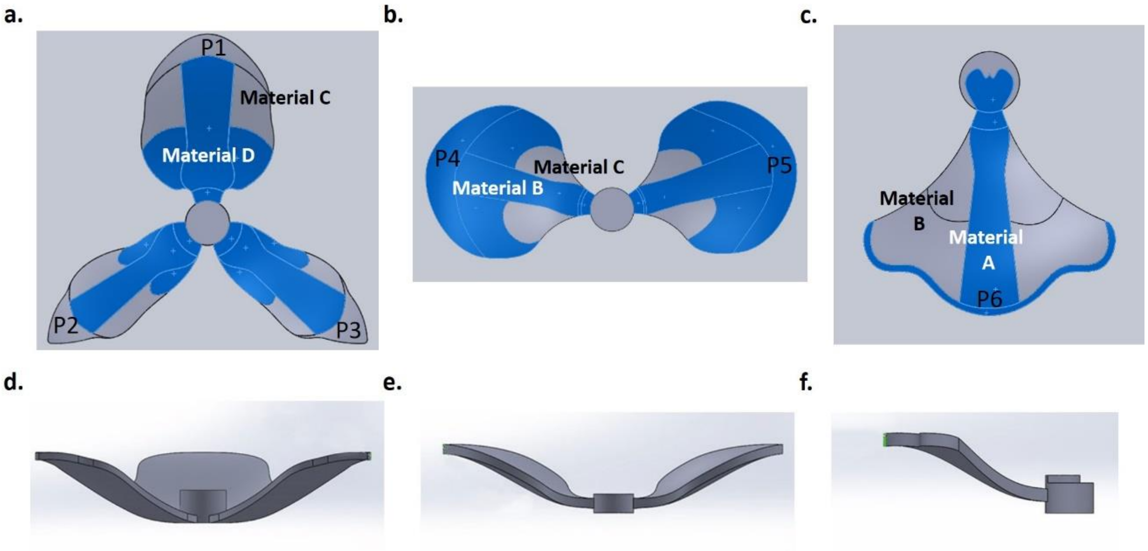

Figure 26. Allocation of materials for local and global response. (a) Three petals (P1, P2 and P3) at the bottom layer made of DM8530 and DM8520. (b) Two petals (P4 and P5) in the middle layer made of DM8520 and DM8510. (c) One petal at the top layer made of DM8510and VeroWhitePlus. (d)-(f) Side views of (a)-(c)

3.3.3 Self-blooming test in an ambient environment

Figure 27 shows the blossom of the artificial flower bud activated by thermal stimulation with a hair blower. The as-printed flower was painted with colours using markers and programmed to a temporary bud. In Figure 27(c), the flower at different blooming stages was captured from the video and put together into one image. It can be seen that three layers of the flower unfolded sequentially upon heating, with bottom layer opening the fastest and top layer the slowest, giving a visual impression of the natural blossom. Moreover, the curved petals became less curved or flattened over time, indicating the concurrent local morphing events. The entire opening process with hair dryer took 2 minutes and 45seconds. This would, of cause, depend on the temperature and air flow rate of the hair blower and its distance to the flower. It also depends on the T_g temperatures of the flower components and their thicknesses as a result of associated heat transfer.

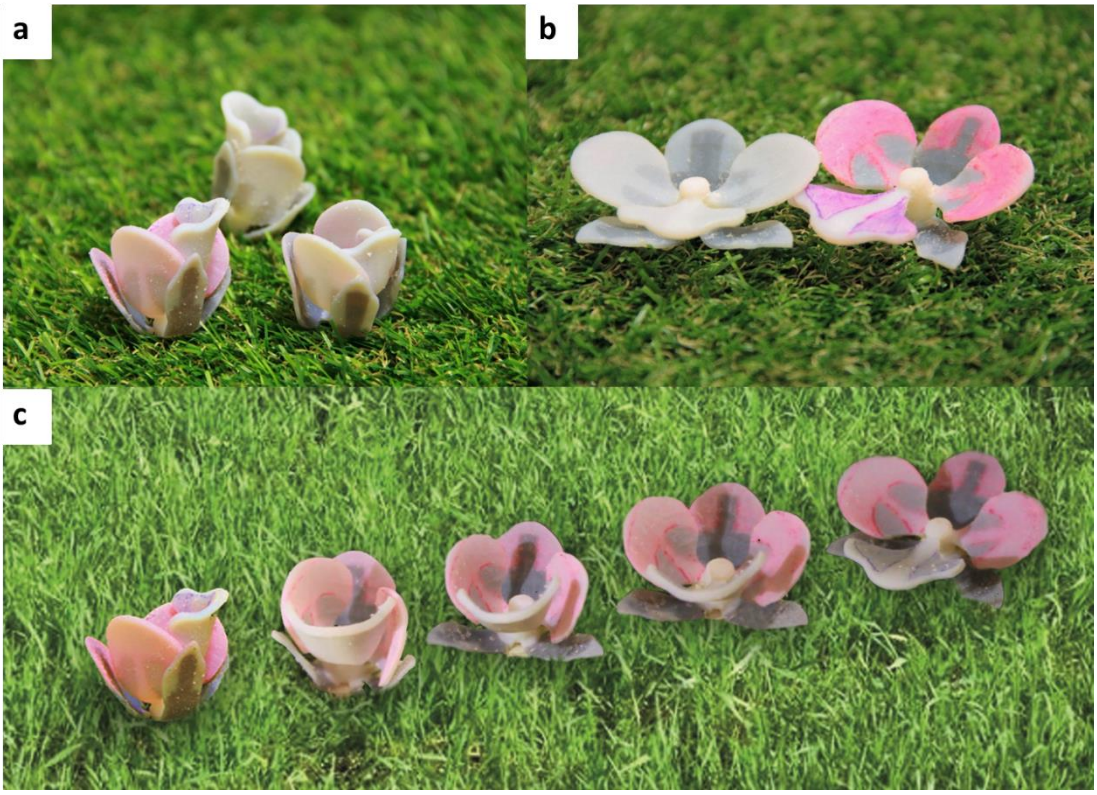

Figure 27. Blossom of the artificial flower thermally activated with a hair dryer, (a) Flower buds through shape setting, (b) fully bloomed flowers and (c) Snapshots showing sequential views (from left to right) of hierarchically morphing process

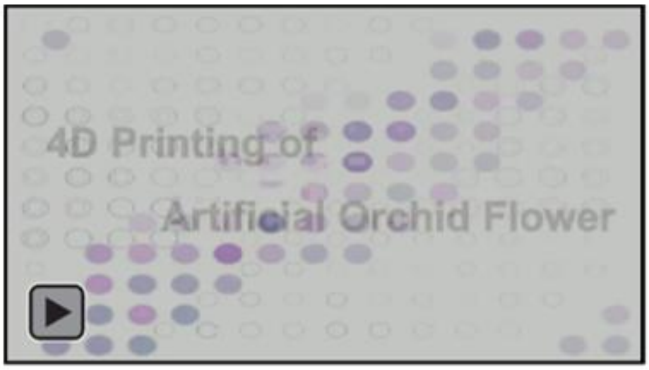

Video: Multimaterials, multistage sequential opening of Orchid flower

Recently, it has been reported that a biomimetic flower has also been 4D printed [10]. However, the reported design of the flower is very simple as it consists of only a single material and a single layer of petals. Moreover, the material used for printing the flower can only be activated in a water environment which limited its applicability in dry environment. On the other hand, a 4D printed multi-material flower has also been reported very recently [83, 84]. However, the design of multiple SMPs was not at the local level and the self-opening occurred only at the global level.

In this research, the self-morphing process started from one 3D configuration (flower bud) and ended at another 3D configuration (fully bloomed flower). The shape setting between two 3D configurations was performed manually, which had poor controllability and accuracy. Hence this is one limitation to be overcome in the future. A special mould may be designed to precisely control the shape setting process from one 3D configuration to another. Also in this research the flowers were coloured after 3D-printing. For better artistic effect, colourful flowers could be directly printed by using the most recent PolyJet printer (Model: J750), which can print six materials and allow full colour printing.

3D printing has an established wide range of industrial and biomedical applications [85]. Though 4D printing is recent and new, it has already been applied for making robotic grippers [84, 86], actuators and soft robots [83, 87-89], medical device such as stent [90], and flexible electronic devices [91]. The knowledge of hierarchical 4D printing gained from this research could be extended to structures where hierarchically self-morphing down to component level is required. The potential applications may include self-healing automotive structure, architectural kinetic façade and deployable space structures.

3.4 Summary

Hierarchical self-morphing structures involve concurrent sequential shape-changing (multistage folding) at both the system (global) and component (local) levels. By carefully determining minimum allowable bend radius and selectively deploying different SMPs at both global and system levels, a hierarchically self-morphing artificial orchid flower which was thermally activated to blossom in an ambient environment was successfully printed. The design principle for selecting proper thickness would be useful for other 4D printing approaches to avoid material fracture during shape-setting stage. The approach of hierarchical 4D printing may be used for a variety of applications that involve controlled, self-morphing complex structures.

CHAPTER FOUR - DESIGN OF GEOMETRY-BASED SMART STRUCTURES VIA HEAT TRANSFER

4.1 Introduction

This chapter proposes using a geometric parameter such as thickness as a control factor to increase design complexity. Geometric effect is important in designing smart structures in 4D printing, as the response behaviours of smart structures are not only dependent on the materials or the number of materials but also how the materials are implanted in geometric design. Smart structures made of the same material but different geometric design implementation will have different response behaviours. However, implementation of this novel design methodology requires a thorough understanding of heat transfer in 4D smart structures in relation to their self-response behaviours. Therefore, Ansys workbench transient thermal simulations were performed to estimate response times for samples with different thicknesses. A new method has been designed specifically for accurate measurement of SMP's fast shape recovery. In this research, SMPs produced from Stratasys were used. L-hinges and spiral square were designed and fabricated. It was demonstrated that by using material thickness as a controlling factor, even a single material could achieve multistage sequential shape morphing. When a single material is capable to achieve as much as when multiple materials were previously used, the achievable complexity of shape morphing will be unlimited.

4.2 Material and methods

4.2.1 Materials

The materials used in this research are based on two basic proprietary materials provided by Stratasys (USA), namely TangoBlackPlus (TB) and VeroWhitePlus (VW). Compared to TB, which is rubbery and has a great extent of elongation, VW is a rigid and opaque material that has high Young’s modulus, great tensile strength and 10-25% of elongation before break. Through mixing of these two materials, new materials possessing different glass transition temperatures (T_g) can be obtained. In this research, four materials, VW and three mixtures from VW and TB (DM8510, DM8520 and DM8530) were used. All three mixtures are Stratasys’ proprietary digital materials (DM), with VW as the primary component and TB the secondary component. The percentage of TB in each is not released by Stratasys, but the order is known as follows: DM8510 < DM8520 < DM8530 (highest percent of TB) [92].

4.2.2 Design and fabrication

L-hinges with variable thicknesses (Figure 28a) were designed in CAD software and converted to stereolithography files for 3D printing. All specimens (3 for each thickness) were fabricated with Stratasys’ PolyJet (Model: Objet500 Connex3). The as-printed specimens were used directly for experiments without post-processing. All specimens had an original L shape. After being placed in a hot water bath (~98 °C) above their T_g temperatures, they were programmed into a temporary straight and flat shape. When heat stimulus was applied again, specimens recovered from flat shape back to their original L shape. Apart from L-hinges, a spiral square containing 8 hinges of variable thicknesses (0.5 mm, 1 mm, 1.5 mm and 2 mm), was designed and printed to demonstrate single material multistage recovery (Figure 28b). An even thickness of 2 mm was used for the flat connection part. The printed spiral square was then programmed in a hot water bath into a straight strand before being stimulated to recovery. To further demonstrate the effect of thickness manipulation on response time in a complex structure, Vanda Miss Joaquim, the national flower of Singapore, was designed and fabricated with different thicknesses of the flower components (Figure 28c). The printed flower mimicked the real orchid by having 1 labellum (top layer), 2 petals (middle layer) and 3 sepals (bottom layer).

The material used for printing was a mixture of VW and VeroMagenta (VM), still a single material. The addition of VM is for colouring the flower in pink.

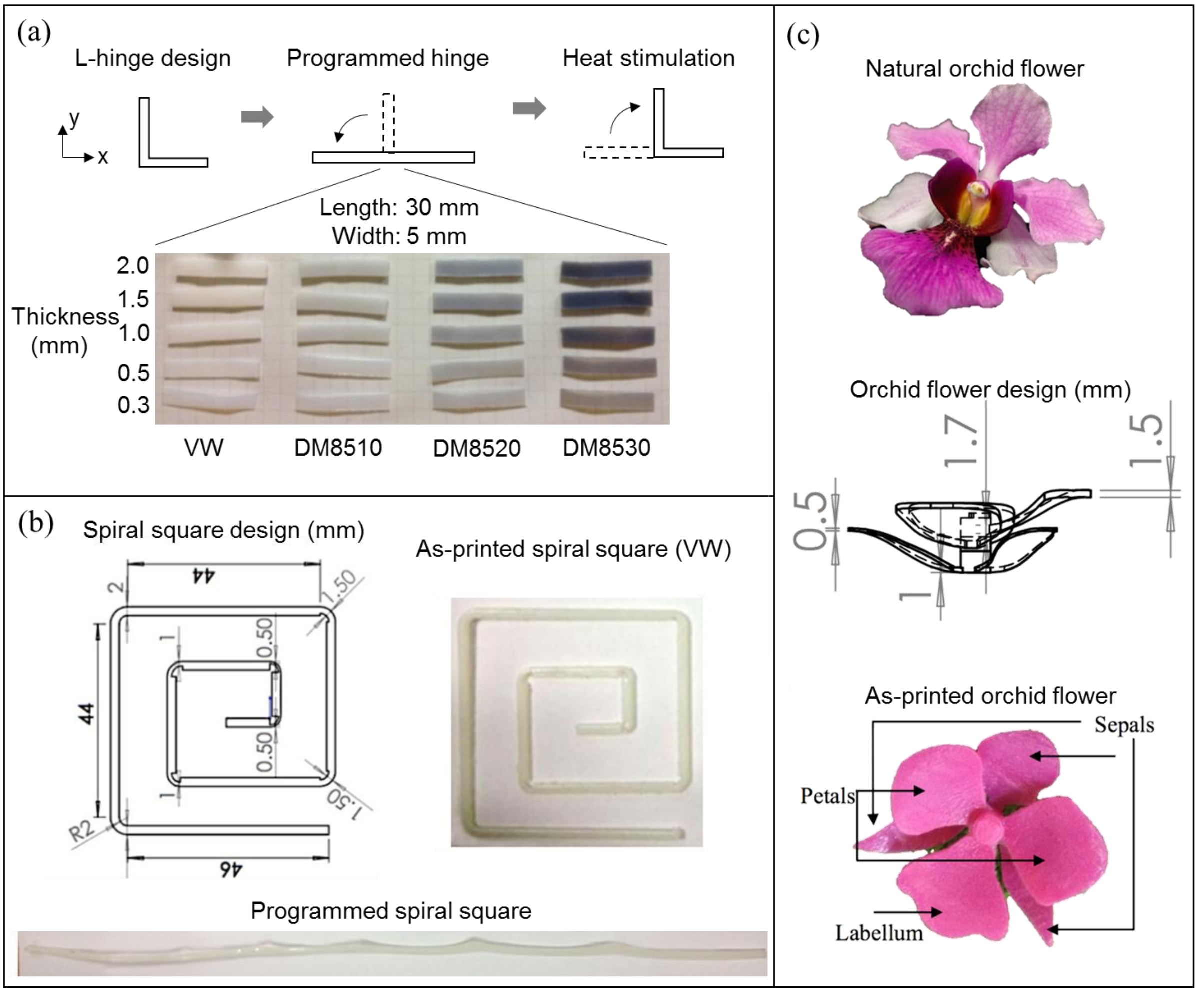

Figure 28. Design and 3D printing of single material smart structures with thickness variation (a) L-hinges (b) Spiral square and (c) Orchid flower

4.2.3 Measurement of shape recovery

After programming, each flat L-hinge specimen was clamped with nuts and placed in a plastic tray under a stereomicroscope. A digital camera was connected to a computer with software (AmScope) to record the whole recovery process (Figure 29). A piece of grid paper was inserted below the plastic tray as reference for measurement. A layer of styrofoam was inserted between the tray and table as insulator to minimise heat loss. Boiling water was added to the tray and water temperature was monitored at 75 ± 1 °C during the video recording. The water bath dimension is (80 mm × 40 mm × 15 mm). Video sequence editor function in Blender was used to break each recorded video from time domain into frame domain so as to clearly identify starting and finishing points of recovery. By counting the total number of frames during the recovery period in Blender and converting them back into time domain, an accuracy of millisecond was achieved and clear movement for each frame was obtained. For example, for VW specimen of 1.0 mm, a video of 11.082 second was recorded, which corresponds to a total of 52 frames in Blender. The recovery period was identified from the 24th frame to the 40th frame, which was equivalent to 3.62 seconds in total when converted back to time domain.

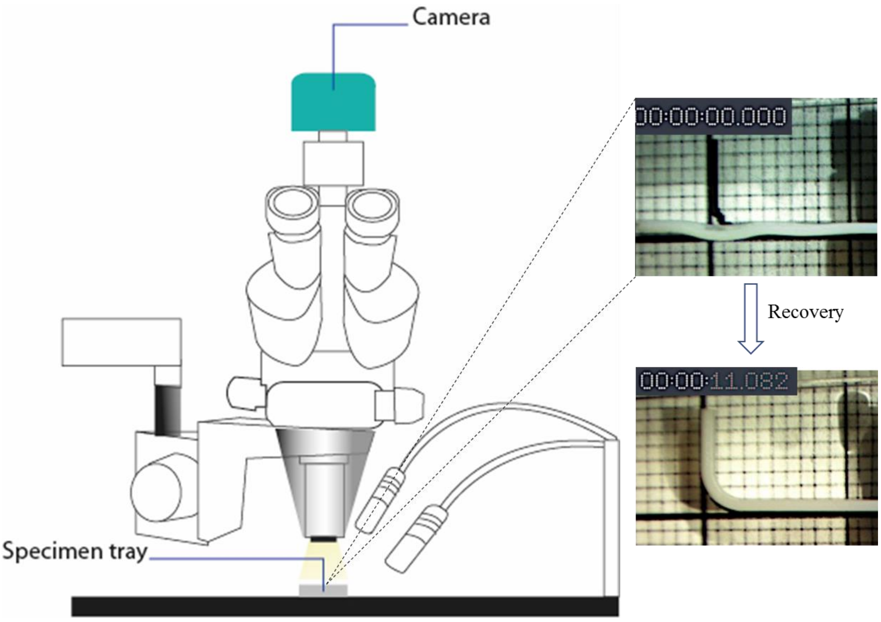

Figure 29. Setup for recording shape recovery of L-hinge samples

4.2.4 Thermal analysis and simulation

4.2.4.1 Material density and thermal conductivity

No information is available from Stratasys for the proprietary digital materials. Since the present digital materials are mixtures of VeroWhitePlus and TangoBlackPlus, their thermal property values should fall between those of VeroWhitePlus and TangoBlackPlus, respectively.

As the glass transition temperatures of the investigated materials are directly related to the volume fraction of VeroWhitePlus and TangoBlackPlus, linear interpolation method was used to obtain digital materials' density values based on their glass transition temperatures. Similarly, linear interpolation was used to obtain digital materials' thermal conductivity values based on their glass transition temperatures.

4.2.4.2 DSC to determine material specific heat capacity

Since specific heat capacity is temperature dependent, linear interpolation is not appropriate. Hence, advanced Differential Scanning Calorimetry (DSC) tests using the ASTM E1269 standard were conducted for VeroWhitePlus and all other tested materials. The specific heat capacity c_p values were determined using the DSC Q200 (TA Instruments). The mass for each test sample was approximately 13 mg. By performing the sapphire calibration and setting the temperature rate at 2.5℃/min, heat flow curves were obtained and specific heat capacity as a function of temperature was determined.

4.2.4.3 Ansys simulation

Ansys workbench (Ver 18.1) transient thermal simulation was used for modelling heat transfer and temperature distribution in L-hinges and spiral square during the recovery period. Since there is no digital material data in Ansys, we modified from the general materials (polyethylene) provided in the Ansys transient thermal software and input the values of density, thermal conductivity and specific heat capacity from the respective digital materials, VW, DM8510, DM8520, DM8530 and TB. For simulation environment, recovery processes of L-hinges and spiral square were simulated in a water bath (80 mm × 40 mm × 15 mm). Initial temperature of the model was set at 22 °C. Convection was selected as the mode of heat transfer with all the L-hinge and spiral square surfaces chosen to be contact surfaces. Since ambient fluid is stagnant water, film coefficient was set at 1200 W/m^2 °C. Ambient temperature was set to 75 °C, the same as the temperature of the hot water bath. For spiral square, the ambient temperature was set at 81 °C during simulation.

For general multidimensional transient thermal analysis, determination of temperature variation as a function of time and position $\mathrm{T}\,(\mathrm{x},\mathrm{t})$ within the heat conducting body is the primary function. Generally, studies on conducting bodies are of three-dimensional Euclidean space in a suitable set of coordinates ($\mathrm{x} \in \mathrm{R}^3$) and the aim is to define the development of temperature field for $\mathrm{t} > 0$ [93]. The general heat equation is shown below:

$$\rho C_p \frac{\partial T}{\partial t} = \nabla \cdot (\mathrm{k}\nabla\mathrm{T}) + \mathrm{g}(\mathbf{r}) \qquad \text{Eqn.(1)}$$

ρ: density (kg/m^3)
C_p: specific heat capacity J/kg°C
∇T: ∇T is the vector differentiation i.e. $\nabla\mathrm{T} = \partial\mathrm{T}/\,\partial\mathrm{x} + \partial\mathrm{T}/\,\partial\mathrm{y} + \partial\mathrm{T}/\,\partial\mathrm{z}$
k: thermal conductivity (W/m°C)
$\mathrm{g}(\mathbf{r})$: heat generated at location vector **r**

In the present case, the problem can be simplified into two one-dimensional problems. The L-hinge can be dissected into 1 vertical slab and 1 flat slab. The heat transfer is hence simplified into one-dimensional solely in the thickness direction. The multidimensional problem is reduced to a homogeneous problem of predicting the one-dimensional temperature distribution inside a thin slab. The thickness of the slab is 2L and the thermal diffusivity is α, where α is defined as:

$$\alpha = \frac{k}{\rho C_p} \qquad \text{Eqn.(2)}$$

α is assumed to be invariant with temperature.

Given comparable k and ρ, according to above material property to heat transfer relationship, specific heat capacity determines the heat transfer rate for response time materials. According to this heat transfer model, given similar ρ, k, and $\mathrm{c_p}$, heat transfer rate for L-hinges should be similar and they should reach similar temperatures at the same time when heated in a water bath.

4.3 Results and discussion

4.3.1 Ansys transient thermal analysis

4.3.1.1 Material parameters for ansys simulation

In this research, VW, TB and three mixtures were printed in the form of L-hinges and a spiral square to demonstrate the effect of thickness on recovery time and thickness-induced multistage shape morphing. For Ansys simulation, material property values such as convective heat transfer coefficient (h), material density (ρ), thermal conductivity (k), and specific heat capacity (c_p), are critical input parameters. However, Stratasys' materials are proprietary and most of the material property values are not available. Hence reasonable assumption and linear interpolation were used to obtain respective material property values.

For natural convection of water, heat transfer coefficient is within the range of 284 to 1500 W/m^2 °C [94]. The exact value depends on several factors, for instance, the friction at the heat transfer surface [95]. In this research, the value of 1200 W/m^2 °C was chosen from Ansys simulation predefined data for stagnant water.

Table 4 shows the estimated material density and thermal conductivity values used in the Ansys simulation. Tg temperatures of VW, DM8510, DM8520 and DM8530 was reported previously in [11] and Tg of TB was reported in [96]. Densities and thermal conductivities of VW and TB were taken from [97]. By interpolation against Tg temperatures, densities and thermal conductivities of digital materials were obtained.

Table 4. Values of density and thermal conductivity of digital materials taken for Ansys simulation.

Material	Tg (°C)	Density (kg/m^3)	Thermal Conductivity (W/m °C)
VeroWhitePlus	55.6	1180.00	0.2376
DM8510	53.5	1178.47	0.2371
DM8520	51.6	1177.05	0.2370
DM8530	47.4	1173.91	0.2365
TangoBlackPlus	-10	1130.00	0.2307

Differential Scanning Calorimetry (DSC) tests were conducted to determine specific heat capacity values as a function of temperature (Figure 30). In the Ansys simulation, specific heat capacity of each material was input as tabular data across test temperature range. Stratasys provides specific heat capacity for VeroWhitePlus as 1470 J/kg°C and for TangoBlackPlus 1950 J/kg°C [98]. However, the temperature at which the value is obtained is not given. From the DSC results, the reported specific heat capacity value for VeroWhitePlus is similar to what was obtained at room temperature, as shown in Figure 30. The main peak exhibits the materials glass transition temperature T_g, as more heat is absorbed during glass transition, resulting in a higher specific heat capacity.

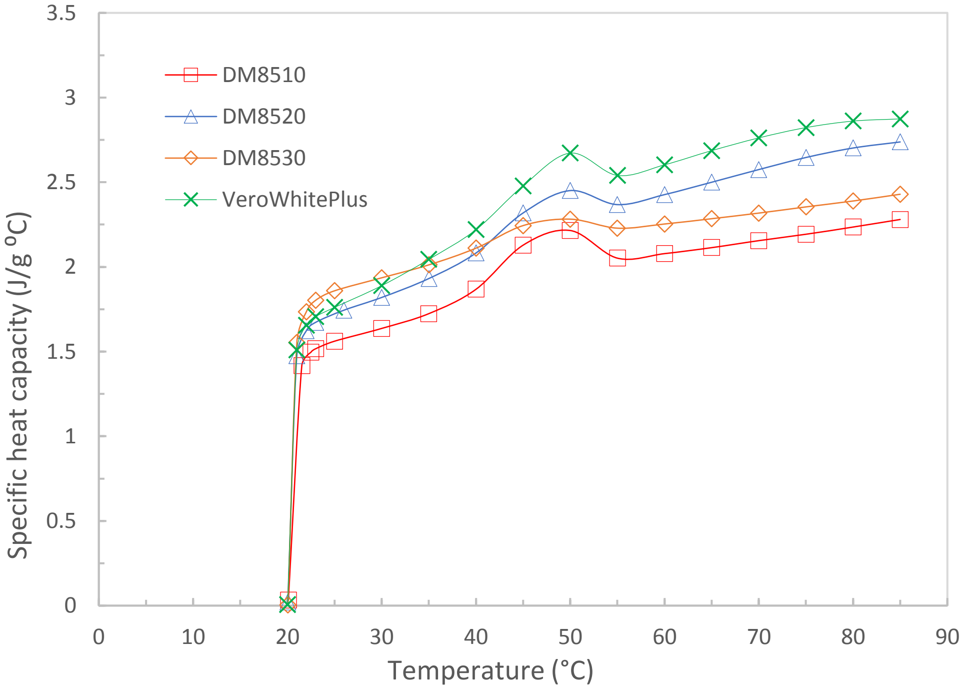

Figure 30. Specific heat capacity versus temperature for four materials tested

4.3.1.2 Full recovery temperature and time

In order to determine the full recovery time in simulation, it is important to determine the full recovery temperature. For consistency, in this research the full recovery temperature is defined as the extrapolated end temperature on the storage modulus curve [94]. Average values from three sets of DMA results for each material were taken and the full recovery temperatures of the tested materials are shown in Table 5.

Table 5. Full recovery temperature determined based on DMA results

Material	Full Recovery Temperature (°C)
VeroWhitePlus	68.3
DM8510	63.7
DM8520	60.4
DM8530	55.9

With respect to the temperature distribution in the L-hinge, the lowest temperature should occur at the interior centreline position. Thus, a full recovery should occur when the temperature at the centreline reaches the critical temperature for shape recovery, and the time taken for such temperature rise should be the time for full shape recovery. It is not thermal equilibrium as the environmental temperature is much higher than the temperature required for full recovery. Since the time is discretized in simulation by pre-defined step size, linear interpolation is used to determine the time needed to reach exact full recovery temperature. The nearest lower and upper temperatures to full recovery temperature were taken for linear interpolation. For example, full recovery time for VW was 68.28 °C. Recovery times for the nearest temperatures 66.457 °C and 68.447 °C were taken. Linear interpolation was used for this small temperature range to determine the time to reach 68.28 °C. For hinge thickness of 0.3mm, the time taken for full recovery was then determined to be 0.921s. Similar practices were conducted to determine full recovery times for hinges of other thicknesses (0.5 mm, 1.0 mm, 1.5 mm and 2.0 mm) for all the tested materials.

4.3.1.3 Surface temperature over time

During the recovery, heat was lost from water bath to surrounding air, which could decrease the ambient temperature of the sample (water bath temperature). For better simulation accuracy, this decrease in water temperature needed to be captured. Therefore, a separate simulation was performed for hot water bath. The volume of the sample with thickness of 2 mm was 300 mm^3 and the volume of the water bath was 48,000 mm^3. Therefore, the volume of the sample is about 0.6% of the volume of water so this did not affect the temperature. Since the bottom of the water bath surface was insulated by styrofoam from the metal plate to minimise heat loss, the bottom surface was modelled as insulated surface. The rest 5 surfaces were subject to natural convection with stagnant air of heat transfer coefficient of 5 W/m2 °C at 22 °C. The results were given in terms of water bath maximum and minimum temperatures against time. Average values of maximum and minimum temperatures were taken for L-hinge model simulation. For L-hinge ambient temperature (water bath temperature), water bath temperature was input as tabular data across the time range. Simulation was then performed for L-hinge and temperature distribution was solved. Similar transient thermal model is used for the spiral model as well. The simulation was designed similarly with the specimen inside a hot water bath to be activated by heat stimuli shown in figure 31.

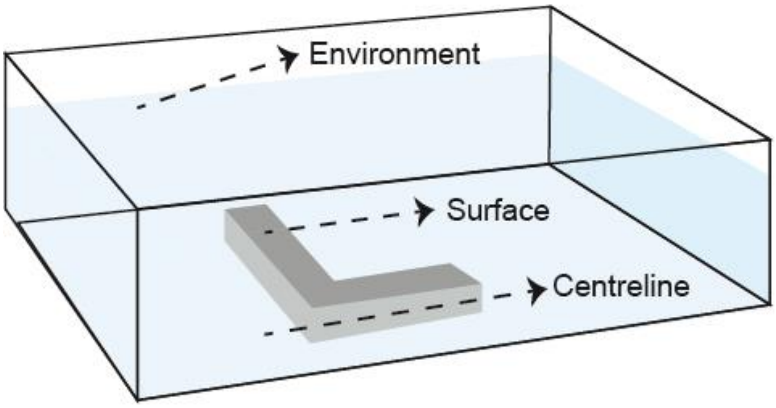

Figure 31. A schematic of L-hinge in a hot water bath with different surface temperature distribution

4.3.1.4 Heat transfer in digital materials

In heat transfer context, it is a three-dimensional transient thermal problem which can be further divided into two parts. The first part is the natural convection between the stagnant water and the solid model (sample). The water acts as the heat source and provides heat flux into the model, which defines the boundary conditions at the model's surfaces. The second part is conduction within the model. A brief description of the model is in Section 2.4.3. This heat transfer model was developed mainly to explore if other inherent properties of digital materials such as thermal conductivity, density and specific heat capacity would affect heat transfer rate and hence lead to differences in response time. However, although VW, DM8510, DM8520 and DM8530 have different glass transition temperatures, they share similar values in thermal conductivity, density and specific heat capacity. Therefore, according to the heat transfer model we developed, given the same thickness, the changes of centreline temperatures over time in digital materials were similar to those shown in Table 6. The material effect on heat transfer rate was not found. It should be noted that this did not contradict the material effect on response time as observed in Figure 32, which is due to the difference in glass transition temperatures. Hence the conclusion is that digital materials have similar centreline temperature variation over time due to similar heat transfer rate, but they have different response time for full recovery.

Table 6.Simulation of centreline temperatures at different time for hinge thickness of 1.5mm.

Time (s)	VeroWhitePlus Minimum Temperature (°C)	D8510 Minimum Temperature (°C)	D8520 Minimum Temperature (°C)	D8530 Minimum Temperature (°C)
0	22.0	22.0	22.0	22.0
1	26.8	29.0	27.6	26.9
2	37.9	40.5	38.6	37.9
3	46.0	48.1	46.2	46.0
4	52.2	54.4	52.0	52.3
5	57.3	59.3	56.8	57.3
6	61.1	63.0	60.5	61.2
7	64.2	65.8	63.4	64.2

4.3.2 Experimental Results

4.3.2.1 L-hinges

Figure 32 shows the recovery angle vs. response time for a 1.5 mm thick VW specimen. The angle of recovery refers to the acute angle between the horizontal part and the recovering part of the L- hinge. Samples with thicknesses less than 1.5 mm are not analysed as the recovery was too fast to obtain accurate time readings. When chopped into frames in blender, it is in the middle of movement causing the capture to be very blur. For example, in Section 2.3, we mentioned that for 1 mm thick sample, there are only 17 frames (start to end of recovery) for the duration of 3.62 seconds. As a result, the start and end frames are clear to view though, the frames in-between are blur due to fast movement, unable to accurately measure the recovery angle and hence difficult to convert back to accurate time domain. However, the other specimens (thickness above 1.5 mm) show similar trend in data plots. The recovery was faster initially and became slower towards the end of recovery. When the L-hinge recovered to the vertical line marked on the grid paper, a recovery angle of 90 degree was reached and the hinge was fully recovered.

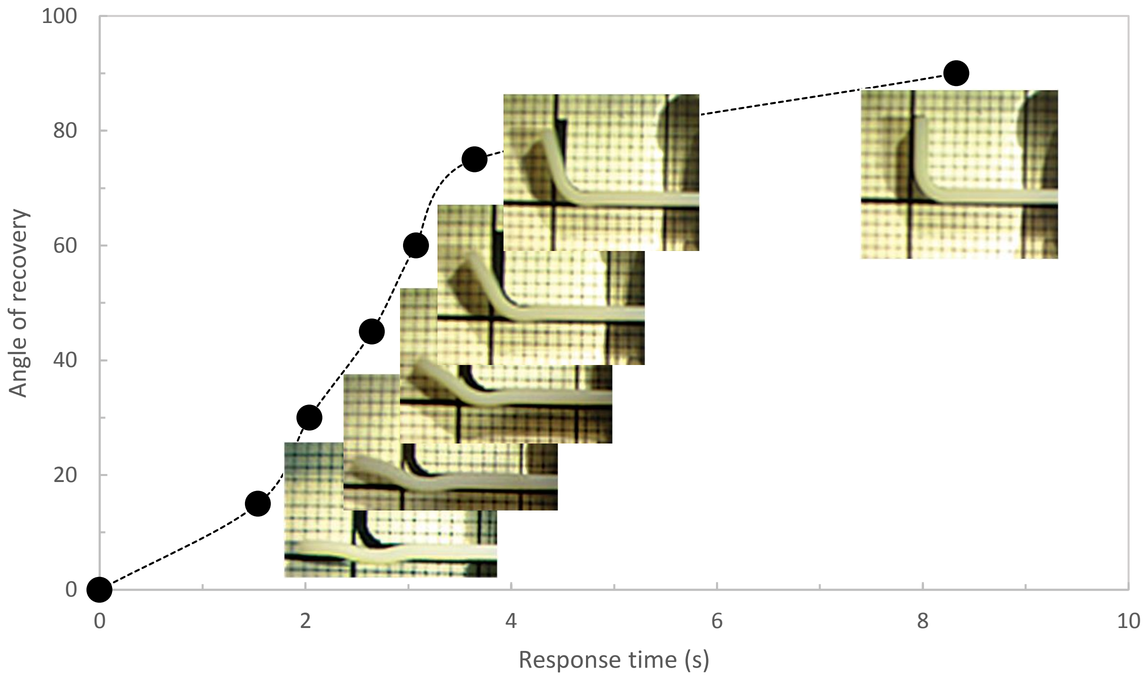

Figure 32. Angle of recovery as a function of time during heating in water bath at temperature of 75°C for VerowhitePlus

The experimentally determined response times and corresponding simulation results as a function of thickness for four different materials are shown in Figure 33. The results show clearly that thickness is a critical factor in controlling material response time. For each material, the response time increases with increasing thickness consistently. This relationship can be attributed to thermal mass of the hinge structure. The thicker the hinge, the greater the mass and the larger amount of thermal energy needed. Moreover, along the mass, there is an increase in volume and surface area for convective heat transfer from system to surroundings. Hence, given the same material and the same heat transfer rate, longer time is needed to reach T_g temperature, i.e. longer time is needed to fully reach shape recovery temperature when the structure is immersed in hot water.

Figure 33 also shows that the percentage of TB in the materials affects the response time. DM8530 contains the highest percentage of TB and responds the fastest among all the materials. On the contrary, VW contains zero TB and shows the longest response time. This relationship agrees with the T_g temperatures of four materials in which VW has the highest T_g, and DM8530 the lowest T_g. Given the same heat transfer rate as discussed previously in Table 3, a material with higher T_g takes longer time to be activated. Furthermore, there was a good agreement between simulation results and experimental results in terms of shape recovery time. However, when hinge thickness increases from 0.3 mm to 2.0 mm, differences between simulation and experimental values tend to increase, with 2 mm hinge showing the largest discrepancies regardless of materials. In addition to heat transfer, another reason is that the recovery of 2 mm hinge is the slowest among all specimens and the end point of recovery can hardly be precisely determined from video method, hence showing a greater tendency for reading errors. Nevertheless, the overall discrepancies range from about 5% to 16%. The overall discrepancies refer to the differences between experimental data and simulation data. At each thickness and each material, the smallest difference between experiment and simulation is 5% and the largest is 16%. The causes of such discrepancies could be due to the differences in heat transfer environment in simulation and reality (e.g. micro air bubbles on surfaces, etc.) as well as effects resulting from interpolated densities and thermal conductivities.

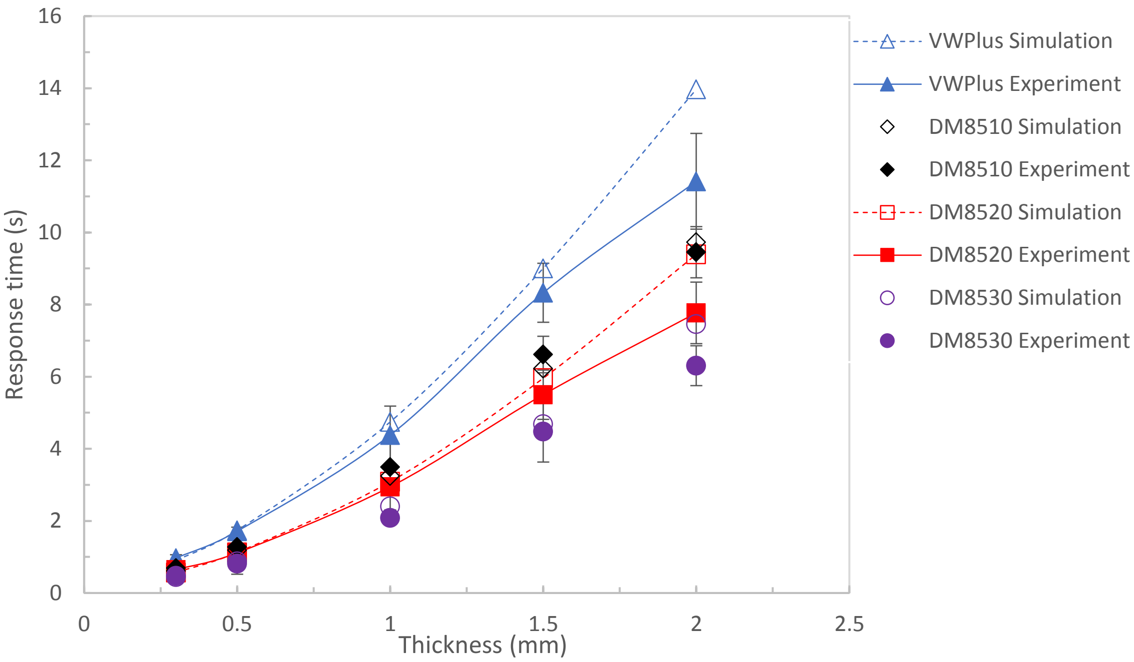

Figure 33. Simulation results and experimental data of response time versus material thickness for four tested materials indicated

4.3.2.2 Spiral square

After printing, the spiral square was programmed into a straight strip and then placed in a hot water bath for shape recovery. Hot water temperature was closely monitored by thermometer readings (constant at 81°C). The outermost end of the spiral square was fixed as the recovery pivot. The specimen recovered back to its original shape by a multistage sequential movement, starting from the thinnest hinge of 0.5 mm to the thickest hinge of 2 mm (Figure 34, supplementary video is available). Based on the video method, the full recovery time was determined to be 7.187 seconds, close to the simulation result of 6.034 seconds. The difference could be due to several reasons: (1) the surface of the sample was in contact with the bottom of the water bath which reduced heat transfer from hot water; (2) the interface between the sample surface and the hot water might not be as ideal as what has been assumed in the simulation (for example, there might exist gas bubbles at the interface between sample and water, hence reduced the heat transfer), which might also be responsible for the discrepancies between the simulation and experimental data. It is worth noting that the response times of L-hinge (2 mm) and spiral square (2 mm hinges) were slightly different, 11.419 seconds and 7.187 seconds, respectively. This is because in spiral square experiment, the water bath temperature was 81°C, higher than 75 °C in L-hinge experiments, which gave spiral square faster response.

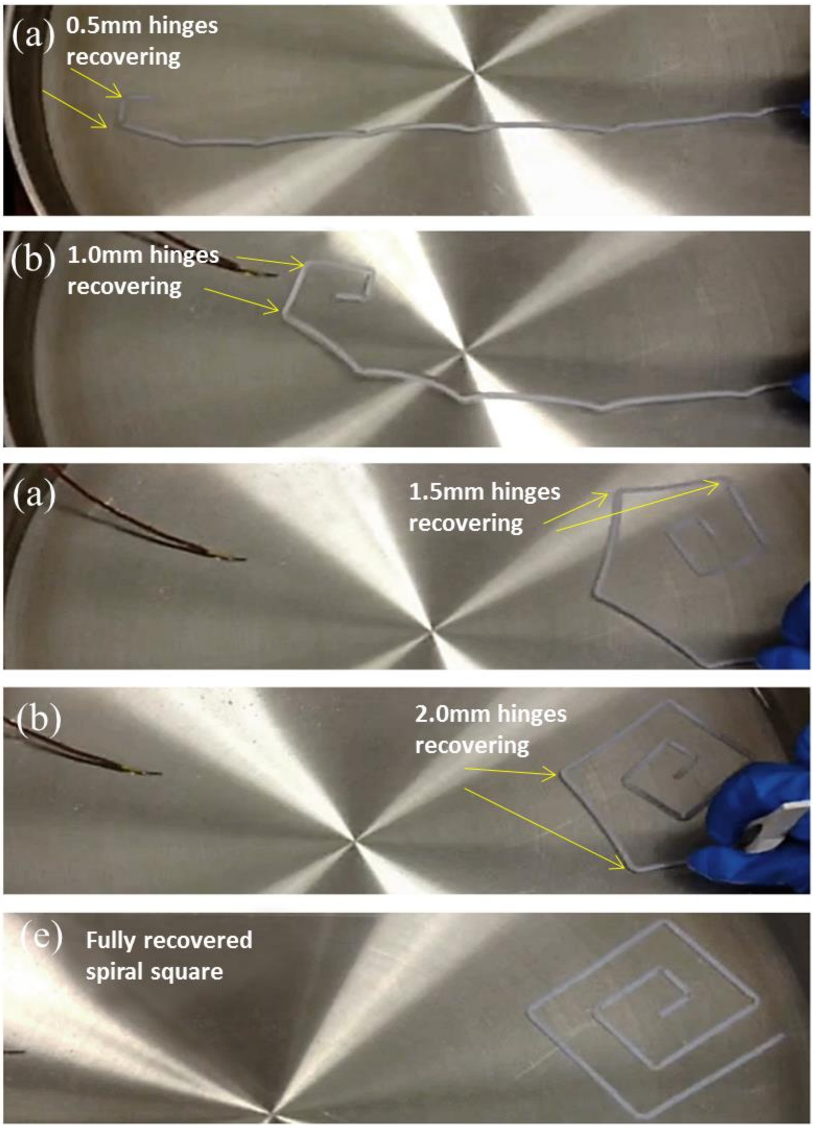

Figure 34. Screens shots of multistage sequential recovery of a spiral square

Video: Multistage sequential recovery of a spiral square

4.3.2.3 Orchid flower

For a natural orchid flower, during its blossom period, the bottom layer of the flower opens first, followed by the middle layer and then the top layer. These sequential events can be mimicked by an artificial flower 3D printed using a single material with different petal thicknesses. Given the inverse relationship between thickness and recovery time, the top layer was designed to be the thickest (1.7 mm) and the bottom layer the thinnest (0.5 mm). Figure 35 illustrates the recovery process of a printed flower made from a single SMP (VM added for pink colour). After printing, the flower was programmed into a bud. When the bud was placed in a hot water bath, the bottom layer recovered first, followed by the middle layer and then the top layer (Supplementary video is available). The whole recovery process resembles the natural blooming phase of an orchid flower. The combination of a single printable material and printed thickness control provides a highly flexible design and fabrication methodology. Such multistage recovery process has been accomplished by printing multiple materials of different T_g temperatures in the structure [94]. This, however, requires the use of complex multi-material printer such as Objet Connex 500.

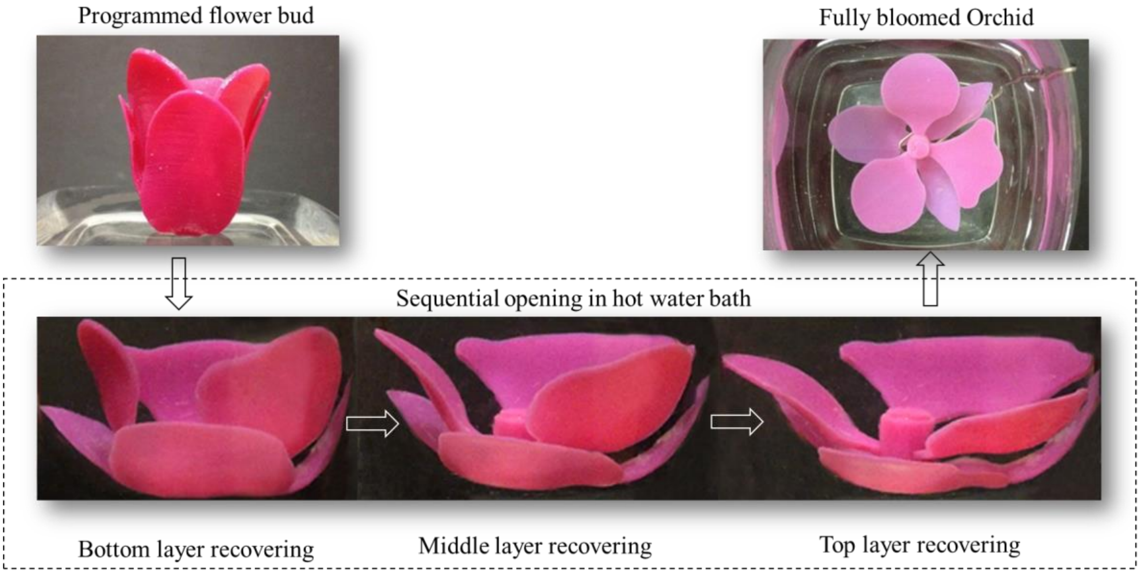

Figure 35. Multistage sequential opening of Orchid flower printed with single material

Video: Single material, multistage sequential opening of Orchid flower

In this research, instead of using multiple materials of different T_g temperatures a geometric parameter such as thickness is used to achieve controlled multistage shape morphing with a single material. The results demonstrated that thickness can be used as one more dimension for 4D printing design, further increasing the response complexity of the smart structures. In this sense, single material-based multistage sequential morphing could become an important factor or consideration in future 4D printing research.

There are a few advantages when using a single material with thickness variation. Firstly, it increases the complexity of 4D printing designs by changing material thickness with no new materials required. Secondly, geometric thickness is simple and easy to be used as a control factor when designing continuous gradient features involving uniform material as compared to using multiple materials. Typically, it allows a smooth transition from the thinnest to the thickest in a single material, while multiple materials with different T_g will always give a discrete allocation of different materials, in which non-smooth transition from one material to another is unavoidable. Thirdly, this new approach increases the applicability of 4D printing, especially in an environment which does not permit the use of multiple materials due to limitation in a fixed range of T_g. Currently, most 4D printing research, especially controlled shape morphing or actuation, rely on 3D printing of multiple materials. Multi-materials must be used in an environment where the temperature is higher than all the glass transition temperatures of the printed materials. However, in certain applications where the environment temperature is limited to certain level at which materials with high T_g cannot be used, in this case manipulating the thickness of a single material for multistage response purpose approach will clearly have an advantage. Finally, there are a few other 4D printing research works involving the use of single material (e.g. FDM, SLA, DLP or SLM), however there is little control during the shape shifting or multistage morphing. This research has presented a single material approach with controlled multistage response by choosing material thickness as a controlling factor, which breaks the barrier of PolyJet and could enable more single material 3D printers for controlled multistage 4D printing, thus increasing the level of complexity while avoiding the high cost of using multi-materials.

Nevertheless, there are a couple of limitations in this research. The thinnest printable and programmable thickness was tested only on Objet500 Connex3 PolyJet printer (Stratasys, USA) machine, which was 0.01mm. This approach is also not applicable for structures which require uniform thickness throughout the part geometry. Moreover, fatigue behaviour of 3D printed shape memory polymer is an important topic. In this research we did conduct a minimum of 3 cycles for each thickness with varied materials, and thick L-hinges demonstrated with no functional degradation, while repeated uses of smaller thickness caused fracture. A separate systematic investigation is necessary if the intended application requires repeated usage of the printed smart structures.

The printed geometric thickness has been determined to be a key design parameter that can be used to effectively predict the shape recovery response time in 3D printed L-hinge and spiral structures using a single shape memory materials. In future, in addition to thickness other geometric parameters such as diameter and height could be explored in a similar way for design consideration of 4D printing.

4.4 Summary

In the present chapter, the effect of thickness on the response time of 3D printed shape memory polymers has been investigated in both 2D and 3D smart structures (i.e. L-hinges, spiral square and orchid flower). It has been demonstrated that through controlling the thickness of each component in the smart structure alone, the response sequence can be precisely controlled. This is because material thickness affects heat transfer, differentiating material full recovery time or the response time to heat. This approach provides an alternative to the use of multiple materials which are expensive and may not be applicable to smart structures which require the use of single material. Moreover, this approach allows 4D printed structures to respond sequentially at a temperature in-between the Tg temperatures of multiple materials, which is currently impossible to achieve in multi-material approach. Furthermore, our approach is design based rather than multi-material based, hence providing an additional degree of freedom for designing complex responses of 4D printed smart structures, especially when employed in combination with multi-material based approach.

CHAPTER FIVE - DESIGN OF CROSSFOLDING-BASED SMART STRUCTURES

5.1 Introduction

Folding and unfolding of structures are essential in 4D printing. Usually, structures fold or unfold along certain axis. A folding line is defined as a segment of the folding axis on the structure. In a simple structure such as a hinge, there is only one folding line. In a structure involving multifolding, there are multiple folding lines. However, these folding lines may or may not overlap or cross each other (see Figure 36). Crossfolding is defined as a multifolding in which at least two folding lines within the same plane overlap each other (Figure 36(b)). In previous two chapters, multimaterials and design geometry have been demonstrated to increase the complexity of 3D printed smart structures. However, they are applied to structures with non-overlapping folding lines only. Whether the design guidelines are applicable to structures with overlapping folding lines is unknown. Moreover, crossfolding allows the deformation of a structure to be doubled i.e. saving 50% of the space in a single fold. Therefore, in this chapter, 4 different materials (VeroWhitePlus, DM8510, DM8520 and DM8530) and 3 different axes (x, y and z) are selected to explore the feasibility of printing and programming crossfolded smart structures as well as to characterize crossfolded structures. Mechanical properties of single material and multimaterials will be analysed first and then crossfolded single material structures and multimaterial structures are designed and demonstrated.

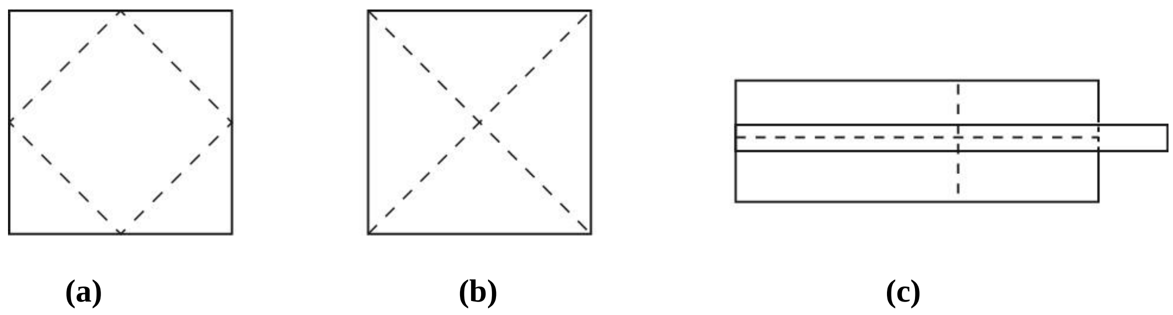

Figure 36.Multifolding. (a) Non-overlapping folding lines. (b) Overlapping folding lines, and (c) Combination of overlapping and non-overlapping folding lines

5.2 Materials and methods

5.2.1 Preparation of single material specimens and tensile test

All specimens used in this Microforce test are prepared by PolyJet 3D printing machine. The four materials used are VeroWhitePlus, DM 8510, DM 8520 and DM 8530. Five specimens were 3D printed for each type of the material. Among four materials, DM 8510, DM 8520 and DM 8530 are digital materials that are combinations of two materials. They all have VeroWhitePlus as primary material and TangoBlackPlus as secondary material. The difference is that the percentage of TangoBlackPlus material increases from DM 8510 to DM 8530 (refer to Appendix B and Appendix C).

According to ASTM D638 standard, for rigid and semi-rigid plastics, type I and type II specimen shall be used when material having a thickness of 7mm [99]. Type III specimen must be used for material having a thickness greater than 7mm, while type IV specimen shall be used when need to compare materials in different rigid cases [99]. Type V specimen shall be used for material having a thickness of 4mm or less [99]. Thus, for the specimen used in this tensile test, ASTM D638 type V is chosen and shown in Figure 37.

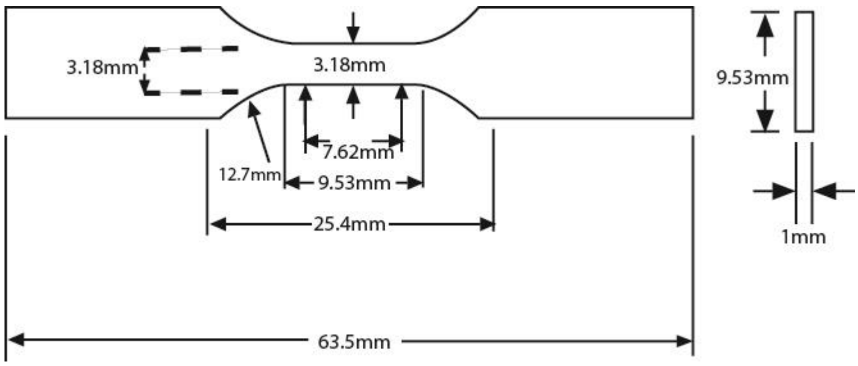

Figure 37. Type V: specimen dimensions

MTS Criterion Model 43 machine from MTS Systems Corporation in the United States, it is used for this microforce test. The fixed and the movable member of the machine carries grip. The specimen shall be clamped with alignment and held without any slippage to the grips. The load is measured using a load cell and the displacement of the crosshead is set to be 3.5mm. The heating chamber of the machine is used to heat up the specimen to 70°C and maintain the temperature.

A thermocouple is used to monitor the surface temperature of the specimen while 10 minutes are waited upon to ensure complete heat transfer across the specimen.

A temperature-controlling water tank is used for reheating the specimen after measuring the elongation.

5.2.2 Calculation of shape recovery for single material specimens

To determine the shape recovery characteristics for single material specimens, the shape setting test method steps using the microforce test specimen are show in Figure 38. For every specimen of four different materials, the specimen was held using tensile grips at room temperature of 25°C. The displacement of the crosshead was set to 3.5mm and the load calibration was applied. The chamber was heated to an equilibrium temperature of 70°C and tensile testing was performed. After the tensile test was completed, the chamber temperature was reduced to 25°C with the specimen still held by tensile grips and change in length was measured. The specimen was placed in a hot water batch of 70℃ for shape recovery and change in length was measure again.

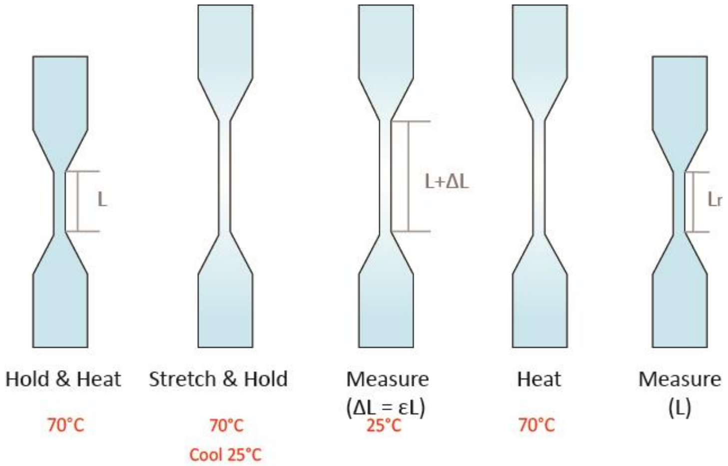

Figure 38. Shape recovery properties measurements

After the final gauge length L_f was measured, the percent elongation was calculated using the formula:

$$\%El = [(L_f - L_o)/L_0]x100\% \qquad \text{Eqn. (3)}$$

Similarly, the gauge length L_r after recovery by reheating was measured and the percent recovery was calculated using the formula:

$$\%R = [1-(L_r-L_o)/L_o]x100\% \qquad \text{Eqn. (4)}$$

The original gauge length L_o = 7.62mm.

$$\text{Percentage of recovery rate} = [1- (L_r-L)/\Delta L] \qquad \text{Eqn.(5)}$$

5.2.3 Design and crossfolding of single material smart structures

Based on the tensile test results, DM8530 material has near 100% recovery. Therefore it was selected to study the influence of hinge thickness in multifolding process. A series of tests were conducted using DM8530 material. There are 12 sets of specimens of Length x Width x Thickness = (60 x 15 x 1.5) mm. Each specimen was designed with two crossed folding lines as shown in Figure 39. For folding line 1, the thickness (note: not the width of the channel) was

0.1mm, 0.3mm and 0.5mm and for folding line 2, the thickness was a constant of 1.0 mm. Also, a hole was designed at the cross to study the folding effect with and without stress concentration.

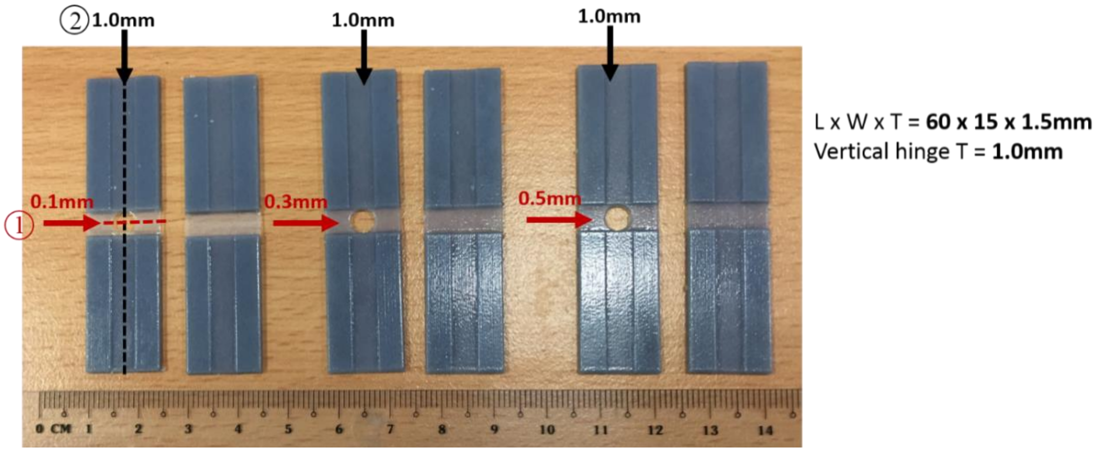

Figure 39.Structures with crossed folding lines of different thicknesses

5.2.4 Preparation of multimaterial specimens for tensile test

According to ASTM D638 standard, specimen dimension is given below in Figure 40.

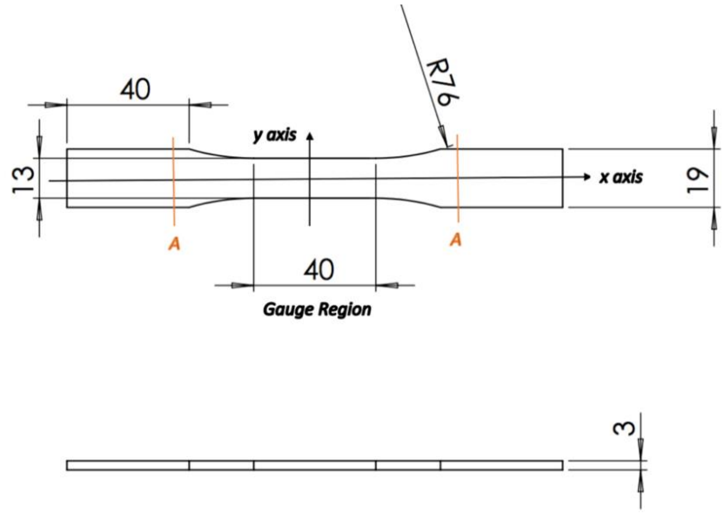

Figure 40. Specimen dimensions

In each combination, two materials were combined symmetrically along X-axis, Y-axis and Z-axis (here Z-axis refers to XY plane) in Table 7.

Table 7. Specimen material composition

X-axis	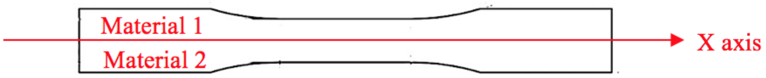 
Y-axis	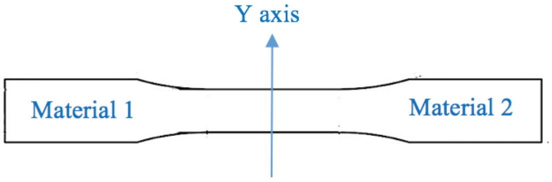 
Z-axis (XY plane)	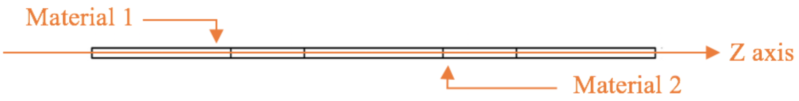 

ASTM D638 standard tensile tests were performed on all specimen at room temperature of 25°C.

The testing stroke speed is given 3mm/min to comply with ASTM D638, which gives a strain rate of

$$\dot{\varepsilon}(t) = \frac{d\varepsilon}{dt} = \frac{d}{dt}\left(\frac{L(t) - L_0}{L_0}\right) = \frac{1}{L_0}\frac{dL}{dt}(t) = \frac{v(t)}{L_0} = \frac{3mm/min}{40mm} \qquad \text{Eqn.(6)}$$

$$= 1.25 \times 10^{-3} mm/s$$

$v(t)$: the speed at which the ends of specimen are moving away from each other, i.e. stroke speed

L_0: original specimen gauge length

For each specimen clamp sample at two ends exposing the gauge length, set testing speed at 3mm/min, zero force and stroke displacement and when fracture occurs, stop testing and export testing data.

5.2.5 Rule of mixtures for multimaterial specimens

Rule of Mixtures is a math expression which describes some properties of the composite in terms of the properties, quantity and arrangement of their constituents [100]. It can be used to predict the overall Young's Modulus of the mixture in terms of the moduli of the individual constituent phases and their volume fractions [101]. The properties, i.e. Young's Modulus, are proportional to their volume fractions of the components and lie between the pure component values [102]. In this project, different multi-material conditions can be approximated as rule of mixture composite to obtain predicted Young's Modulus. Two established methods have been practised to calculate mixture's Young's Modulus under the concept of rule of mixtures, namely iso-strain and iso-stress. Two simple models widely used are Voigts' iso-strain model and Reuss' iso-stress model (Figure 41) [103].

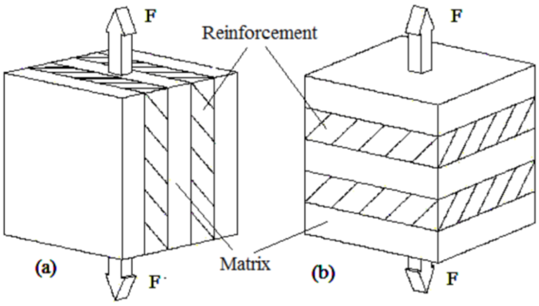

Figure 41. a)Voigts' iso-strain model b)Reuss' iso-stress model

As the name implies, iso-strain requires the composite components to undergo the same strain deformation, which normally refers to longitudinal loading whereby load direction is the same as fibre direction [104]. In our case, the whole specimen is the composite. Material 1 can be approximately treated as matrix while material 2 can be approximately treated as fibre. Iso-strain can be applied to multi-material printing orientation of X-axis and Z-axis (XY plane) as illustrated below in Figure 42 and Figure 43. Both materials undergo the same deformation, ε.

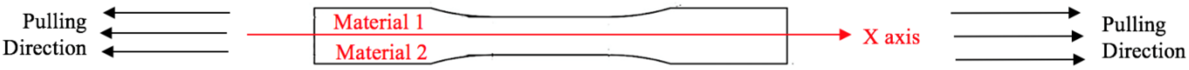

Figure 42. Modelling X-axis combination as iso-strain

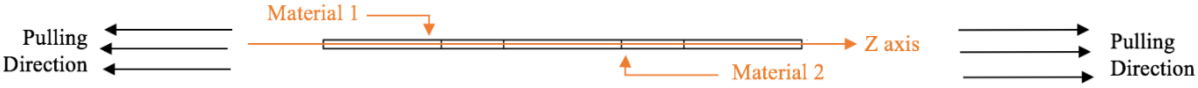

Figure 43. Modelling Z-axis (XY plane) combination as iso-strain

For iso-strain condition, Young's Modulus of the composite can be calculated by Eqn.(7)[105]:

$$E_c = E_m V_m + E_p V_p \qquad \text{Eqn.(7)}$$

In our case, the equation is modified to the following equation Eqn.(8):

$$E_s = E_{m1} V_{m1} + E_{m2} V_{m2} \qquad \text{Eqn.(8)}$$

Young's Modulus for material 1 and 2 are known separately from previous tests. Volume fractions are 50% for matrix (material 1) and fibre (material 2). Since $V_{m1} = V_{m2}$ =50%, the equation is rewritten in the following form:

$$E_s = V_m(E_{m1} + E_{m2}) \qquad \text{Eqn.(9)}$$

Hence, the choice of material 1 or material 2 as matrix or fibre will not affect the result. Young's Modulus for the specimen can then be calculated.

On the other hand, iso-stress refers to condition whereby load is applied normal to the plane of fibres [104]. Normal stresses for matrix and fibres are the same. This condition can be applied to multi-material printing orientation of Y-axis as illustrated in Figure 44. Since both materials have the same cross-section, upon application of load, they will have the same normal stress according to Eqn. (10):

$$\sigma = \frac{F}{A} \qquad \text{Eqn.(10)}$$

where F is the force applied and A is the cross-sectional area [106].

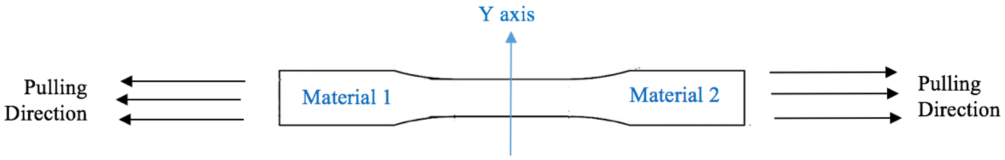

Figure 44. Modelling Y-axis as iso-stress

For iso-stress condition, Young's Modulus of the composite can be calculated by Eqn. (11) [105]:

$$E_c = \frac{E_m V_f + E_f V_m}{E_m E_f} \qquad \text{Eqn.(11)}$$

In our case, the equation is modified to the following equation Eqn. (12):

$$E_c = \frac{E_{m1} V_{m2} + E_{m2} V_{m1}}{E_{m1} E_{m2}} \qquad \text{Eqn.(12)}$$

Similarly, Young's Modulus for material 1 and 2 are known separately from previous tests and volume fractions are both 50%:

$$E_c = \frac{E_{m1} + E_{m2}}{E_{m1} E_{m2}} V_m \qquad \text{Eqn.(13)}$$

Hence again, it does not matter to treat material 1 or material 2 as matrix or fibre.

5.2.6 Design and crossfolding of multimaterial smart structures

There are two types of folding: folding at not more than 90° and folding at more than 90°. Crossfolding requires the first folding angle to be close to 180° before the second fold. Given a rectangular shape, there are two ways to cross fold: (1) fold on short edge on folding line 1 and then the long edge on folding line 2 (Figure 45); Figure 46 shows the crossfolded structure using method 1. (2) fold on long edge first and then short edge (Figure 47). Both methods were tested with a variation of thickness: 0.1, 0.3, 0.5, 1, 1.5, 2 (mm). 0.1 mm is the thinnest possible for manual handling after PolyJet printing.

For this structure it was created by the first fold along folding line 1, followed by the folding along folding line 2 to create a crossfolding and the bottom hinge folded outwards. Materials with the different T_g were chosen and placed according to its movement.

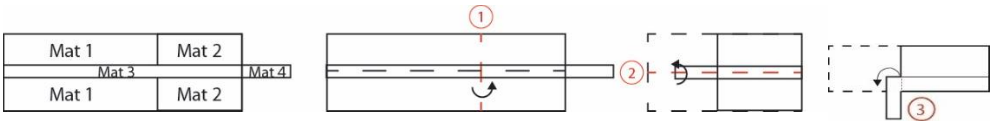

Figure 45. Sequence of crossfolding for method 1

Figure 46. Crossfolding of final structure of method 1

Method 2 was created by folding along fold line 2 across the structure and followed by folding along fold line 1 in another direction and the bottom hinge folded inwards which is opposite from Method 1. Figure 48 shows the crossfolded structure using method 2.

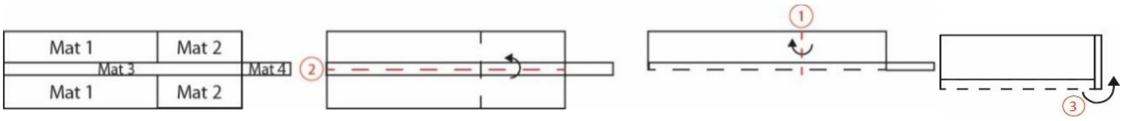

Figure 47. Sequence of crossfolding for method 2

Figure 48. Crossfolding of final structure of method 2

5.3 Results and discussion

5.3.1 Shape recovery of single material specimens

The recovery rates (in percentage) of four different materials are shown in Figure 49. DM8530 achieved the highest recovery rate whilst VeroWhitePlus has the lowest recovery rate. Due to the better recovery property, DM8530 should have a stronger ability to take multi-folding process.

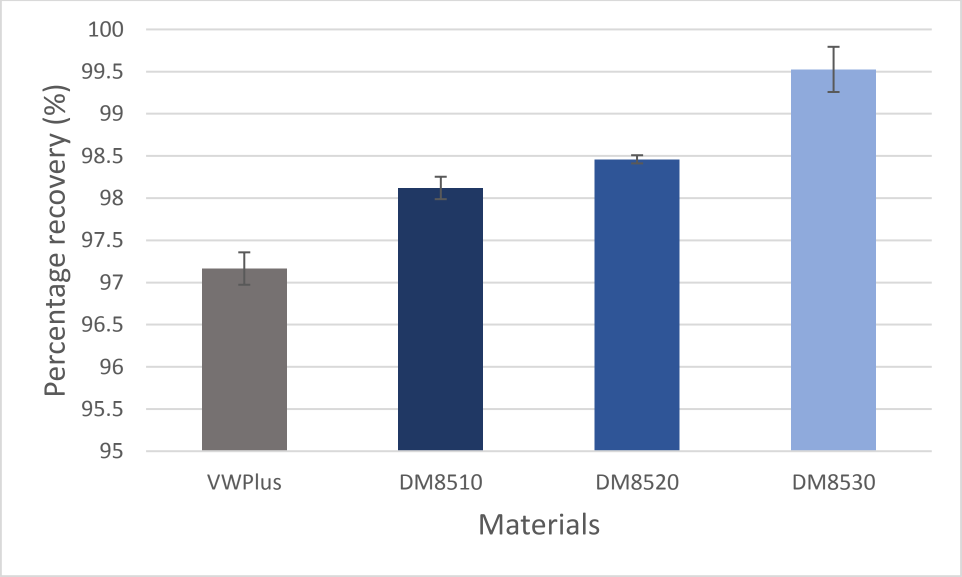

Figure 49. Percent recovery comparison of four materials

5.3.2 Recovery of crossfolded single material smart structures

(a) Thickness of folding line 1 = 0.5 mm, folding line 2 = 1 mm

As shown in Figure 50 and Figure 51, the sequence of the unfolding showed that 0.5 mm (folding line 1) opened earlier than 1.0 mm (folding line 2) due to rapid response to thermal stimulus. The folding line 1 of 0.5 mm unfolded first in both cases, no matter how the folding sequence was. This result was expected, as explained in Chapter 4, heat transfer was faster when the material was thinner, hence an earlier response. This result suggested that given the same unfolding sequence of folding line 1 and folding line 2, there were at least two ways to fold the structure into a compact form. In other words, crossfolding can increase the variety of smart structures.

(1) **(2)** **(3)** **(4)** **(5)**

Figure 50. Method 1- The sequence of unfolding from (1) to (5)

(1) **(2)** **(3)** **(4)** **(5)**

Figure 51.Method 2- The sequence of unfolding from (1) to (5)

Figure 52 shows that folding was easier when there was a hole in the centre the specimen, since the specimen with a hole has less stress concentration than the specimen without a hole.

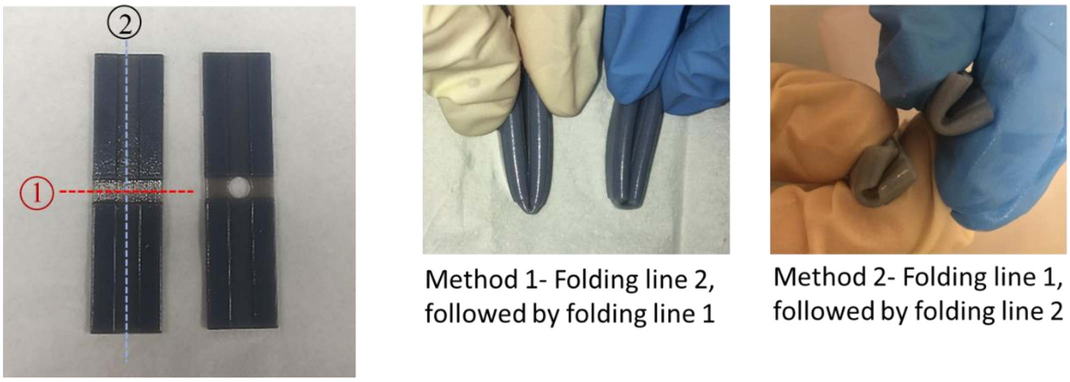

Method 1- Folding line 2, followed by folding line 1

Method 2- Folding line 1, followed by folding line 2

Figure 52. Crossfolding for 0.5 mm sample

As shown in Figure 53, a repeated test was performed for the same specimen and it started to break at the fourth time of programming. It was observed that a hole in the centre reduced the stress concentration and cracks.

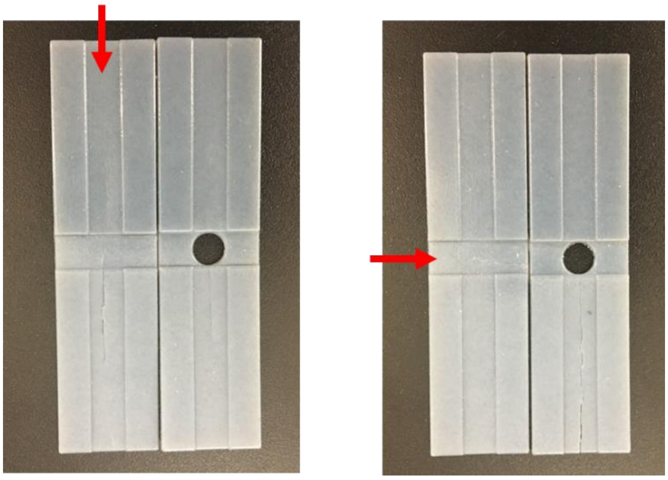

Figure 53. Fracture for 0.5 mm sample

(b) Thickness of folding line 1 = 0.3 mm, folding line 2 = 1 mm

In Figure 54 and Figure 55, similar behaviours were observed except that in the repeated test, the specimen started to break at the second time of programming.

(1) **(2)** **(3)** **(4)** **(5)**

Figure 54.Method 1- The sequence of unfolding from (1) to (5)

(1) **(2)** **(3)** **(4)** **(5)**

Figure 55.Method 2- The sequence of unfolding from (1) to (5)

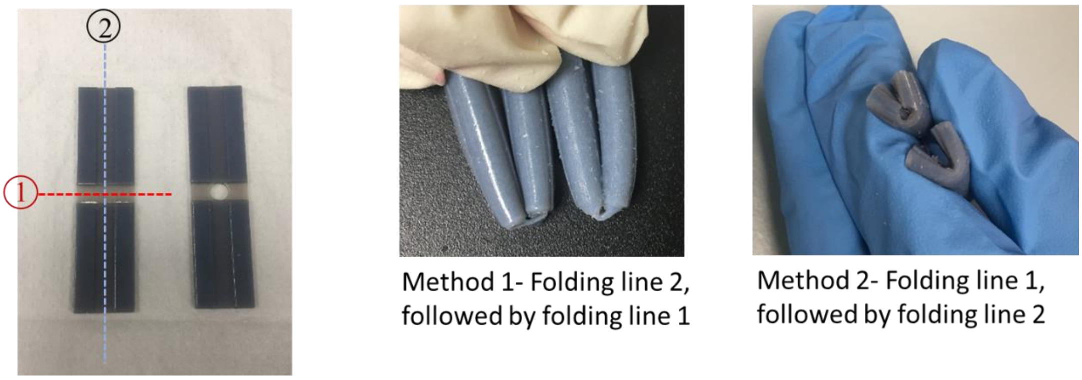

Method 1- Folding line 2, followed by folding line 1

Method 2- Folding line 1, followed by folding line 2

Figure 56. Crossfolding for 0.3 mm sample

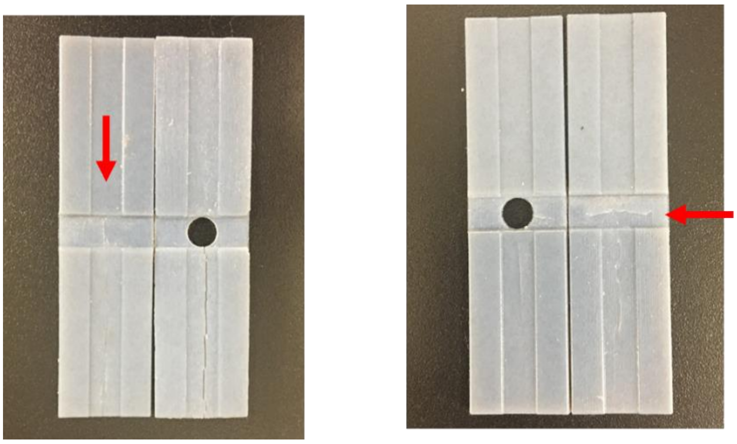

Figure 57. Fracture for 0.3 mm sample

(c) Thickness of folding line 1 = 0.1 mm, folding line 2 = 1mm

Similar behaviours were observed as shown in method 1 and 2 in Figure 58, except that the specimen was unable to recover and in the repeated test the specimen started to break at the first time of programming shown in Figure 60.

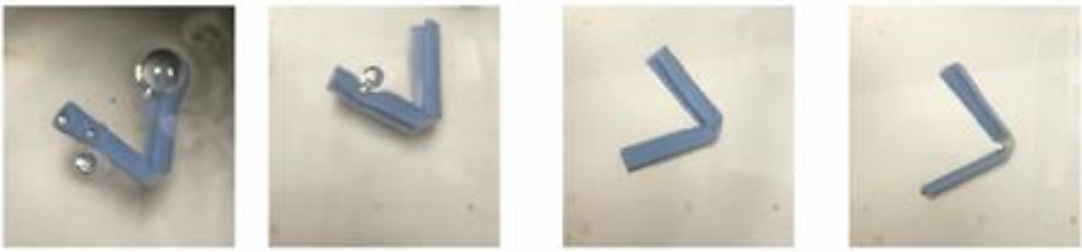

(1) (2) (3) (4)

Figure 58.Method 2- The sequence of unfolding from (1) to (4)

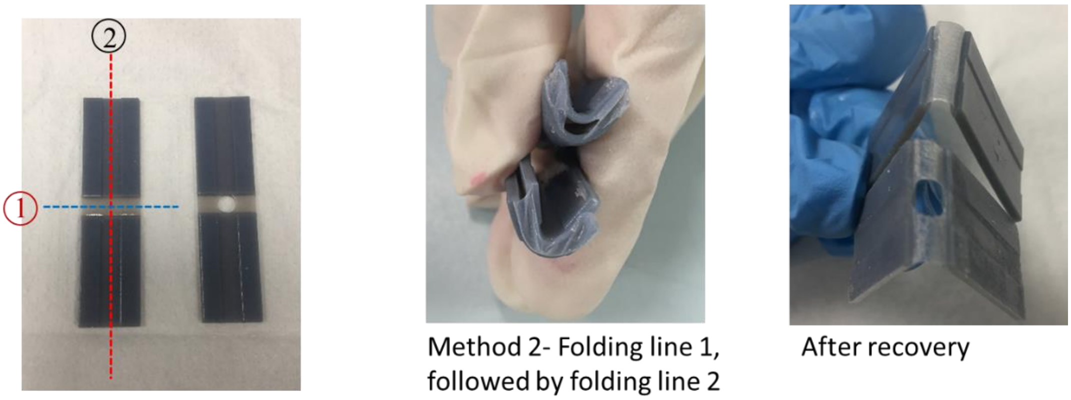

Method 2- Folding line 1, followed by folding line 2

After recovery

Figure 59. Crossfolding for 0.1 mm sample

Figure 60.Fracture for 0.1 mm sample

The results of single material crossfolding can be summarized in Table 8

Table 8. Single material crossfolding

Horizontal hinge thickness		Folding sequence	Open sequence	Maximum folding times	Crack With visual inspection
0.5mm	With hole	2+1	1+2	3	Less
		1+2			
	Without hole	2+1			More
		1+2			
0.3mm	With hole	2+1	1+2	1	Less
		1+2			
	Without hole	2+1			More
		1+2			
0.1mm	With hole	2+1	NA	NA	Break
		1+2	1+2		Less
	Without hole	2+1	NA		Break
		1+2	1+2		More

1 = Folding line 1
2 = Folding line 2

Maximum folding times
(Number of times cross-folded)

5.3.3 Analysis of tensile test results for multimaterial specimens

Crossfolding of multimaterial structure is different from crossfolding of single material structure, because material interfacial bonding in multimaterial structure may play a role in shape setting. There is a concern that fractures or delamination may occur at the interface of different materials during shape setting. Therefore analysis of mechanical properties of multimaterial specimens is necessary.

(a) Stress strain curves

At room temperature of 25℃, stress-strain curves for material combination of VeroWhitePlus and D8510 are shown in Figure 61 - Figure 63 for X, Y and Z axis. Other stress-strain curves and results are attached in Appendix A. For a combination of VeroWhitePlus and D8510, Figure 61 shows the stress-strain curves.

When two materials were combined symmetrically along X-axis, the stress-strain curve was obtained as shown in Figure 61.

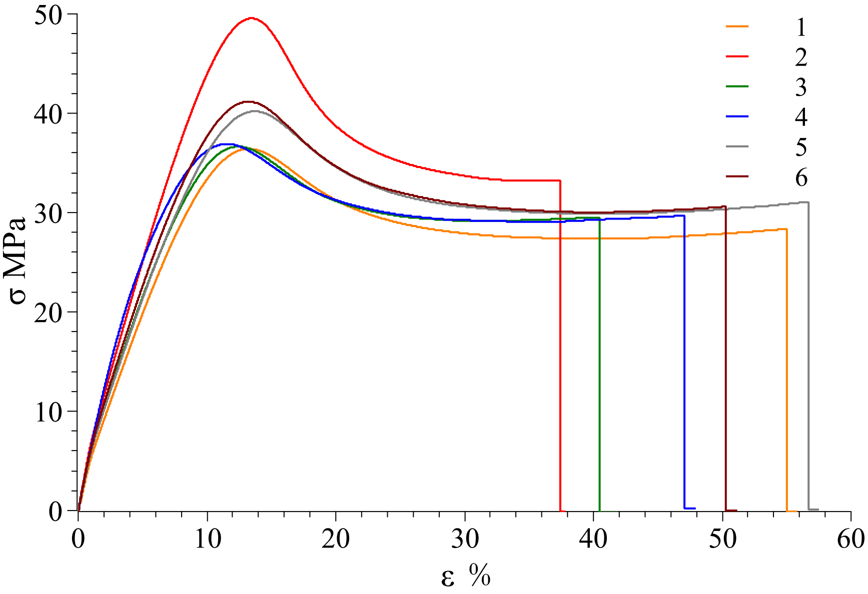

Figure 61. VeroWhitePlus, DM8510 stress-strain curve for X-axis

When two materials were combined symmetrically along Y-axis, the stress-strain curve was obtained as shown in Figure 62.

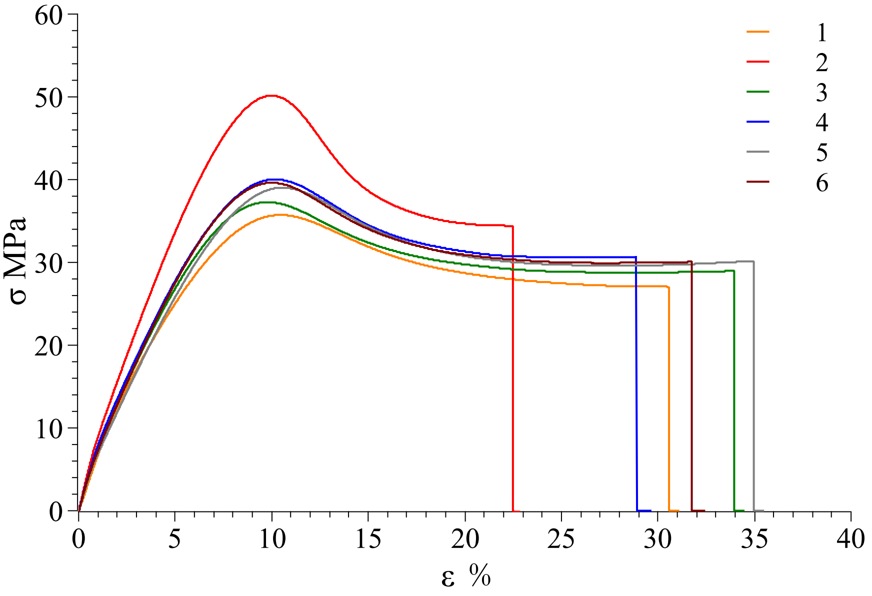

Figure 62. VeroWhitePlus, DM8510 stress- strain curve for Y-axis

When two materials were combined symmetrically along Z-axis (XY plane), the stress-strain curve was obtained as shown in Figure 63.

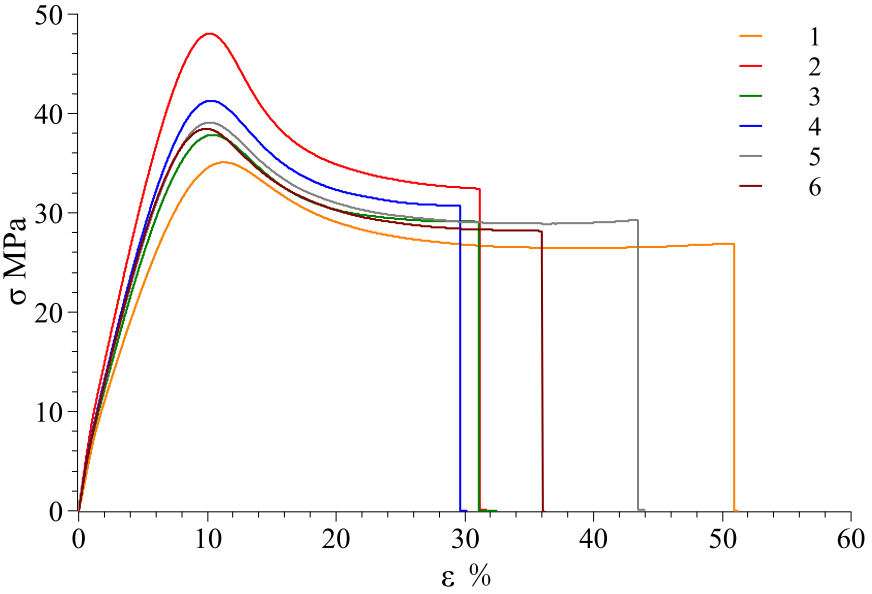

Figure 63. VeroWhitePlus, DM8510 stress-strain curve for Z-axis (XY plane)

As observed, red curve (#2) was likely an outlier as the curve deviated from the rest too much. After removing it, the following Table 9 shows the averages obtained from the remaining 5 curves.

Table 9. VeroWhitePlus, DM8510 combination thermal-mechanical properties

Axis	X	Standard deviation	Y	Standard deviation	Z	Standard deviation
Ultimate Tensile Stress (MPa)	38.273	±2.238	38.335	±1.793	38.354	±2.246
Maximum Strain (%)	50.795	±6.272	46.465	±3.403	55.247	±12.348
Young's Modulus (MPa)	628.281	±38.849	557.266	±48.595	552.231	±63.868

(b) Theoretical versus experiment

After calculation based on rule of mixture, the following results were obtained as shown in Table 10. For Young's Modulus, all experimental values were lower than predicted values. One possible reason is imperfect interfacial bonding that weakens the bond as discussed under single material investigation. Moreover, rule of mixtures applies to composites with long and continuous fibres embedded. Our multi-material conditions are just approximation of rule of mixtures situations as our fibre (material 1 or material 2) is not embedded in the composite. Materials are printed side by side, which results in less restraining force applied on the matrix from fibres, hence making the specimen easier to deform (smaller Young's Modulus). Additionally, the material in the experiments was not long enough to be classified as long fibres. The general aspect ratio (length to diameter) of long fibre should be at least 200 [107]. Moreover, Young's Modulus of X-axis is greater than Z-axis (XY plane). According to rule of mixtures, X-axis and Z-axis (XY plane) should give the same Young's Modulus. The reason could be that Z has a larger contact surface between two different materials. When it is not 100% bonded, it allowed more slippery movement and made the specimen more elastic (smaller Young's Modulus).

Table 10. Young's Modulus comparison for multi-material combination

E_{VW} (MPa)	E_{D8510} (MPa)	V_{VW}	V_{D8510}	Material combination axis	$\boldsymbol{E_{Predicted}}$ (MPa)	$\boldsymbol{E_{Experimental}}$ (MPa)	Error
818.479	742.110	0.5		X	780.295	628.281±38.849	19.5%
				Y	778.426	557.266±48.595	28.4%
				Z	780.295	552.231±63.868	29.2%
E_{D8510} (MPa)	E_{D8520} (MPa)	V_{D8510}	V_{D8520}	Material combination axis	$\boldsymbol{E_{Predicted}}$ (MPa)	$\boldsymbol{E_{Experimental}}$ (MPa)	Error
742.110	693.520	0.5		X	717.815	582.590±48.531	18.8%
				Y	716.993	499.329±69.315	30.4%
				Z	717.815	497.307±53.639	30.7%
E_{D8520} (MPa)	E_{D8530} (MPa)	V_{D8520}	V_{D8530}	Material combination axis	$\boldsymbol{E_{Predicted}}$ (MPa)	$\boldsymbol{E_{Experimental}}$ (MPa)	Error
693.520	546.235	0.5		X	619.878	496.813±34.982	19.9%
				Y	611.129	417.935±60.800	31.6%
				Z	619.878	413.767±63.502	33.3%

(c) Rupture location and interfacial bonding strength

For Y-axis, the following ruptures were obtained (Figure 64). Young’s Modulus and Ultimate Tensile Stress decrease in the order: VeroWhitePlus>D8510>D8520>D8530. All three specimens did not break at the interface of stronger and weaker materials but always at the weaker material. Since all specimens broke at the weaker material, not at the bonding, it meant that the interfacial bonding transmitted stress over to the weaker material. This observation is in correspondence of the test results from Ge, Sakhaei, Lee and et al’s findings [108]. This result showed that the possibility of delamination or fracture at the interface of different materials during shape setting was negligible.

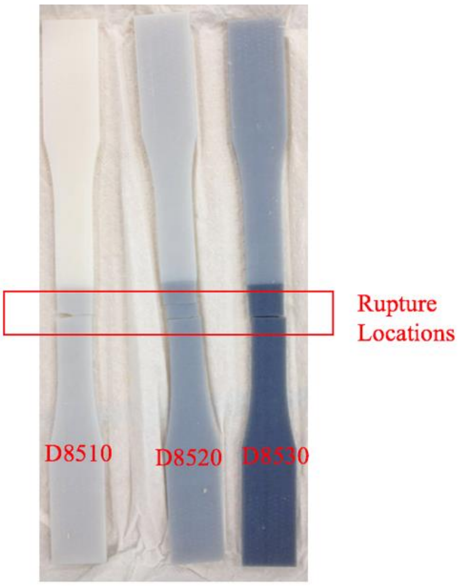

Figure 64. Rupture locations for Y-axis

(d) Effect of material combination axis

Material combination axis is the axis along which two materials are symmetrically combined. It is noted that material combination axis can have a significant effect on maximum strain and Young's modulus of all material combinations, but a mixed effect on UTS. As shown in Figure 65, the material combinations did not suggest a consistent no effect on UTS. The combination of D8520 and D8530 has a lower UTS value when combined along Y-axis. The reason was unknown. It might be related to the increased rubbery content in the materials, since the combination of D8510 and D8520 also showed a slightly lower UTS value for Y-axis. The rubbery content in each material increased in the following order: VeroWhitePlus < D8510 < D8520 < D8530.

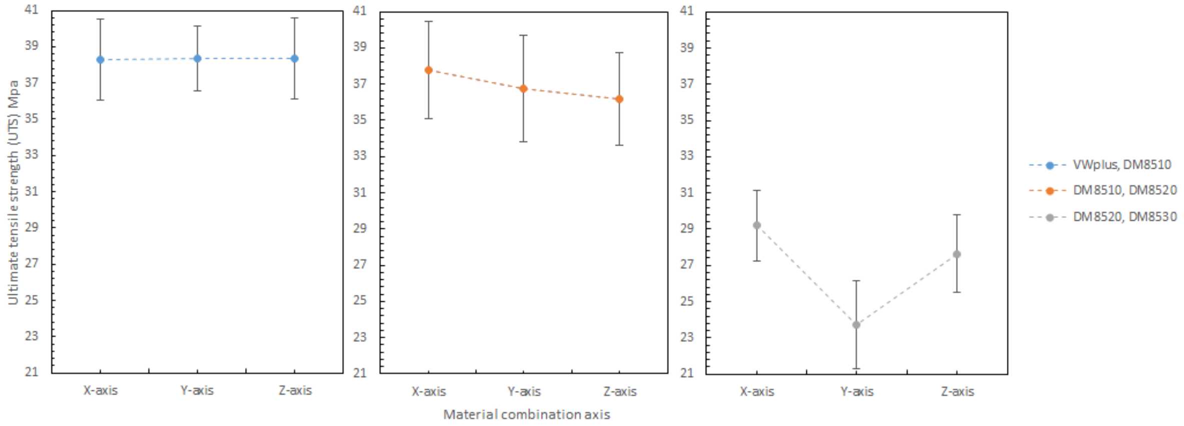

Figure 65. Combination axis effect on UTS at 25 degree Celsius

Shown in Figure 66 is the material combination axis effect on maximum strain at 25℃. Clearly, the combination axis did affect the maximum strain. For all different materials, maximum strain increased in the order: Y-axis < X-axis < Z-axis. The reason was that Z-axis has most surface contact between two materials, allowing more slippery plastic deformation.

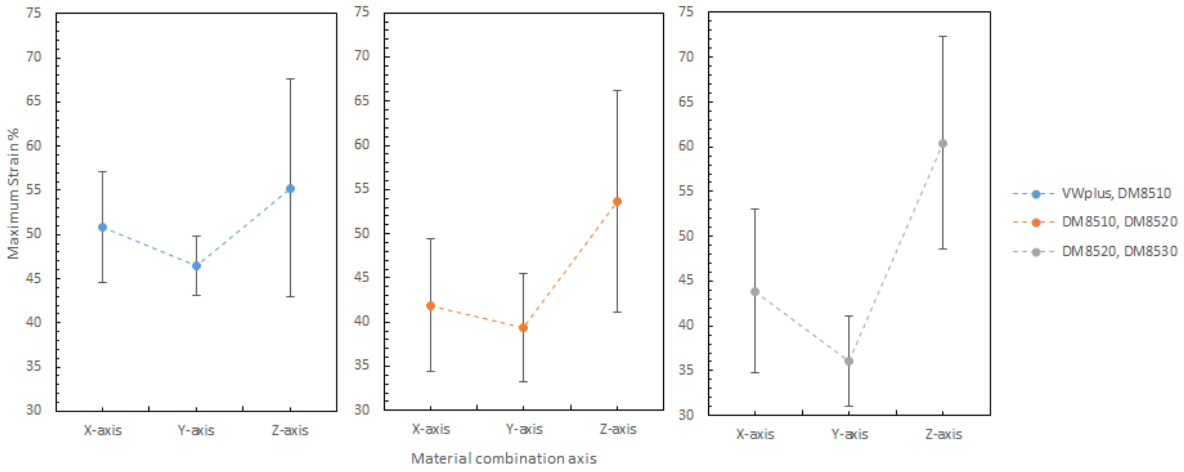

Figure 66. Combination axis effect on maximum strain 25 degree Celsius

Shown in Figure 67 is the material combination axis effects on Young’s Modulus, which have been briefly mentioned in Table 5 earlier. For Young’s Modulus, it decreased in the order: X-axis > Y-axis > Z-axis. The reason was the imperfect interfacial adhesion between 2 materials. During 3D printing, thermoset polymer’s properties give materials irreversible cross-links after heating and curing. As 3D printing is line by line, there is a very high chance that the previous line is heated and half cured. When next line is printed beside the first line, the bonding between these two lines is not 100% bonded as cured materials cannot be bonded perfectly onto the previous layer. It is physical bonding between these two lines, instead of chemical bonding within the individual lines. This applied to different material boundary as well. Between material 1 and material 2, the first printed material would be cured when second material was printed beside it, resulting in imperfect bonding at the material boundary which weakened the bonding and made the specimen more elastic by allowing more slippery movement. Longitudinal adhesion along the loading direction was stronger than the transverse adhesion to the loading direction. This was the reason for specimen with X-axis (longitudinal loading) orientation having a greater Young’s Modulus value than Y-axis (transverse loading).

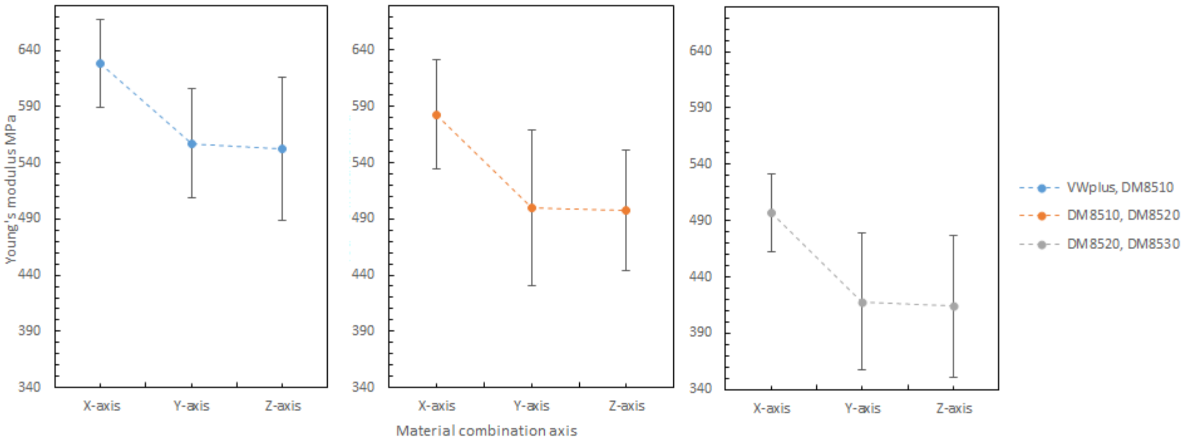

Figure 67. Combination axis effect on Young's Modulus 25 degree Celsius

5.3.4 Recovery of crossfolded multimaterial smart structures

Figure 68 shows the folding line 3 of the petiole (stem) at the lower end of the petal, which involvesd just the bending of a single material into a bud shape. Figure 69 shows the folding line 2 of the petal which involved the folding of two different materials with different T_g. Figure 70 shows the material placement and the axes of crossfolding of the structure.

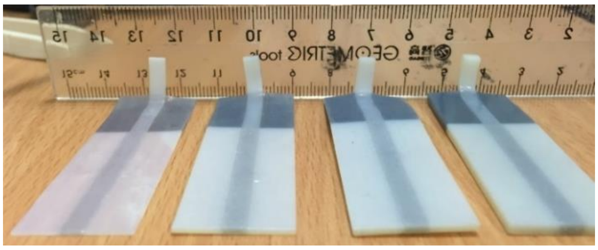

Figure 68. Folding line 3

Figure 69. Folding line 2

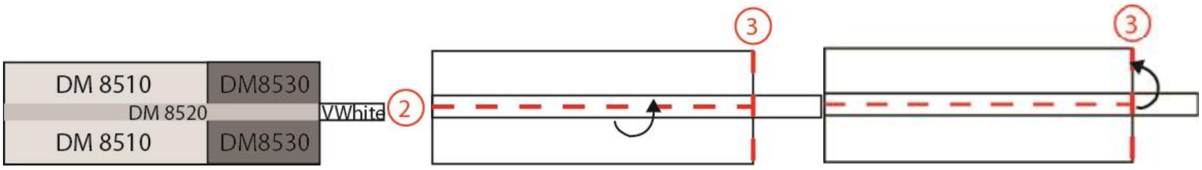

Figure 70. Materials and folding line 2&3

The data shown in Table 11 explains varying the different thickness of the structure, the upper boundary (maximum) thickness 0.5, 1.0, 1.5, 2.0 mm and lower boundary (minimum) thickness 0.1, 0.3 mm were printed. The different T_g materials were allocated to the structure. The structure represented the petal in a simplified geometric form instead of a curved shape for experimental purpose so that observation of minor changes could be recorded accurately. However, if pressure was applied for folding line 3 or folding line 2, the structure could not be accurately controlled due to manual manipulation. Thickness of the structure was relevant when designing the flower with the combination of the basic designs. From the experiment, it was observed that the thicker the folding line 3 on the structure, the longer it took for the structure to recover to its original geometry. This was because a longer time was required for the centre of a thicker sample to be heated to above its T_g, which lengthened the overall recovery time.

Table 11. Recovery time of folding line 3

Folding Line 3 (Temperature: 70°C -73°C)	
Thickness (mm)	Time to recover (s)
0.1	N/A
0.3	0.9
0.5	1.8
1	2
1.5	8
2	11

Similar to the folding line 3 in Table 12, it was observed that the thicker the folding structure, the longer it took for the structure to recover to its original geometry.

Table 12. Recovery time of folding line 2

Folding line 2 (Temperature: 70°C -73°C)	
Thickness (mm)	Time to recover (s)
0.1	0.7
0.3	1.1
0.5	4
1	5
1.5	11
2	Breakage

The experiment shows that the thinner the thickness, the quicker the response time. Also, from the graph in Figure 71, it can be seen that the recovery rate for folding line 2 of the petal is longer than for the folding line 3 of the petiole.

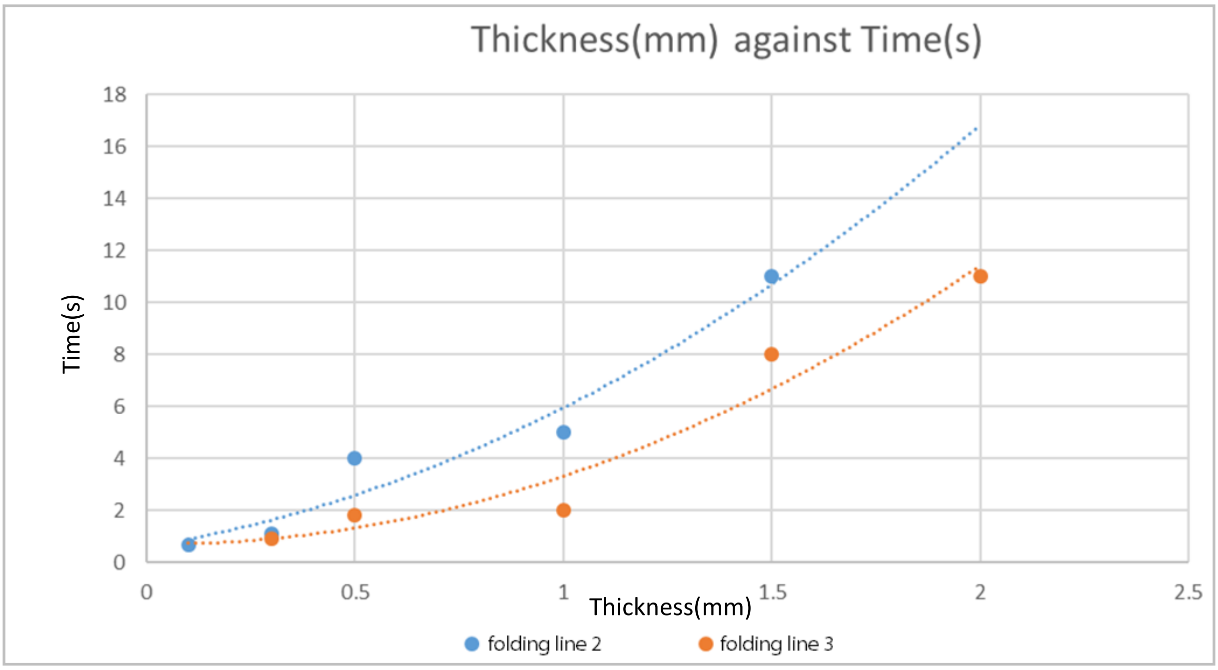

Figure 71. Thickness against recovery time

The multi-component strip of thickness 1 mm was 3D printed and programmed into the folded structure. Different materials were applied to the designed location on the strip to mimic the petal. Thermal stimulus was applied to activate the structure according to the material T_g and it was shown that for both methods, crossfolding was achievable in the experiments conducted. During method 1, folding line 1 first and then folding line 2 and vice versa for method 2 were experimented.

In Figure 72 (3-8), the lower T_g of DM8530 has a lower T_g than DM8510. It can be seen that the sequence of the unfolding shows that DM8530 (darker grey) opened earlier than DM8510 (white material) with a higher T_g for the material to respond to thermal stimulus.

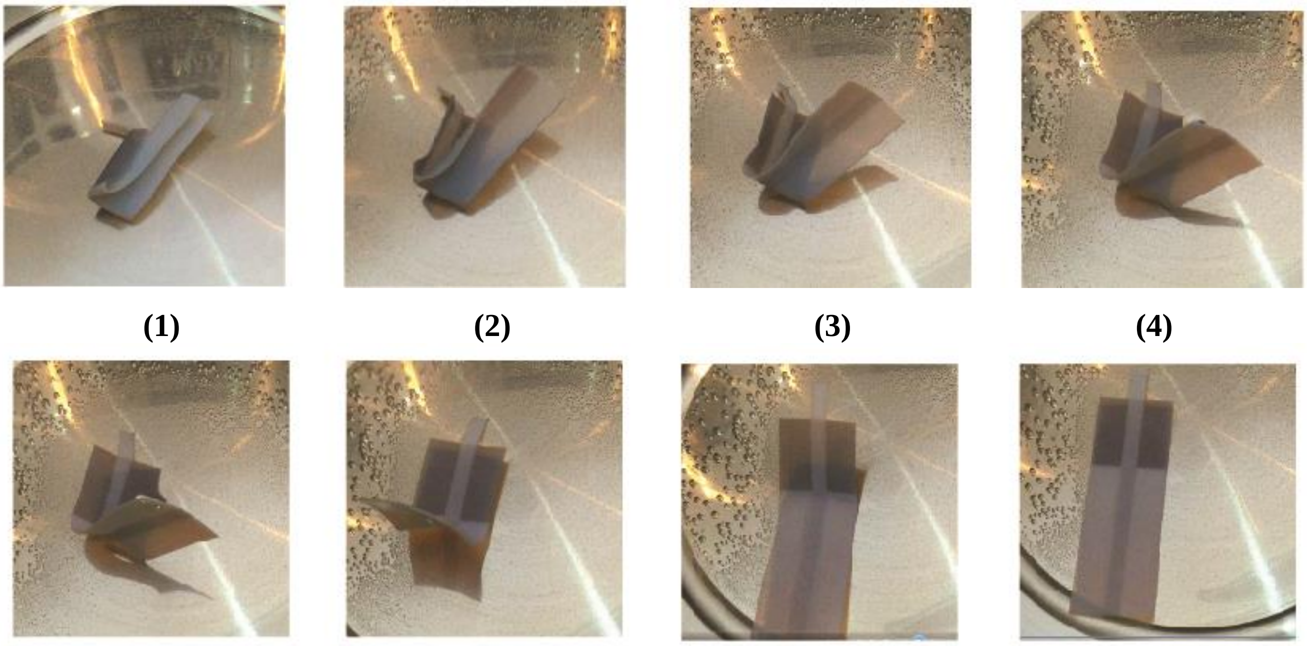

(1) **(2)** **(3)** **(4)**

(5) **(6)** **(7)** **(8)**

Figure 72. Method 1- The sequence of unfolding from (1) to (8)

During method 2, folding line 2 first and then folding line 1, it was observed that a turning movement was created by the folding sequence. This depended on the folding order and material allocation on the strip. In the folding order, it was observed that when programming, the reverse method was done to predict the sequence of the unfolding order.

This was similar to the cross folding method 1. It was due to the lower T_g of DM8530. It can be seen that the sequence of the unfolding at Figure 73(4-8) shows that darker grey area (DM8530) opened earlier than the white material (DM8510).

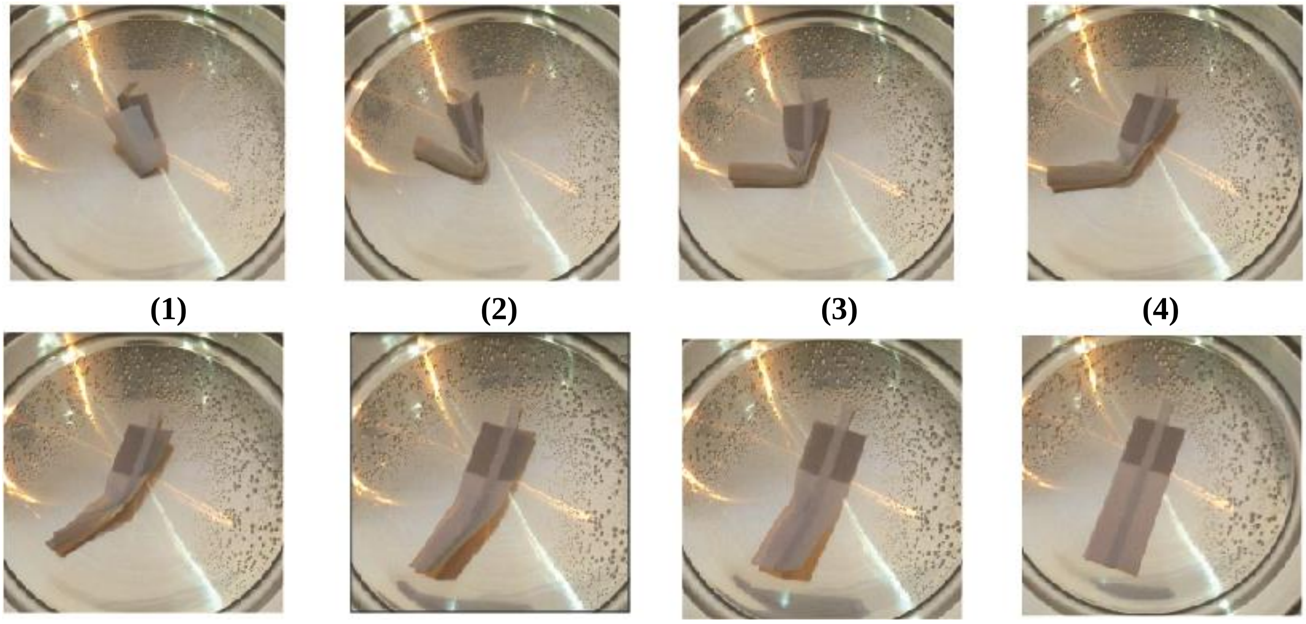

(1) **(2)** **(3)** **(4)**

(5) **(6)** **(7)** **(8)**

Figure 73. Method 2- The sequence of unfolding from (1) to (8)

5.3.5 Summary

For single material structures, a series of tests were conducted using specimens with different horizontal hinge thickness for multi-folding process. The structures with smaller thickness would recover first independent of the folding sequence. Horizontal hinge of 0.5 mm thickness could only be repeatedly folded for three times, while 0.3 mm thickness could only be folded once prior to fracture cracked. The structure with 0.1 mm thickness has very low structural strength, it was either not able to recover back or even break at the first folding. All specimens with a hole in the centre showed reduction in the stress concentration and fracture cracks. For multimaterial structures, combining multimaterial components along different axes did affect the maximum strain and young's modulus of the composite, but the effect on UTS was mixed. Assembling a flower petal, sequential unfolding of multimaterial structures, which was designed with a combination of overlapping and non-overlapping folding lines, was successfully demonstrated. Different thicknesses at different folding lines resulted in different recovery time. Overall the development of design guidelines for accessing material cross-foldability was accomplished. Although crossfolding was possible in 4D printing, the radius of curvature during folding needed to be further minimized in future.

CHAPTER SIX - CONCLUSION AND FUTURE WORK

6.1 Conclusion

This research has fulfilled the project objectives: (1) design of multimaterial-based smart structures via fracture avoidance; (2) design of geometry-based smart structures via heat transfer; and (3) smart multistage complex cross-folding. Design methodologies have been proposed and key research contributions are elaborated in the following sections.

6.1.1 A critical review on design guidelines for polymeric 4D printing

Published literature on design guidelines for polymeric 4D printing were critically reviewed together and compared with results from our ongoing research. Research publications on 4D printing were classified according to the type of external stimulus. Even though there are research publications in the area of 4D printed smart structures, it is found that methodologies and guidelines on designing a 4D printed structure are lacking. Another key challenge in 4D printing is intrinsic limitation in thermomechanical and mechanical properties of shape memory polymer materials.

6.1.2 Design of multimaterial-based smart structures via fracture avoidance

Design, analysis and experimental characterization of multimaterial smart structures were implemented using a single petal design to achieve higher order shape memory response. Graded distribution of heterogeneous materials within a single petal was analyzed for variable angle response when external stimulus was applied. Thermal analysis was also carried out to determine transient and steady-state temperature distribution when external stimulus was applied. By carefully determining minimum allowable bend radius and selectively deploying different SMPs at both global and system levels, a hierarchically self-morphing artificial orchid flower which was thermally activated to blossom in an ambient environment was successfully

3D printed. The design principle for selecting proper thickness would be useful for other 4D printing approaches to avoid material fracture during shape-setting stage. This approach will enable highly complex origami structures by leveraging on multiple petals. This provides a more realistic simulation of flower blooming response. The petal was designed and experimented with thermal stimulus. The system level design was made up of the basic design of a single petal. One example is the flower blooming process. The varying shape memory materials was used to demonstrate this phenomenon.

6.1.3 Design of geometry-based smart structures via heat transfer

In order to investigate the effect of thickness on the response time, 3D printed shape memory polymers have been investigated in both 2D and 3D smart structures (i.e. L-hinges, spiral square and orchid flower). Printed material thickness affects heat transfer characteristics and hence will determine initial response time and full shape recovery duration. Therefore, in this research, the printed thickness was used as a controllable parameter during the structure fabrication process to determine the shape recovery characteristics and sequence in a complex structure. This presents an alternative approach to the use of materials with different properties. In addition, this approach will also enable higher resolution control of sequential shape recovery compared with the sole use of material Tg which is only available for limited values. This approach will provide additional degree of freedom for designing complex responses of 4D printed smart structures, especially when employed in combination with multi-material based approach.

6.1.4 Smart multistage complex cross-folding

A series of experimental tests were conducted using specimens with different horizontal hinge thickness parameters to analyse multi-folding characteristics in structures with single materials. The following key results were determined from the experimental tests: structures with smaller thickness would recover first independent of the folding sequence, horizontal hinge of 0.5 mm thickness could only be repeatedly folded three times, while hinge of 0.3 mm thickness could only be folded once prior to fracture. Structures with 0.1 mm thickness had very low structural strength and any form of shape recovery was not achievable. The experimental tests were repeated for structures with the addition of a physical hole in the centre. Results for these tests indicated the physical hole provided stress relief or reduced stress concentration and eliminate fracture cracks.

Experimental tests performed for multi-material structures indicated that multi-material component printing along different axes had strong impact on the effective Young's modulus of the composite structure and hence, the maximum fracture strength. A flower petal shape recovery structure, consisting of sequential unfolding of multi-material structures designed with a combination of overlapping and non-overlapping folding lines, was demonstrated. Different thicknesses at different folding lines resulted in different recovery time. Overall the development of design guidelines for accessing material cross-foldability was accomplished. Although cross-folding was possible in 4D printing, the radius of curvature during folding needed to be optimised in the future.

6.2 Future work

6.2.1 Finite Element Analysis (FEA) modelling for crossfolding

Using the thickness variation for single material crossfolding to create more complex structures will be carried out in this project. Work conducted on crossfolding can be further explored by carrying out ANSYS simulation test for thermal transient temperature and stress and strain before printing 3D structures to obtain results of stress and strain points on the structure.

6.2.2 Fracture for hole dimensions

To reduce fracture during crossfolding, the physical clearance area provides stress relief. To further investigate and optimise the clearance hole dimension of the structure will reduce fracture.

6.2.3 Combining design guidelines for 4D printing structures

The varying materials will be applied to the different sections of the flower and programmed according to their folds and creases. The flower will be designed according to their thickness and their Tg materials based on the data.

To further increase the complexity of a structure, a possible extension to the study can include combining the design guidelines of multimaterial-based smart structures via fracture avoidance, geometry-based smart structures via heat transfer and smart multistage complex crossfolding. The favourable results summarised above showed that the design guidelines for 4D printing is a novel concept for future applications. The need for intensive systematic investigation of the 3D printed structure is to be activated or used repeatedly, to improve structures for more fatigue and to withstand more number of cycles. Other mechanical factors such as cyclic mechanical folding test could be considered for crossfolding. The specimen flower petal of different thickness will be subjected to tension and back to recovery until breakage occurs. Lastly, the mechanics of flower blooming which has a complex movement from the vertical movement of the stem to the twisting of petals could be explored.

6.3 List of publications

The author has generated a number of publications throughout the course of this research. The publications include five international peer reviewed journal papers, three international conference papers and one technology disclosure.

6.3.1 International peer reviewed journal papers

J. An, **J. E. M. Teoh**, R. Suntornnond, and C. K. Chua, "Design and 3D printing of scaffolds and tissues," Engineering, 2015.

Z. X. Khoo, **J. E. M. Teoh**, Y. Liu*, C. K. Chua, S. F. Yang, J. An, K. F. Leong, W. Y. Yeong, "3D Printing of Smart Materials: A Review on Recent Progresses in 4D Printing," Virtual and Physical Prototyping, 2015.10(3): p. 103-122.

Teoh, J. E. M., An, J., Chua, C. K., Lv, M., Krishnasamy, V., & Liu, Y. Hierarchically self-morphing structure through 4D printing. Virtual and Physical Prototyping, 2017. 12(1): p. 61-68.

Teoh, J.E.M., Zhao,Y., An, J., Chua, C. K., & Liu, Y. Multistage responsive 4D printed smart structure through varying geometric thickness of shape memory polymer. Smart Materials and Structures, 2017. 26(12): p. 125001.

Teoh, J.E.M., Xiao, F., Zhao,Y., An, J., Chua, C. K., & Liu, Y. Design of Crossfolding-Based Smart Structures, Materials, 2018. 11: p. 376.

6.3.2 Technology disclosure

Technology Disclosure **Teoh, J. E. M.**, Chua, C. K., Liu, Y., & An, J, 4D printing of reconfigurable objects via digital materials printing. TD252/15.

6.3.3 International conference papers

<u>J. E. M. Teoh</u>, C. K. Chua, Y. Liu, and D. Q. Zhang, "Four dimension (4D) printing using PolyJet technology," in *The 4th International Conference on Additive Manufacturing and Bio-Manufacturing*, Xijian Hotel Convention Center, Beijing,12-14 November 2014.

<u>J. E. M. Teoh</u>, C. K. Chua, Y. Liu, J. An and Y. Li, “Preliminary investigation of Four dimension (4D) printing technology for deployable UAV development," in *The 2nd International Conference on Additive Manufacturing*, Nanyang Technological University, Singapore,16-19 May 2016.

<u>Teoh, J. E. M.</u>, Chua, C. K., Liu, Y., & An, J. (2017). 4D printing of customised smart sunshade: A conceptual study. In Challenges for Technology Innovation: An Agenda for the Future (pp. 105-108). CRC Press.

REFERENCES

1. S. S. Patel, I. J. G. Zuazola, and a.W.G. Whittow., *Antenna with three dimensional 3D printed substrates*, in *Microwave and Optical Technology Letters*. April 2016. p. 741-744.
2. Pei, E., *4D printing–revolution or fad?* Assembly Automation, 2014. **34**(2): p. 123-127.
3. Pei, E., *4D Printing: dawn of an emerging technology cycle.* Assembly Automation, 2014. **34**(4): p. 310-314.
4. Campbell, T.A., S. Tibbits, and B. Garrett, *The programmable world.* Scientific American, 2014. **311**(5): p. 60-65.
5. Tibbits, S., *4D printing: multi-material shape change.* Architectural Design, 2014. **84**(1): p. 116-121.
6. Raviv, D., et al., *Active printed materials for complex self-evolving deformations.* Scientific reports, 2014. **4**: p. 7422.
7. Ding, Z., et al., *Direct 4D printing via active composite materials.* Science Advances, 2017. **3**(4): p. e1602890.
8. Mao, Y., et al., *Sequential self-folding structures by 3D printed digital shape memory polymers.* Scientific reports, 2015. **5**: p. 13616.
9. Ge, Q., et al., *Active origami by 4D printing.* Smart Materials and Structures, 2014. **23**(9): p. 094007.
10. Gladman, A.S., et al., *Biomimetic 4D printing.* Nature materials, 2016. **15**(4): p. 413-418.
11. Teoh, J., et al., *Hierarchically self-morphing structure through 4D printing.* Virtual and Physical Prototyping, 2017. **12**(1): p. 61-68.
12. Büchi, F.N., M. Inaba, and T.J. Schmidt, *Polymer electrolyte fuel cell durability*. 2009: Springer.
13. Chae, M.P., et al., *Four-Dimensional (4D) Printing: A New Evolution in Computed Tomography-Guided Stereolithographic Modeling. Principles and Application.* Journal Of Reconstructive Microsurgery, 2015. **31**(6): p. 458-463.
14. Gao, B., et al., *Review: 4D Bioprinting for Biomedical Applications.* Trends in Biotechnology, 2016.
15. Crump, S.S., et al., *Process of support removal for fused deposition modeling*. 1996, Google Patents.
16. Mitcham, L.D. and W.E. Nelson, *Stereolithographic apparatus and method of use*. 1993, Google Patents.
17. Bremen, S., W. Meiners, and A. Diatlov, *Selective laser melting.* Laser Technik Journal, 2012. **9**(2): p. 33-38.
18. Shin, D.-G., T.-H. Kim, and D.-E. Kim, *Review of 4D printing materials and their properties.* International Journal of Precision Engineering and Manufacturing-Green Technology, 2017. **4**(3): p. 349-357.
19. Meng, H. and G. Li, *A review of stimuli-responsive shape memory polymer composites.* Polymer, 2013. **54**(9): p. 2199-2221.
20. Khoo, Z.X., et al., *3D printing of smart materials: A review on recent progresses in 4D printing.* Virtual and Physical Prototyping, 2015. **10**(3): p. 103-122.
21. Gibson, I., D.W. Rosen, and B. Stucker, *Additive manufacturing technologies*. Vol. 238. 2010: Springer.
22. Utela, B., et al., *A review of process development steps for new material systems in three dimensional printing (3DP).* Journal of Manufacturing Processes, 2008. **10**(2): p. 96-104.

23. Xu, F., H.T. Loh, and Y.S. Wong, *Considerations and selection of optimal orientation for different rapid prototyping systems.* Rapid Prototyping Journal, 1999. **5**(2): p. 54-60.
24. Berman, B., *3-D printing: The new industrial revolution.* Business horizons, 2012. **55**(2): p. 155-162.
25. Campbell, T., et al., *Could 3D printing change the world.* Technologies, Potential, and Implications of Additive Manufacturing, Atlantic Council, Washington, DC, 2011.
26. Petrick, I.J. and T.W. Simpson, *3D printing disrupts manufacturing: how economies of one create new rules of competition.* Research-Technology Management, 2013. **56**(6): p. 12-16.
27. Chua, C.K. and K.F. Leong, *3D printing and additive manufacturing: principles and applications*. 5th edition, 2017: World Scientific.
28. Lipson, H. and M. Kurman, *Fabricated: The new world of 3D printing*. 2013: John Wiley & Sons.
29. Anastasiou, A., et al. *3D printing: Basic concepts mathematics and technologies*. in *Bioinformatics and Bioengineering (BIBE), 2013 IEEE 13th International Conference on*. 2013. IEEE.
30. Chua, C.K., J.G.K. Gan, and M. Tong, *Interface between CAD and rapid prototyping systems. Part 1: a study of existing interfaces.* The International Journal of Advanced Manufacturing Technology, 1997. **13**(8): p. 566-570.
31. Bianconi, F., *Bridging the gap between CAD and CAE using STL files*. International Journal of CAD/CAM, 2009. **2**(1).
32. Barclift, M.W. and C.B. Williams. *Examining variability in the mechanical properties of parts manufactured via PolyJet direct 3d printing*. in *International Solid Freeform Fabrication Symposium, August*. 2012.
33. Dimitrov, D., K. Schreve, and N.d. Beer, *Advances in three dimensional printing – state of the art and future perspectives.* Rapid Prototyping Journal, 2006. **12**(3): p. 136-147.
34. Masood, S.H., *Intelligent rapid prototyping with fused deposition modelling.* Rapid Prototyping Journal, 1996. **2**(1): p. 24-33.
35. Graves, A., *Stereolithography vs. PolyJet: Photopolymer 3D Printing Materials and Applications.* R&D Magazine, 2016. **58**(1): p. 14-17.
36. Pei, D.E., *4D Printing - Dawn of an Emerging Technology Cycle.* Assembly Automation, 2014. **34**(4): p. 1-8.
37. Vaupotič, B., M. Brezočnik, and J. Balič, *Use of PolyJet technology in manufacture of new product.* Journal of Achievements in Materials and Manufacturing Engineering, 2006. **18**(1-2): p. 319-322.
38. Gaynor, A.T., et al., *Multiple-Material Topology Optimization of Compliant Mechanisms Created Via PolyJet Three-Dimensional Printing.* Journal of Manufacturing Science and Engineering, 2014. **136**(6): p. 061015.
39. Newswire, P.R. *Unique 3D Printed Color Multi-Material Fashion Collection Produced Using Objet500 Connex3 3D Printer*. in bc-Stratasys, ; ed: Y, 2014:[
40. Chua, C.K., S.M. Chou, and T.S. Wong, *A study of the state-of-the-art rapid prototyping technologies.* The International Journal of Advanced Manufacturing Technology. **14**(2): p. 146-152.
41. Khoo, Z.X., et al., *3D printing of smart materials: A review on recent progresses in 4D printing.* Virtual & Physical Prototyping, 2015. **10**(3): p. 103-122.
42. Tobushi, H., et al., *Thermomechanical properties in a thin film of shape memory polymer of polyurethane series.* Smart Materials and Structures, 1996. **5**(4): p. 483.
43. Otsuka, K. and C.M. Wayman, *Shape memory materials*. 1999: Cambridge university press.

44. Meng, Q. and J. Hu, *A review of shape memory polymer composites and blends.* Composites Part A: Applied Science and Manufacturing, 2009. **40**(11): p. 1661-1672.
45. Tobushi, H., et al., *Thermomechanical constitutive model of shape memory polymer.* Mechanics of materials, 2001. **33**(10): p. 545-554.
46. Maitland, D.J., et al., *Photothermal properties of shape memory polymer micro‐actuators for treating stroke*.* Lasers in Surgery and Medicine, 2002. **30**(1): p. 1-11.
47. Lan, X., et al., *Fiber reinforced shape-memory polymer composite and its application in a deployable hinge.* Smart Materials and Structures, 2009. **18**(2): p. 024002.
48. Meng, Q., J. Hu, and L. Yeung, *An electro-active shape memory fibre by incorporating multi-walled carbon nanotubes.* Smart materials and structures, 2007. **16**(3): p. 830.
49. Meng, Q., et al., *Morphology, phase separation, thermal and mechanical property differences of shape memory fibres prepared by different spinning methods.* Smart materials and structures, 2007. **16**(4): p. 1192.
50. Lendlein, A. and R. Langer, *Biodegradable, elastic shape-memory polymers for potential biomedical applications.* Science, 2002. **296**(5573): p. 1673-1676.
51. Metcalfe, A., et al., *Cold hibernated elastic memory foams for endovascular interventions.* Biomaterials, 2003. **24**(3): p. 491-497.
52. Wache, H., et al., *Development of a polymer stent with shape memory effect as a drug delivery system.* Journal of Materials Science: Materials in Medicine, 2003. **14**(2): p. 109-112.
53. Charlesby, A., *Atomic Radiation and Polymers: International Series of Monographs on Radiation Effects in Materials*. Vol. 1. 2013: Elsevier.
54. Lendlein, A. and R. Langer, *Self-expanding device for the gastrointestinal or urogenital area*. 2004, Google Patents.
55. Tobushi, H., et al., *Influence of strain-holding conditions on shape recovery and secondary-shape forming in polyurethane-shape memory polymer.* Smart materials and structures, 2006. **15**(4): p. 1033.
56. Tobushi, H., et al., *The influence of shape-holding conditions on shape recovery of polyurethane-shape memory polymer foams.* Smart Materials and Structures, 2004. **13**(4): p. 881.
57. Marco, D., *Biodegradable self-inflating intragastric implants and method of curbing appetite by the same*. 2006, Google Patents.
58. Hayashi, S., et al., *Development of smart polymer materials and its various applications.* Mitsubishi Juko Giho, 2004. **41**(1): p. 62-64.
59. Behl, M. and A. Lendlein, *Shape-memory polymers.* Materials today, 2007. **10**(4): p. 20-28.
60. Ware, T., et al., *Triple-shape memory polymers based on self-complementary hydrogen bonding.* Macromolecules, 2012. **45**(2): p. 1062-1069.
61. Yu, K., et al., *Controlled sequential shape changing components by 3D printing of shape memory polymer multimaterials.* Procedia IUTAM, 2015. **12**: p. 193-203.
62. Lendlein, A. and S. Kelch, *Shape-memory polymers.* Angewandte Chemie International Edition, 2002. **41**(12): p. 2034-2057.
63. Rossiter, J., P. Walters, and B. Stoimenov, *Printing 3D dielectric elastomers actuators for soft robotics.* Proc. of SPIE, 2009. **7287**.
64. Raviv, D., et al., *Active printed materials for complex self-evolving deformations.* Scientific Report, 2014. **4**(7422).
65. Ivanovaa, O., et al., *Uncloable security features for additive manufacturing.* Additive Manufacturing 1-4, 2014: p. 24-31.
66. Ge, Q., H.J. Qi, and M.L. Dunn, *Active materials by four-dimension printing.* Applied Physics Letters, 2013. **103**(131901).

67. Ge, Q., et al., *Active origami by 4D printing.* Smart materials and structures, 2014. **23**(094007).
68. Bakarich, S.E., R. Gorkin, and G.M. Spinks, *4D printing with mechanically robust, thermally actuating hydrogels.* Macromolecular rapid communications, 2015. **36**(12): p. 1211-1217.
69. Sydney Gladman, A., et al., *Biomimetic 4D printing.* Nat Mater, 2016. **advance online publication**.
70. Lendlein, A., et al., *Light-induced shape-memory polymers.* Nature, 2005. **434**(7035): p. 879-882.
71. Chen, M., et al., *Photodeformable polymer material: towards light-driven micropump applications.* Applied Physics A: Materials Science & Processing, 2010. **100**(1): p. 39-43.
72. Lee, K.M., et al., *Light-activated shape memory of glassy, azobenzene liquid crystalline polymer networks.* Soft Matter, 2011. **7**(9): p. 4318-4324.
73. Lee, K.M., et al., *Photomechanical mechanism and structure-property considerations in the generation of photomechanical work in glassy, azobenzene liquid crystal polymer networks.* Journal of Materials Chemistry, 2012. **22**(2): p. 691-698.
74. Mahimwalla, Z., et al., *Azobenzene photomechanics: prospects and potential applications.* Polymer Bulletin, 2012. **69**(8): p. 967-1006.
75. White, T.J., *Light to work transduction and shape memory in glassy, photoresponsive macromolecular systems: trends and opportunities.* Journal of Polymer Science Part B: Polymer Physics, 2012. **50**(13): p. 877-880.
76. Kuksenok, O. and A.C. Balazs, *Stimuli-responsive behavior of composites integrating thermo-responsive gels with photo-responsive fibers.* Materials Horizons, 2016. **3**(1): p. 53-62.
77. Zhang, X., et al., *UV light induced plasticization and light activated shape memory of spiropyran doped ethylene-vinyl acetate copolymers.* Soft matter, 2014. **10**(21): p. 3748-3754.
78. Wu, J., et al., *Multi-shape active composites by 3D printing of digital shape memory polymers.* Scientific Reports, 2016. **6**.
79. Deng, S., M. Hou, and L. Ye, *Temperature-dependent elastic moduli of epoxies measured by DMA and their correlations to mechanical testing data.* Polymer Testing, 2007. **26**(6): p. 803-813.
80. Kagan, V.A., I. Palley, and N. Jia, *Plastics part design: Low cycle fatigue strength of glass-fiber-reinforced polyethylene terephthalate (PET).* Journal of reinforced plastics and composites, 2004. **23**(15): p. 1607-1614.
81. Yonemitsu, E., et al., *Thermoplastic blend composition*. 1976, Google Patents.
82. Mondragón-Palomino, M. and G. Theißen, *MADS about the evolution of orchid flowers.* Trends in Plant Science, 2008. **13**(2): p. 51-59.
83. Mao, Y., et al., *3D Printed Reversible Shape Changing Components with Stimuli Responsive Materials.* Scientific Reports, 2016. **6**.
84. Ge, Q., et al., *Multimaterial 4D Printing with Tailorable Shape Memory Polymers.* Scientific Reports, 2016. **6**.
85. Chua, C.K. and K.F. Leong, *3D Printing and Additive Manufacturing: Principles and Applications*. 2014: World Scientific.
86. Yang, Y., et al., *3D printing of shape memory polymer for functional part fabrication.* International Journal of Advanced Manufacturing Technology, 2016. **84**(9-12): p. 2079-2095.
87. Bakarich, S.E., et al., *4D printing with mechanically robust, thermally actuating hydrogels.* Macromolecular Rapid Communications, 2015. **36**(12): p. 1211-1217.

88. Balasubramanian, A. and C.J. Bettinger, *Shape Recovery Kinetics in Vascularized 3D-Printed Polymeric Actuators.* Advanced Engineering Materials, 2015. **17**(9): p. 1287-1293.
89. Umedachi, T., V. Vikas, and B.A. Trimmer, *Softworms: The design and control of non-pneumatic, 3D-printed, deformable robots.* Bioinspiration and Biomimetics, 2016. **11**(2).
90. Rodriguez, J.N., et al., *Shape-morphing composites with designed micro-architectures.* Scientific Reports, 2016. **6**.
91. Zarek, M., et al., *3D Printing of Shape Memory Polymers for Flexible Electronic Devices.* Advanced Materials, 2016. **28**(22): p. 4449-4454.
92. Teoh, J.E.M., et al., *Hierarchically self-morphing structure through 4D printing.* Virtual and Physical Prototyping, 2017. **12**(1): p. 61-68.
93. Kakaç, S. and Y. Yener, *Heat conduction*. 1985, Univ. of Miami, Coral Gables, FL.
94. Vlachopoulos, J. and D. Strutt, *Basic Heat Transfer and Some Application in Polymer Processing*, in *Plastics Technician's Toolbox*. 2002, Society of Plastics Engineers Incorporated (SPE). p. 21-23.
95. Karwa, R., S.C. Solanki, and J.S. Saini, *Heat transfer coefficient and friction factor correlations for the transitional flow regime in rib-roughened rectangular ducts.* International Journal of Heat and Mass Transfer, 1999. **42**(9): p. 1597-1615.
96. Objet Geometries. *FullCure® Materials*. 6 June, 2017]; Available from: svl.wpi.edu/wp-content/uploads/2014/04/FullCure_Letter_low-1.pdf.
97. Mikkelson, E.C., *Characterization and Modeling of the Thermal Properties of Photopolymers for Material Jetting Processes*. 2014, Virginia Tech.
98. Laaber, D., *Usability of polymer film heat exchangers in the chemical industry.* 2017: p. 148.
99. Standard, A., *D638-02a.* Standard test method for tensile properties of plastics. West Conshohocken, PA, USA: ASTM International, 2002.
100. Askeland, D., P. Fulay, and W. Wright, *The science and engineering of materials*. 2011: Nelson Education.
101. Roylance, D., *Introduction to composite materials.* Department of Materials Science and Engineering, Massachusetts Institute of Tech., Cambridge, 2000.
102. Gooch, J.W., *Law of Mixtures*, in *Encyclopedic Dictionary of Polymers*. 2011, Springer. p. 421-421.
103. Kim, H.S., *On the rule of mixtures for the hardness of particle reinforced composites.* Materials Science and Engineering: A, 2000. **289**(1): p. 30-33.
104. *Mechanical Properties*. 2017 November 20]; Available from: http://www.materials.unsw.edu.au/tutorials/online-tutorials/1-mechanical-properties.
105. Callister, W.D. and D.G. Rethwisch, *Fundamentals of materials science and engineering*. Vol. 471660817. 2000: Wiley London.
106. Johnston, B., *Mechanics of Materials*. 5th ed. ed. 2006: McGraw Hill.
107. S. Kalpakjian, S.R.S., *Manufacturing Engineering and Technology*. International edition (4th ed) ed. Inc. 2001: Prentice Hall.
108. Ge, Q., et al., *Multimaterial 4D printing with tailorable shape memory polymers.* Scientific reports, 2016. **6**: p. 31110.

Appendix A: *DMA graph*

VeroWhitePlus:

Run 1

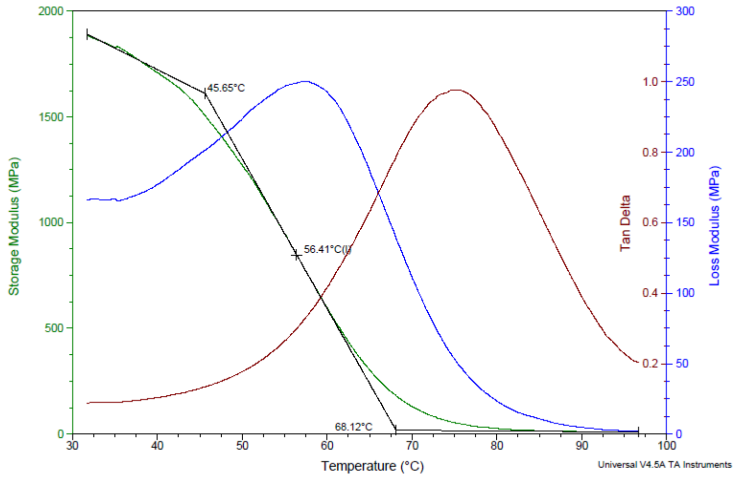

Run 2

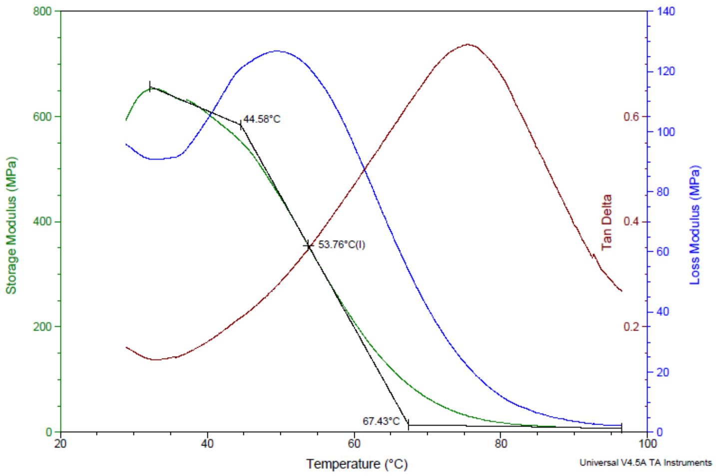

Run 3

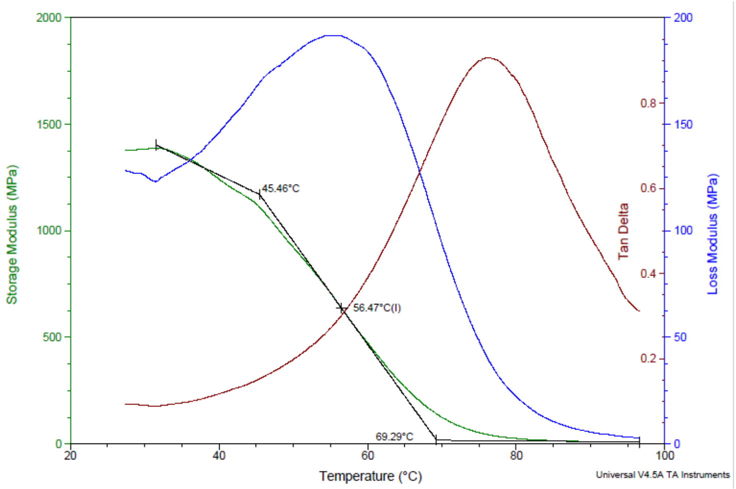

Figure 74. DMA runs for VeroWhitePlus

DM8510:

Run 1

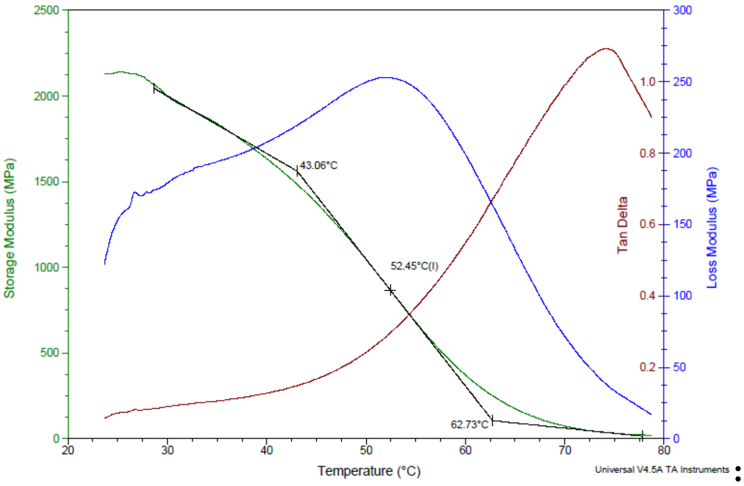

Run 2

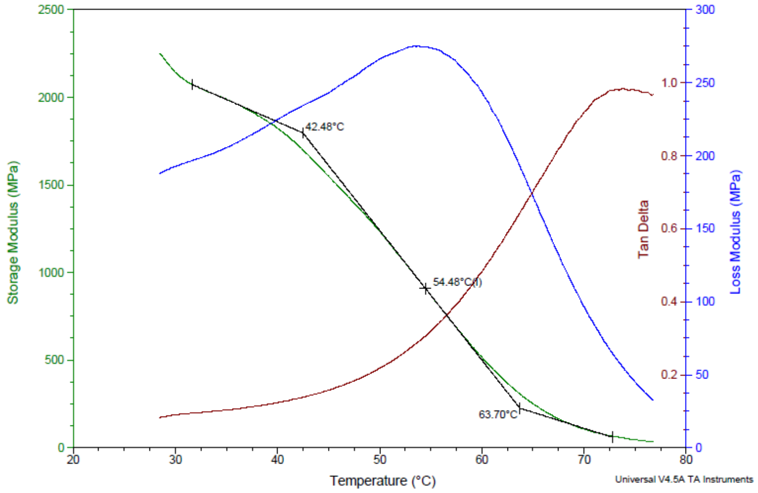

Run 3

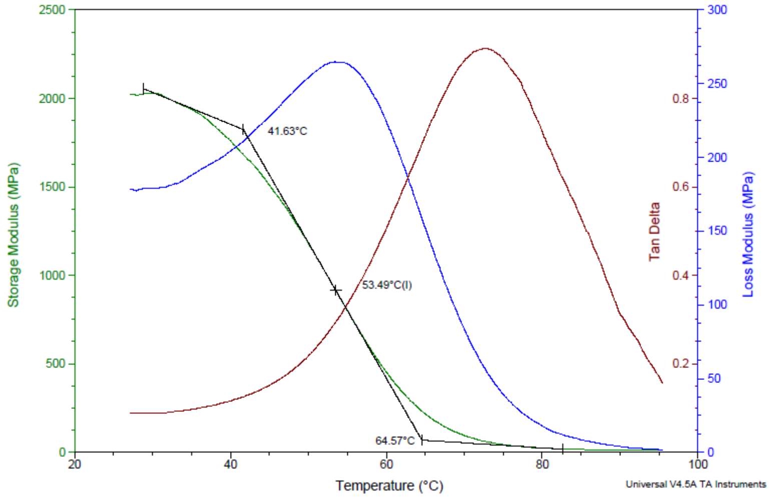

Figure 75. DMA runs for DM8510

DM8520:

Run 1

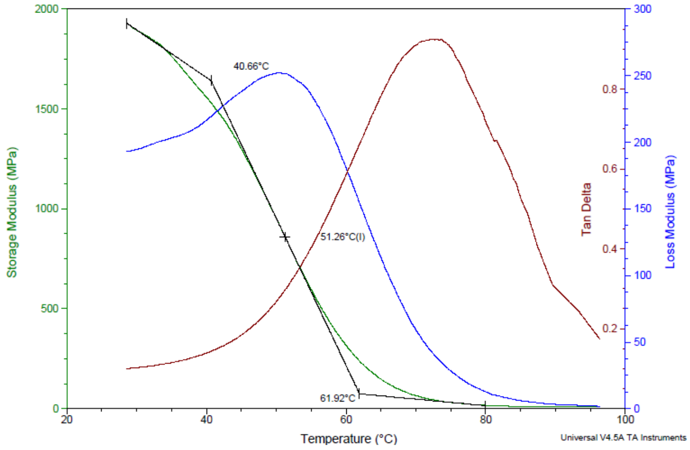

Run 2

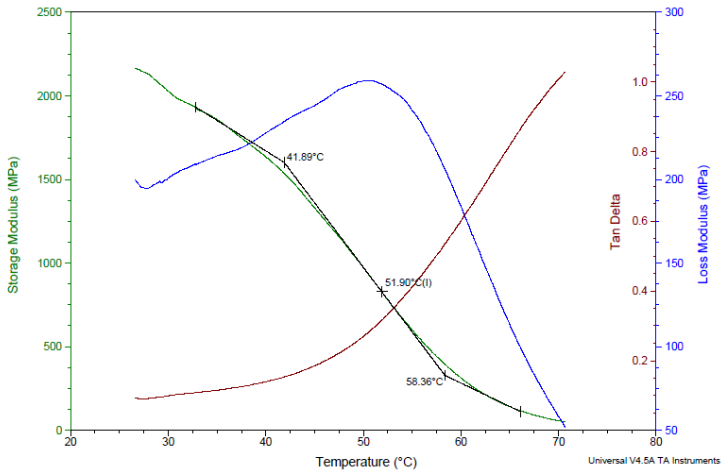

Run 3

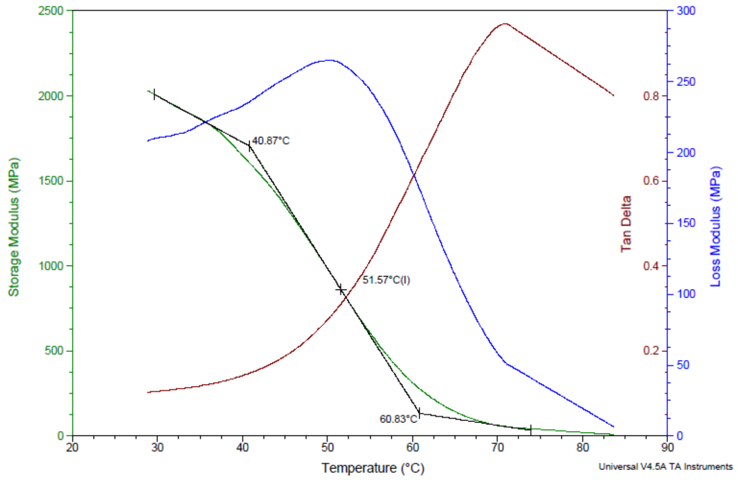

Figure 76. DMA runs for DM8520

DM8530:

Run 1

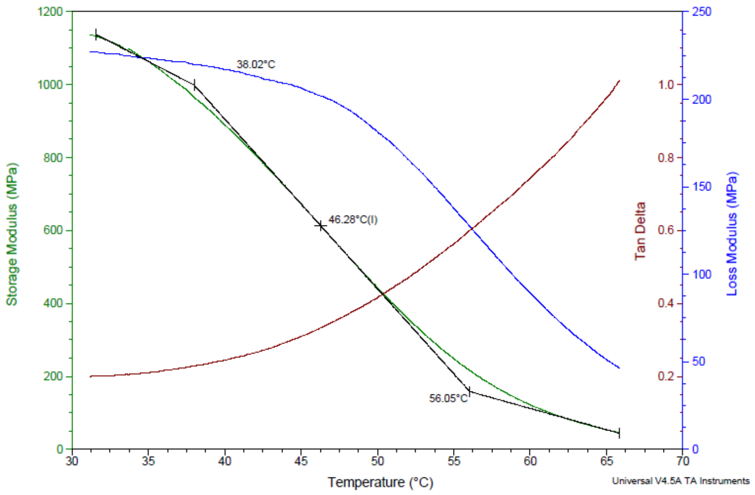

Run 2

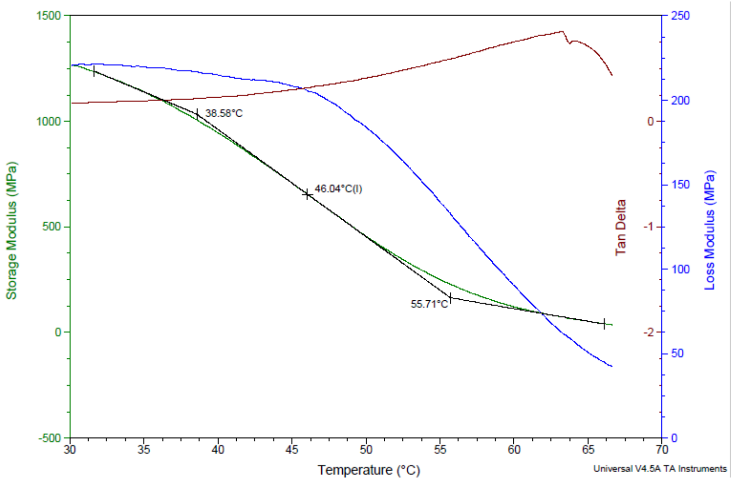

Run 3

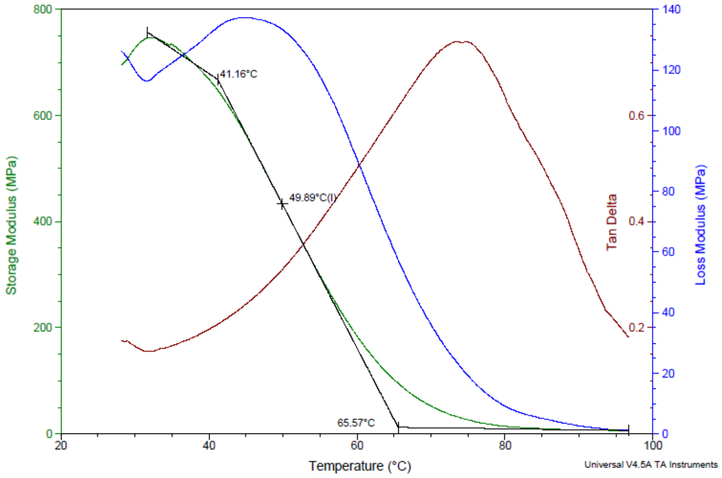

Figure 77. DMA runs for DM8530

Appendix B: ***Multi-material stress-strain curves and property data***

For D8510, D8520:

X-axis:

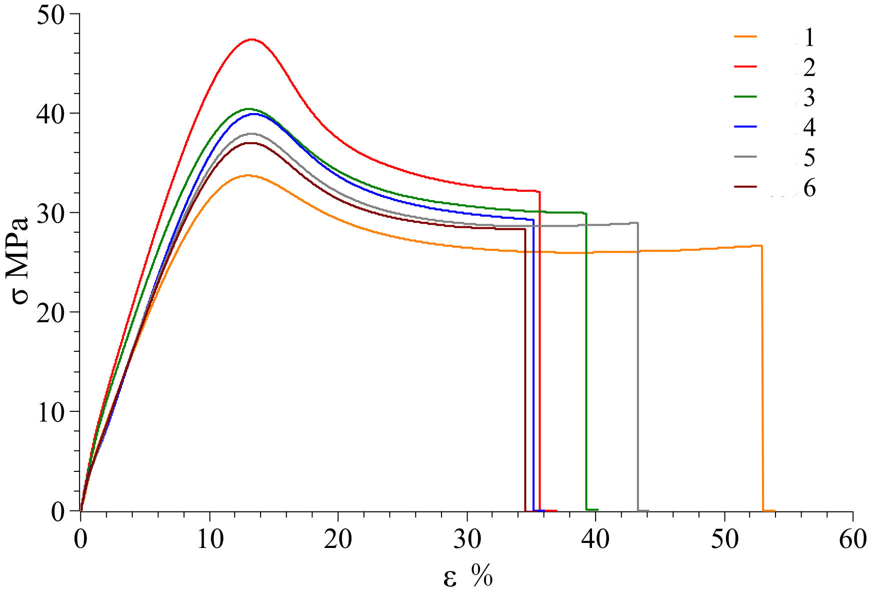

Figure 78. D8510, D8520 stress- strain curve for X-axis

Y-axis:

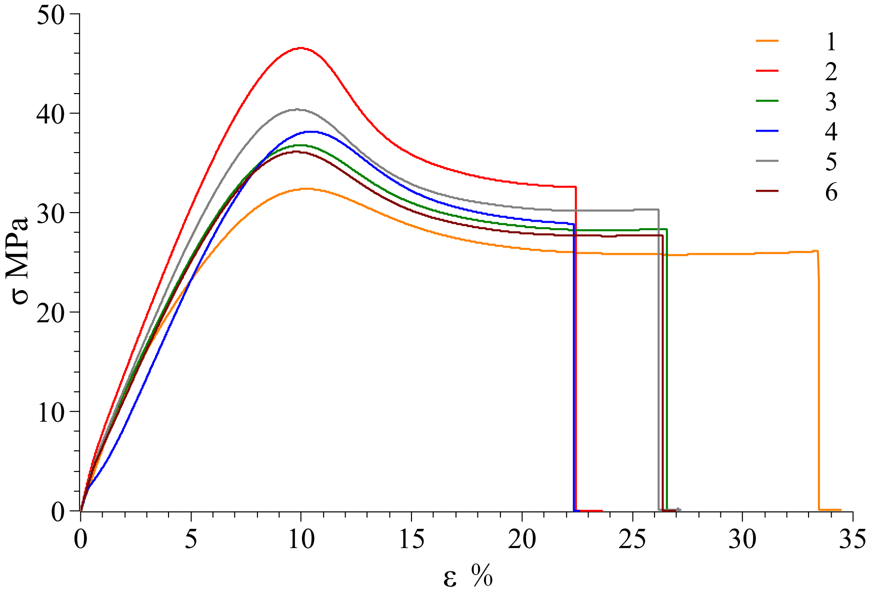

Figure 79. D8510, D8520 stress- strain curve for Y-axis

Z-axis (XY plane):

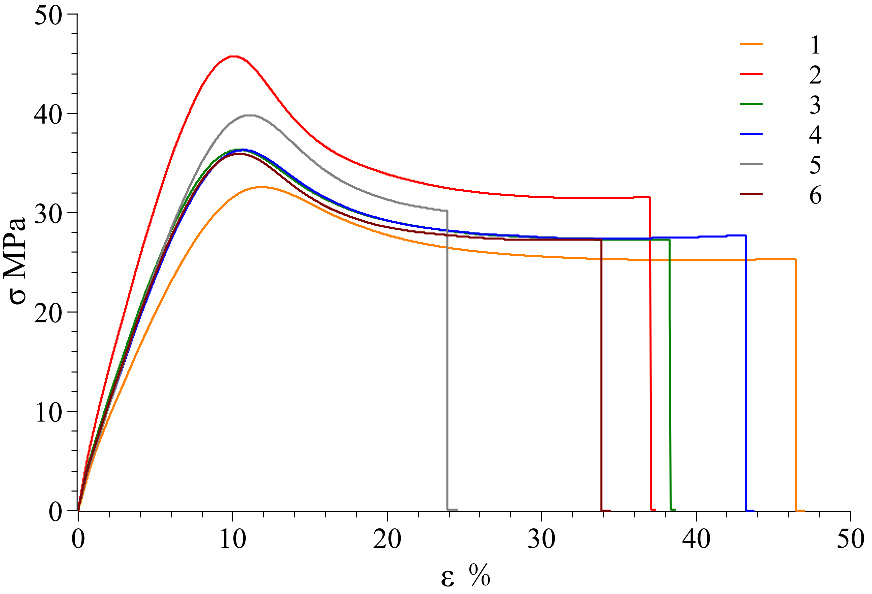

Figure 80. D8510, D8520 stress- strain curve for Z-axis(XY plane)

For D8520, D8530:

X-axis:

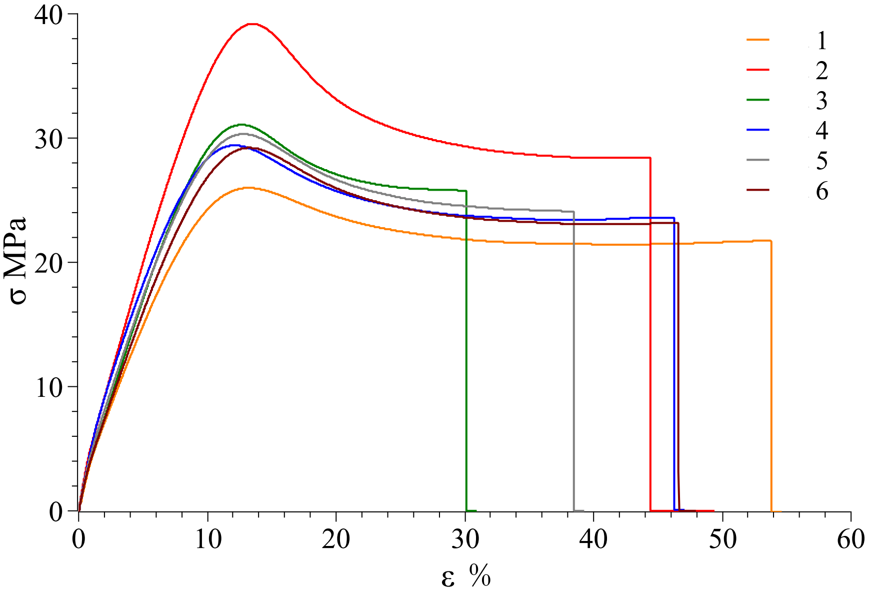

Figure 81. D8520, D8530 stress- strain curve for X-axis

Y-axis:

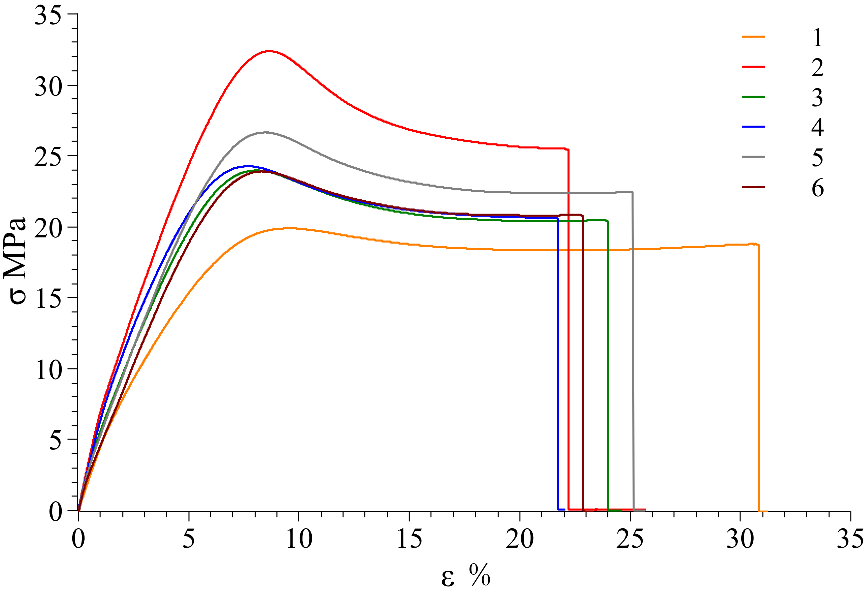

Figure 82. D8520, D8530 stress- strain curve for Y-axis

Z-axis (XY plane):

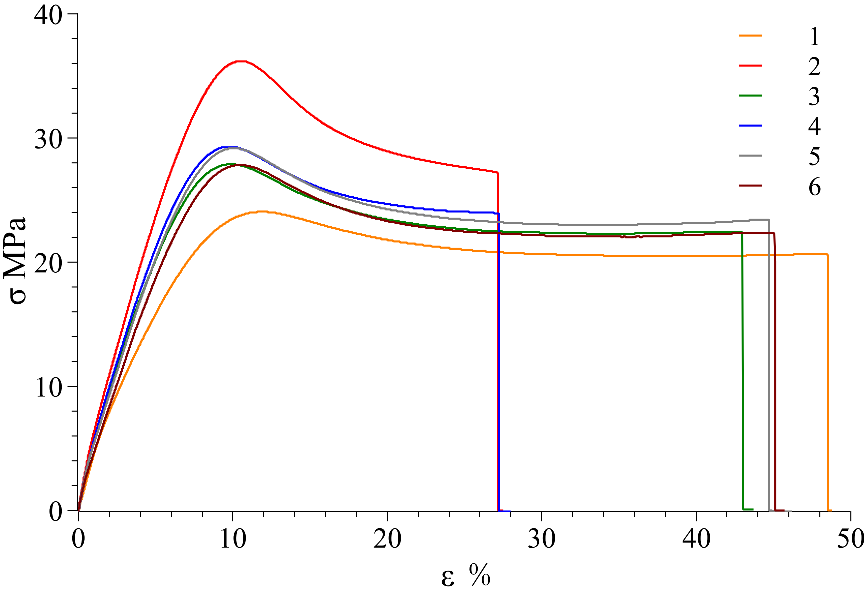

Figure 83. D8520, D8530 stress- strain curve for Z-axis(XY plane)

Table 13 D8510, D8520 combination thermal-mechanical properties

Axis	X	Standard Deviation	Y	Standard Deviation	Z	Standard Deviation
Ultimate Tensile Stress (MPa)	37.791	±2.670	36.753	±2.940	36.202	±2.559
Maximum Strain (%)	41.910	±7.548	39.341	±6.109	53.617	±12.519
Young's Modulus (MPa)	582.590	±48.531	499.329	±69.315	497.307	±53.639

***set 2, abnormal data, removed from calculation**

Table 14 D8520, D8530 combination thermal-mechanical properties

Axis	X	Standard Deviation	Y	Standard Deviation	Z	Standard Deviation
Ultimate Tensile Stress (MPa)	29.202	±1.944	23.727	±2.435	27.650	±2.124
Maximum Strain (%)	43.882	±9.123	36.114	±5.053	60.440	±11.833
Young's Modulus (MPa)	496.813	±34.982	417.935	±60.800	413.767	±63.502

***set 2, abnormal data, removed from calculation**

Appendix C: *VeroWhitePlus material sheet*

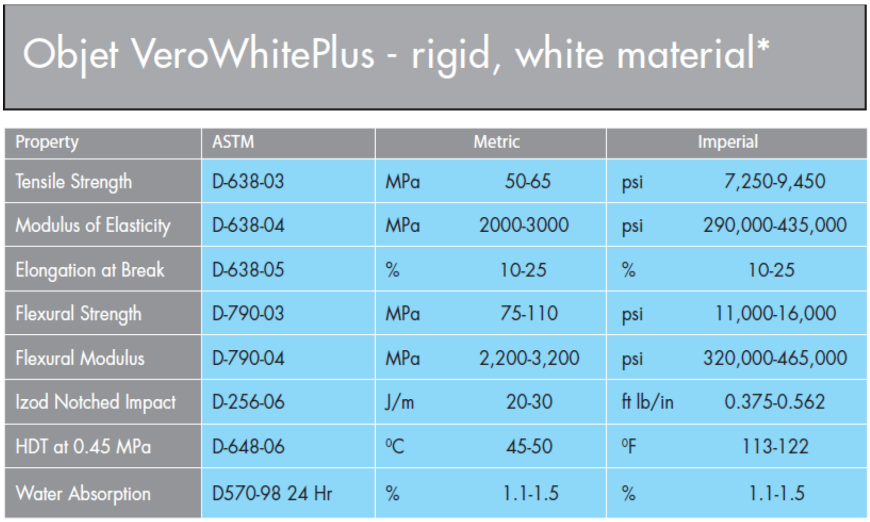

Objet VeroWhitePlus - rigid, white material*

Property	ASTM	Metric		Imperial	
Tensile Strength	D-638-03	MPa	50-65	psi	7,250-9,450
Modulus of Elasticity	D-638-04	MPa	2000-3000	psi	290,000-435,000
Elongation at Break	D-638-05	%	10-25	%	10-25
Flexural Strength	D-790-03	MPa	75-110	psi	11,000-16,000
Flexural Modulus	D-790-04	MPa	2,200-3,200	psi	320,000-465,000
Izod Notched Impact	D-256-06	J/m	20-30	ft lb/in	0.375-0.562
HDT at 0.45 MPa	D-648-06	°C	45-50	°F	113-122
Water Absorption	D570-98 24 Hr	%	1.1-1.5	%	1.1-1.5

Figure 84.VeroWhitePlus material sheet from Stratasys

Appendix D: ***DM 8510, DM 8520 and DM 8530 material sheet and measurement of shape recovery of single material specimens***

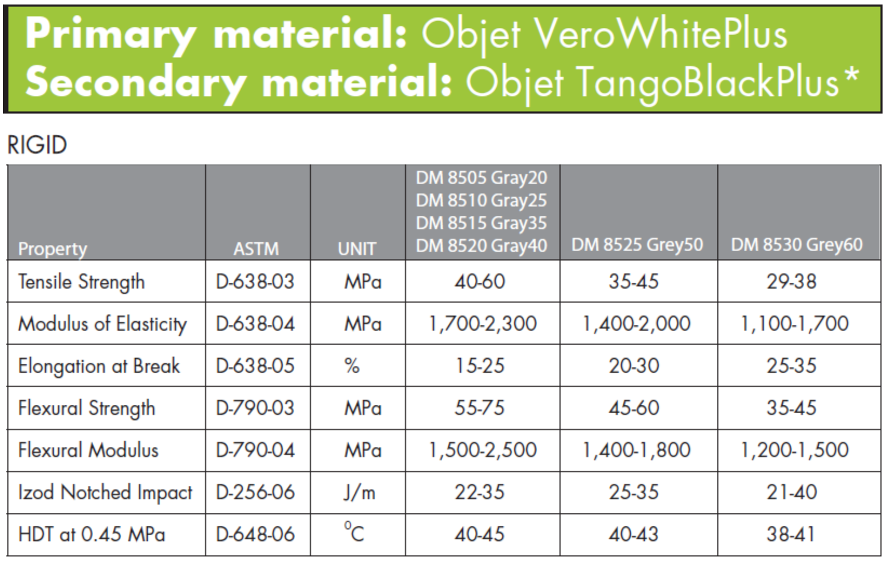

Primary material: Objet VeroWhitePlus
Secondary material: Objet TangoBlackPlus*

RIGID

Property	ASTM	UNIT	DM 8505 Gray20 DM 8510 Gray25 DM 8515 Gray35 DM 8520 Gray40	DM 8525 Grey50	DM 8530 Grey60
Tensile Strength	D-638-03	MPa	40-60	35-45	29-38
Modulus of Elasticity	D-638-04	MPa	1,700-2,300	1,400-2,000	1,100-1,700
Elongation at Break	D-638-05	%	15-25	20-30	25-35
Flexural Strength	D-790-03	MPa	55-75	45-60	35-45
Flexural Modulus	D-790-04	MPa	1,500-2,500	1,400-1,800	1,200-1,500
Izod Notched Impact	D-256-06	J/m	22-35	25-35	21-40
HDT at 0.45 MPa	D-648-06	°C	40-45	40-43	38-41

Figure 85.DM 8510, DM 8520 and DM 8530 material sheet from Stratasys

Measurement of shape recovery of single material specimens (raw data).

Table 15. VeroWhitePlus

Sample No	After Tension (mm)	Percent Elongation (%)	After Recovery (mm)	Percent Recovery (%)
1	28.06	10.7777	25.98	97.4339
2	28.00	10.5409	26.09	96.9996
3	28.12	11.0146	26.10	96.9601
4	28.25	11.5278	26.04	97.1970
5	28.20	11.3304	26.03	97.2365
Average	28.13	11.0383	26.05	97.1654

Table 16. DM 8510

Sample No	After Tension (mm)	Percent Elongation (%)	After Recovery (mm)	Percent Recovery (%)
1	28.10	10.9356	25.75	98.3419
2	28.22	11.4094	25.82	98.0655
3	28.40	12.1200	25.83	98.0261
4	28.46	12.3569	25.83	98.0261
5	28.09	10.8962	25.80	98.1445
Average	28.25	11.5436	25.81	98.1208

Table 17. DM 8520

Sample No	After Tension (mm)	Percent Elongation (%)	After Recovery (mm)	Percent Recovery (%)
1	28.36	11.9621	25.70	98.5393
2	28.29	11.6857	25.72	98.4603
3	28.20	11.3304	25.73	98.4208
4	28.15	11.1330	25.72	98.4603
5	28.35	11.9226	25.73	98.4208
Average	28.27	11.6068	25.72	98.4603

Table 18. DM 8530

Sample No	After Tension (mm)	Percent Elongation (%)	After Recovery (mm)	Percent Recovery (%)
1	28.10	10.9356	25.34	99.9605
2	28.57	12.7912	25.43	99.6052
3	28.16	11.1725	25.48	99.4078
4	28.38	12.0411	25.50	99.3289
5	28.36	11.9621	25.50	99.3289
Average	28.31	11.7805	25.45	99.5263